Improvement of Computational Efficiency for Time-dependent Transport Calculations using Method of Characteristics

Kosuke Tsujita

Department of Applied Energy
Graduate School of Engineering, Nagoya University
2023

This page is intentionally left blank.

Abstract

Efficient numerical methods are developed to improve the computational efficiency of time-dependent transport calculations using the method of characteristics (MOC), which is one of the most challenging topics in reactor analyses due to their enormous computational costs.

To improve the computational efficiency of the time-dependent MOC calculations and to enlarge their applicability to wider applications, *e.g.*, design calculations or real-time applications, the following two approaches are investigated in the present study.

The first one is the improvement of the numerical algorithm for time-dependent MOC calculations using the multigrid amplitude function (MAF) method and the linear source approximation to reduce the temporal and spatial discretization error so that coarser time steps and spatial mesh structures can be used while keeping the accuracy. The accuracy and computational time of the proposed numerical scheme are evaluated through the calculation of the TWIGL and the C5G7-TD 2D benchmark problems, and 6.2 times faster computation than the conventional methods is achieved.

The second one is the construction of the reduced order model (ROM) that reproduces the neutron balance in the time-dependent MOC calculation aiming to use in real-time applications. In the present ROM, the flux distributions and the net neutron currents between the adjacent unstructured mesh regions are taken from the MOC solution. Then, the coefficient matrices for the MOC-equivalent diffusion equation are reconstructed from them. The proper orthogonal decomposition (POD) is applied for the MOC-equivalent diffusion equation to reduce the degree of freedom (DOF) using the orthogonal bases obtained by the singular value decomposition (SVD) for the sampled MOC solution. The accuracy and computation time of the present ROM are verified in the C5G7-TD 2D benchmark problem, and approximately 5000–6000 times faster computation is achieved for the kinetic calculation using ROM.

Throughout the present study, efficient numerical methods that can resolve the primary issues with the computation time of time-dependent MOC calculations are established. These achievements provide a breakthrough in the applications of MOC to safety analyses or real-time applications.

Table of Contents

List of Tables

List of Figures

List of Symbols

(symbols)

$\vec{\Omega}$: Unit vector in the direction of flying neutron
$\vec{r}$: Position
E : Energy
θ : Polar angle
v : velocity
χ : Fission spectrum
ψ : Angular flux
Q : Neutron source
J : Neutron current
k_{eff} : Multiplication factor
β : Delayed neutron fraction
$\mathbf{U}$: Left singular vectors
CP : Core power
s : Coordinate along the flight path
t : Time
φ : Azimuthal angle
Σ : Macroscopic cross section
D : Diffusion coefficient
ϕ : Scalar flux
C : Precursor density
S : (External) neutron source
λ : Decay constant
$\mathbf{S}$: Singular values
$\mathbf{V}$: Right singular vectors

(subscripts/superscripts)

g : Energy group
m : Neutron flight direction
i : Segment
p : Prompt neutron
FOM : Full order model
j : Precursor family
k : Sequential number of path line
r : Flux region
d : Delayed neutron
ROM : Reduced order model

This page is intentionally left blank.

1. Introduction

1.1. Nuclear safety and energy plan

While nuclear power had been employed as a base load power for over 50 years in Japan, the Fukushima Dai-ichi nuclear accident raised large issues regarding nuclear safety. The National Diet of Japan Fukushima Nuclear Accident Independent Investigation Commission (NAIIC) pointed out the overconfidence in nuclear safety by the relevant parties, the lack of countermeasures against severe accidents, and the issue of the mindset that supported the negligence behind the disaster, which is called as “safety myth” [1]. Even 10 years after the disaster, the issues have remained to recover the people’s confidence and to truly achieve nuclear safety. However, stable energy supply and carbon neutrality are also problems since Japan depends on thermal power for 90% of the primary energy supply after the Fukushima Daiichi accident and imports most of the fossil fuels for it [2]. Thus, a well-balanced energy supply employing a variety of energy resources is desirable for a sustainable society. Considering the above situations, in Japan’s basic energy plan, the nuclear power plants that receive approval under the new safety standards established by Nuclear Regulatory Association (NRA) are planned to restart [2]. However, if the power companies focus on only meeting the standard of the regulation, they will be trapped by another safety myth. The Working Group on Voluntary Nuclear Safety Improvement established by the Ministry of Economy, Trade and Industry (METI) is concerned about it and recommends continuous efforts that increase safety voluntarily by the relevant parties [3]. In the field of reactor analysis, investigations also have been promoted to improve the accuracy and reliability of simulations in normal operation, transient, and accident conditions. In the next section, the overview of the reactor analysis is described.

1.2. Overview of reactor analysis

The behavior of the neutron in a reactor core is described by the Boltzmann neutron transport equation as shown in Equation (1.1), and the characteristics of the reactor core are also evaluated from them.

$$\frac{1}{v(\vec{r},E)}\frac{\partial\psi(\vec{r},\vec{\Omega},E,t)}{\partial t} = -\vec{\Omega}\cdot\nabla\psi(\vec{r},\vec{\Omega},E,t) - \Sigma_t(\vec{r},E,t)\psi\left(\vec{r},\vec{\Omega},E,t\right) + Q\left(\vec{r},\vec{\Omega},E,t\right), \quad (1.1)$$

where each symbol is defined in the list of symbols of this dissertation. In reactor analysis, various numerical methods and approximations have been developed to solve the Boltzmann neutron transport equation accurately within reasonable computational resources because of the complexity of the calculation geometry and energy dependence of the cross sections, *e.g.*, Figures 1.1 and 1.2 show the calculation geometry in typical pressurized water reactor (PWR) and the energy dependence of the U-235 total cross section [4].

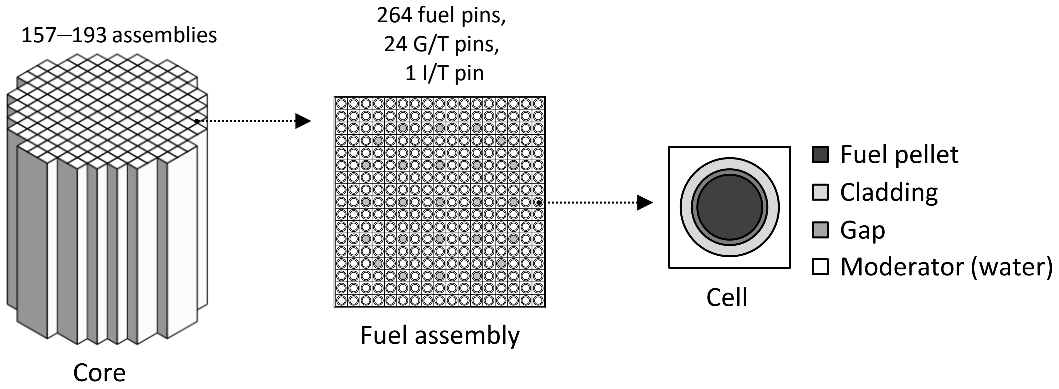

Figure 1.1 Typical PWR geometry

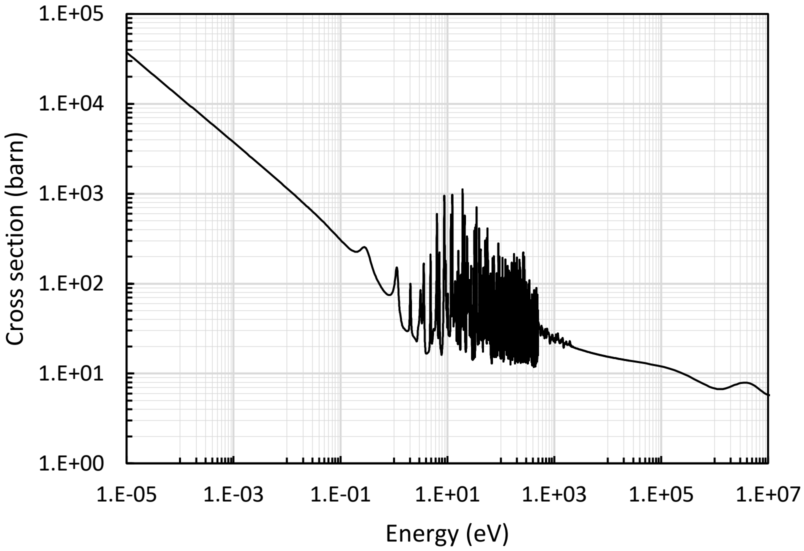

Figure 1.2 Energy dependence of U-235 total cross section

The most principal approximation to numerically treat the Boltzman equation is the discretization of energy as:

$$\frac{1}{v_g(\vec{r})}\frac{\partial\psi_g(\vec{r},\vec{\Omega},t)}{\partial t} = -\vec{\Omega}\cdot\nabla\psi_g(\vec{r},\vec{\Omega},t) - \Sigma_{t,g}(\vec{r},t)\psi_g(\vec{r},\vec{\Omega},t) + Q_g(\vec{r},t)\,, \tag{1.2}$$

where g is the subscript for the energy group. The energy dependence of the microscopic cross sections for each nuclide is discretized into approximately tens of thousands of energy groups. However, since it is still difficult to numerically treat such a large number of energy groups and continuous variables for position ($\vec{r}$) and neutron flight direction ($\vec{\Omega}$) in the core geometry, 2-step calculations, *i.e.*, assembly calculation and core calculation, are employed to treat them at a reasonable computational cost.

In the assembly calculation, detailed flux distribution inside every single assembly is calculated considering the heterogeneity and detailed energy dependence of the cross sections. Then, the assembly-homogenized cross sections used in the core calculation are calculated. Figure 1.3 shows the overview of the assembly calculation.

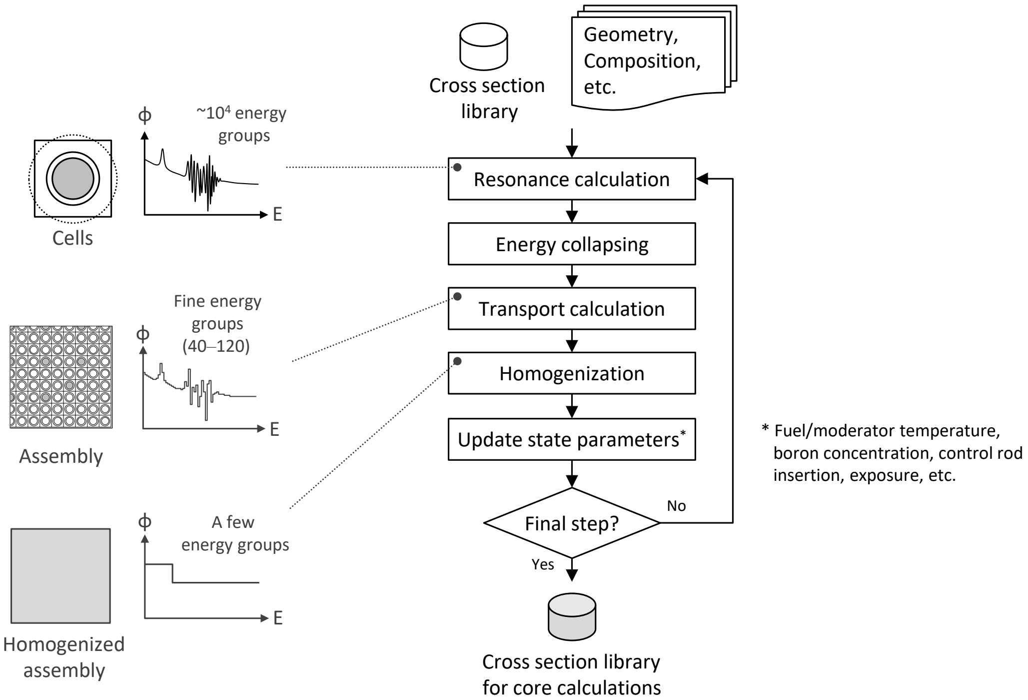

Figure 1.3 Overview of assembly calculation

In the assembly calculation, resonance calculation in pin-cell geometry is carried out considering tens of thousands of energy groups to accurately treat the complicated resonance structure and to obtain the detailed energy spectrum of the neutron flux. Once a detailed energy spectrum of the neutron flux is obtained, energy collapsing is carried out so that the reaction rate is reproduced as:

$$\bar{\Sigma}_G = \sum_{g\in G} \Sigma_g \phi_g \Big/ \sum_{g\in G} \phi_g \,, \tag{1.3}$$

where G is the subscript for the energy group after the energy collapsing, and the energy group structure is collapsed into about 40–120 groups. Then, using the collapsed cross sections, neutron transport calculation is carried out in the heterogeneous lattice geometry. The method of characteristics (MOC) [5] is widely used in transport calculation from the viewpoint of flexibility for heterogeneous geometries and accuracy. In the MOC calculation, neutron flight directions are discretized and a large number of neutron flight paths are considered as shown in Figure 1.4.

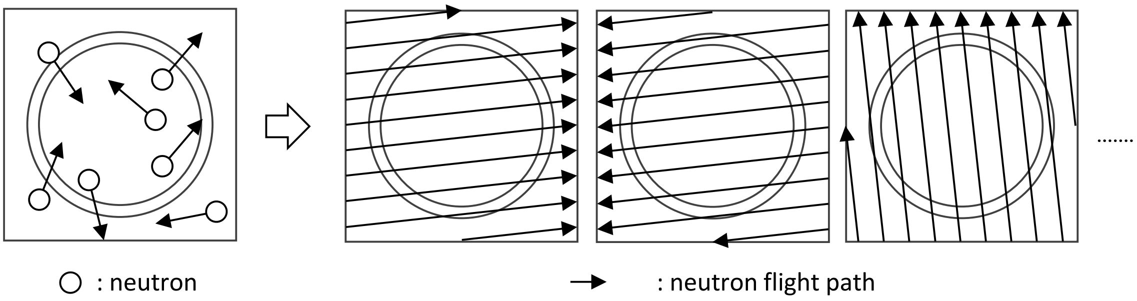

Figure 1.4 Overview of MOC calculations

In typical calculation conditions, about 48–128 directions for azimuthal angle, 3 directions for polar angle, and the flight paths with 0.01–0.1 cm intervals are considered. Then, by solving the Boltzmann equation along each flight path line, spatially averaging them, and integrating the angular fluxes for the total solid angle, scalar flux is obtained as shown in Figure 1.5.

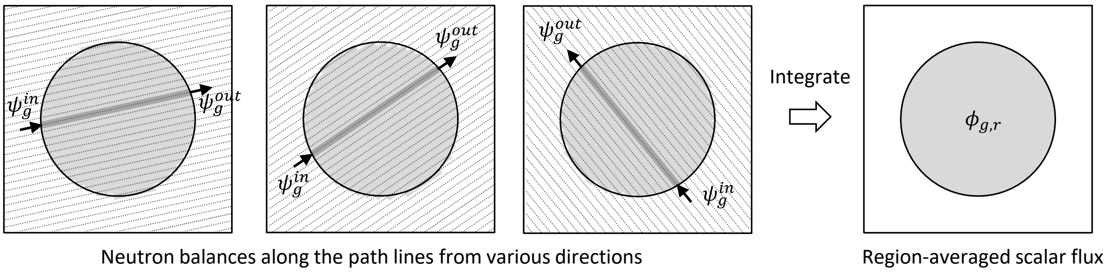

Figure 1.5 Neutron balance along flight paths

Once a flux distribution in the lattice geometry is obtained, the assembly-homogenized cross sections used in the core calculation are also calculated so that the averaged reaction rate in the assembly is reproduced as:

$$\bar{\Sigma}_G = \sum_r \sum_{g \in G} \Sigma_{g,r} \phi_{g,r} V_r \Big/ \sum_r \sum_{g \in G} \phi_{g,r} V_r \,, \tag{1.4}$$

where G denotes the energy group after the homogenization, and the energy group structure is finally collapsed into a few energy groups. These calculations are carried out in various state parameters (*e.g.*, different fuel temperatures, moderator temperatures, boron concentration, exposure, and control rod insertion) so that they encompass the assembly states that appear in the core calculations. Finally, the homogenized cross sections are tabulated as functions of state parameters, and they are summarized as a cross section library for the core calculation.

In the core calculation, using the assembly-homogenized cross section library obtained from the assembly calculation, the diffusion equation derived by expanding the angular dependence of angular flux up to the 1st order of Legendre functions is solved to obtain the flux distribution in the core geometry. The core is divided into larger mesh regions, *e.g.*, approximately 10 cm×10 cm×15cm per mesh in the typical PWR geometry, and the nodal expansion method [6] is widely employed to reduce the spatial discretization error. While each assembly is already homogenized in the core calculation, the pin power distribution is reconstructed using the global flux distribution inside each node and the local (intra-assembly) power distribution obtained in the assembly calculation [7].

As described above, the conventional reactor analysis is carried out gradually reducing the number of variables by the spatial homogenization and energy collapsing via the assembly and core calculations. However, there are several issues with this approach:

- Incoming/outgoing neutrons from/to the adjacent assembly are not taken into account in the assembly calculation. Thus, assembly-homogenized cross sections include the homogenization error due to the difference in the flux distributions between the assembly and core calculations.
- The diffusion calculation includes the approximation error since the angular dependence of angular flux is taken into account only up to the 1st order of Legendre functions.
- Pin power reconstruction includes the approximation error due to the limitation of the modeling.

Especially, the adjacent loading of different types of the fuels such as the mixed oxide (MOX) and UO_2 fuels emphasizes the above modeling error, *e.g.*, approximately 4–5% error for pin power and several hundreds of pcm error for k-effective are observed [8, 9].

To overcome these issues and to improve the accuracy of reactor analysis, direct core calculations without spatial homogenization are investigated. While various numerical approaches are proposed in past studies, *e.g.*, direct core calculation using the Mote-Calro [10–12], the response matrix methods [13, 14], and the MOC [15–21], the MOC is one of the most practical approaches from the viewpoints of computational cost and accuracy for local parameters such as pin power in large heterogeneous geometries because stochastic approaches generally require enormous computation time to achieve enough statistics for local parameters. The most popular approach with the MOC is the following "planer" MOC calculations employed in the DeCART code as follows [15]:

(1) Dividing the axial direction of the core into dozens of planes and the 2D MOC calculations for the radial direction in each plane are employed. This modeling is supported by the high separability of the axial and radial directions in the typical nuclear reactor since the heterogeneity of reactors is generally smaller than that of radial direction.

(2) Using the heterogeneous flux distribution in each 2D plane obtained from the 2D MOC calculations, the homogenized cross sections and the correction terms for neutron current are calculated to reproduce both the neutron current and reaction rate.

(3) Using the homogenized cross sections and correction terms for neutron current, a 3D core calculation is carried out to obtain axial leakage between the planes.

(4) Updating external sources for 2D MOC calculations by the axial leakage in each plane, repeat to (1)–(4) until the convergence criterion.

As another more direct 3D MOC calculation, ASMOC3D [20] and LEAF [21] methods are proposed. In the ASMOC3D and LEAF methods, the neutron flight path is extended as is in the axial direction as shown in Figure 1.6, and the neutron balance along each plane is calculated.

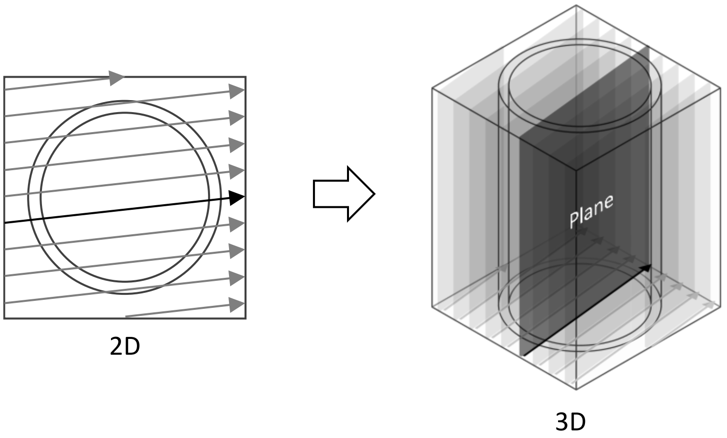

Figure 1.6　3D plane for neutron flight path in ASMOC3D and LEAF methods

Using these high-fidelity core calculations using the MOC, the issues on the conventional 2-step methods can be resolved. Thus, the application of these simulations to best-estimate analyses, uncertainty quantification (UQ), verification and validation (V&V) of the core calculation codes are expected, *e.g.*,

- More accurate and reliable prediction for the multi-physics phenomena inside the reactor during normal operation, transient, and accident conditions.
- Quantification of the error due to numerical modeling, and estimation of the conservatism in fuel design limit for accidents [22].
- An alternative to experiments as a "virtual" nuclear reactor when there are difficulties in the experiment itself, *e.g.*, alternative of the local parameters that can not be measured directly [23].

In the next section, issues with high-fidelity MOC calculations are described.

1.3. Issues with high-fidelity MOC calculations

As described in Section 1.2, high-fidelity MOC calculations are expected to provide accurate simulation results with less approximation. However, they generally require enormous computational costs, *e.g.*, the number of unknowns in the typical MOC calculations is approximately 10^6 times larger than conventional diffusion calculations and the computation time is generally dozens of hours even using parallel calculations. The application of such simulations to time-dependent calculations such as accident analyses requires much longer computation time. Thus, the application of the MOC to industrial use is limited only to assembly calculations, and approximately 10^3–10^4 times or more speed-up would be required to apply it to design calculations, safety analyses, or real-time applications. While several efficient numerical algorithms have been developed for MOC calculations to reduce their high computational cost, such speed-up has not been achieved yet due to an enormous number of degrees of freedom (DOF) in the spatial domain [15, 24–28].

On the other hand, as long as solving the neutron balance along a large number of neutron flight paths in MOC, it is quite difficult to achieve real-time calculations. Thus, as an alternative approach, dimensionality reduction (DR) techniques are expected to provide an equivalent of MOC calculations in specific calculation conditions. In one of the most successful DR techniques, the proper orthogonal decomposition (POD) [29], the flux distributions are expanded with a suitable orthogonal basis for the target problem, and then the DOF is dramatically reduced by converting the neutron balance equation into the equation for expansion coefficients, where the such suitable basis is obtained by the singular value decomposition (SVD) for the flux vectors taken from the full-order model (FOM) solutions. In past studies [30–32], the POD has been successfully applied to neutron diffusion and S_N transport calculations. However, the neutron balance equation must be described in matrix form to apply the POD. An effective way to apply the POD for MOC calculations has not been established because the balance equation in the MOC is not generally described in a matrix form and enormous memory is also required for it.

1.4. Purpose and outline

As described in Section 1.3, the primary issue of high-fidelity MOC calculations is the high computational cost, and efficient numerical methods that enable us to apply the MOC to design calculations or real-time applications have not been established yet in past studies. There are also difficulties in directly constructing a reduced order model (ROM) as an alternative for MOC calculations with the POD. Therefore, the present study aims to improve the efficiency of the time-dependent MOC calculations, which have especially high computational costs and are also important in safety analyses, considering the following two approaches:

(1) Improvement in the computational efficiency of the time-dependent MOC calculation itself using enhanced numerical methods

(2) Development of an effective way to construct a ROM for time-dependent MOC

calculations

The contents of this dissertation are organized into the following 5 chapters:

In Chapter 1, the background and the purpose of the present study are described.

In Chapter 2, the efficiency of time-dependent MOC calculations is improved using the multigrid amplitude function (MAF) method [26, 33] and the linear source approximation [25, 21]. In the previous study [26], the MAF method is successful to improve the computational efficiency of time-dependent transport calculations using MOC. However, a large number of spatial meshes are required in strongly heterogeneous geometry to reduce the spatial discretization error, and it degrades the computational efficiency of the MAF method. In this chapter, using the spatial discretization error reduction technique and the MAF method, a more efficient numerical scheme is developed. The accuracy and computational efficiency of the present scheme are verified in the TWIGL and the C5G7-TD 2D benchmark problems [34, 35]. The present numerical scheme is used as the FOM in Chapter 4 and also contributes to shortening the computation time of the FOM.

In Chapter 3, an efficient way to construct an orthogonal basis employed in time-dependent calculations using the POD is investigated aiming to construct a ROM for time-dependent calculations. Higher-order flux distributions excited in transient must be accurately represented by an orthogonal basis to construct a ROM for time-dependent calculations using the POD. In this chapter, several sets of orthogonal bases, which are constructed using the different types of flux distributions, are tested to find a suitable dataset for the construction of the orthogonal basis that represents the higher-order flux distributions accurately and efficiently.

In Chapter 4, an efficient ROM using the POD for the time-dependent MOC calculations is developed. As discussed in Section 1.3, an effective way to apply the POD for MOC calculations has not been established because the balance equation in the MOC is not generally described in a matrix form. In this chapter, coefficient matrices that reproduce a MOC solution are reconstructed using diffusion calculation with a correction term for neutron current, and then the POD is applied to it. The accuracy and computational efficiency of the present ROM with respect to the FOM are verified in the C5G7-TD 2D benchmark problem.

Finally, the concluding remarks of this dissertation are summarized in Chapter 5.

1.5. Reference

[1] NAIIC, The official report of the Fukushima Nuclear Accident Independent Investigation Commission. 2022. (https://reliefweb.int/report/japan/official-report-fukushima-nuclear-accident-independent-investigation-commission)

[2] Ministry of Economy, Trade and Industry, Strategic Energy Plan. 2022. (https://www.enecho.meti.go.jp/about/whitepaper/2022/pdf/)

[3] Working Group on Voluntary Efforts and Continuous Improvement of Nuclear Safety. 2013. (https://www.meti.go.jp/english/policy/energy_environment/nuclear_energy_subcommittee/index.html)

[4] Homepage for Nuclear data center in Japanese Atomic Energy Agency. (http://wwwndc.jaea.go.jp/index.html)

[5] Halsall MJ. CACTUS, A characteristics solution to the neutron transport equation in complicated geometries, Winfrith (United Kingdom): UKAEA; 1980, (AEEW-R 1291).

[6] Downar T, Xu Y, Seker V. PARCS v3.0 U.S. NRC neutronics simulator theory manual. Ann Arbor: Department of Nuclear Engineering and Radiological Sciences, University of Michigan; 2009.

[7] Bahadir T, Lindahl S. Studsvik's Next generation nodal code SIMULATE-5. Proc ANFM 2009; 2009 Apr 12–15; Hilton Head Island, South Carolina.

[8] Mori M, Kawamura M, Yamate K. CASMO-4/SIMULATE-3 benchmarking against high Plutonium content pressurized water reactor mixed-oxide fuel critical experiment. Nucl Sci Eng. 1995; 121(1): 41–51.

[9] Cho HH, Kang J, Yoon JI, Joo HG, Analysis of C5G7-TD benchmark with a multi-group pin homogenized SP3 code SPHINCS. Nucl Eng Technol. 2021; 53(5):1403–1415.

[10] Shaukat N, Ryu M, Shim HJ. Dynamic Monte Carlo transient analysis for the Organization for Economic Co-operation and Development Nuclear Energy Agency (OECD/NEA) C5G7-TD benchmark. Nucl Eng Technol. 2017; 49(5):920–927.

[11] Mausolff Z, DeHart M, Goluoglu S. Enhanced geometric capabilities for the transient analysis code T-ReX and its application to simulating TREAT experiments. Prog Nucl Energy. 2018; 105:236–246.

[12] Kreher MA, Smith K, Forget B, Frequency transform method for transient analysis of nuclear reactors in Monte Carlo. Nucl Sci Eng. 2022.
DOI: https://doi.org/10.1080/00295639.2022.2067739

[13] Mitsuyasu T. Development of BWR core analysis method by direct response matrix method. Nagoya University; 2020. (in Japanese)

[14] Mickus I, Roverts JA, Dufek J, Stochastic-deterministic response matrix method for reactor transients. Ann Nucl Energy. 2020;40:107103.

[15] Hursin M, Downar TJ, Kochunas B. Analysis of the core power response during a PWR rod ejection transient using the PARCS nodal code and the DeCART MOC code. Nucl Sci Eng. 2012; 170(2):151–167.

[16] Kosaka S, Takeda T, Verification of 3D heterogeneous core transport calculation utilizing non-linear Iteration technique, J Nucl Sci Technol. 2003; 41:645–654.

[17] Ryu M, Joo HG. nTRACER whole core transport solutions to C5G7 TD benchmark. Proc M&C 2017; 2017 Apr 16 20; Jeju, Korea.

[18] Shen Q, Wang Y, Jabaay D, Kochunas B, Downar TJ. Transient analysis of C5G7-TD benchmark with MPACT. Ann Nucl Energy. 2019;125:107–120.

[19] Nguyen TN, Jung YS, Downar TJ, Lee C. Implementation of the transient fixed source problem in the neutron transport code PROTEUS MOC. Ann Nucl Energy. 2019; 129:199–206.

[20] Giho A, Sakai K, Imamura Y, Sakuragi H, Miyawaki K. Development of axially simplified method of characteristics in three-dimensional geometry. 2008;45(10):985–996.

[21] Yamamoto A, Giho A, Kato Y, Endo T. GENESIS – a three-dimensional heterogeneous transport solver based on the Legendre polynomial expansion of angular flux method. Nucl Sci Eng. 2017;186(1):1–22.

[22] Hursin M, Downar T. PWR control rod ejection analysis with the MOC code DeCART. Joint International Workshop: Nuclear Technology and Society-Needs for Next Generation; 2008 Jan. 6–8; Berkeley, California.

[23] US Department of Energy, VERA : The virtual environment for reactor applications.
(https://vera.ornl.gov/)

[24] Tabuchi M, Yamamoto A, Endo T, Sugimura N, Preservation of transmission probabilities in the method of characteristics. J Nucl Sci Technol. 2013;50[8];837–843.

[25] Ferrer R, Rhodes J. Linear source approximation in CASMO5. Proc PHYSOR 2012; 2012 Apr 15–20; Knoxville, Tennessee.

[26] Tsujita K, Endo T, Yamamoto A. Application of the multigrid amplitude function method for time-dependent transport equation using MOC. Proc M&C 2013; 2013 May 5–9; Sun Valley, Idaho.

[27] Shaner SC. Transient method of characteristics via the adiabatic, theta and multigrid amplitude function methods. Cambridge (Massachusetts): Massachusetts Institute of Technology; 2014.

[28] Shen Q, Kochunas B, Xu Y, Downar TJ. Transient multilevel scheme with one group CMFD acceleration. Proc PHYSOR 2018; 2018 Apr 22–26; Cancun, Mexico.

[29] Anttonen JSR, King PI, BERAN PS. POD-Based reduced-order models with deforming grids. Math. Comput. Modell. 2003; 38:41–62.

[30] Behne PA, Ragusa JC, Morel JE. Model order reduction for S_N radiation transport. Proc M&C 2019; 2019 Aug. 25–29; Oregon, Portland.

[31] Elzohery R, Roberts J, Exploring transient, neutronic, reduced-order models using DMD/POD-Galerkin and data-driven DMD, Proc PHYSOR 2020; 2020 Mar 29–Apr 2; Cambridge, United Kingdom.

[32] Elzohery R, Roberts J. Modeling neutronic transients with Galerkin projection onto a greedy-sampled, POD subspace. Ann Nucl Energy. 2021;162.

[33] Ban Y, Endo T, Yamamoto A. A unified approach for numerical calculation of space-dependent kinetic equation. J Nucl Sci Technol. 2012;49:496–515.

[34] Taylor JB. The development of a three-dimensional nuclear reactor kinetics methodology based on the method of characteristics. University Park (Pennsylvania): Pennsylvania State University; 2007.

[35] Boyarinov VF, Fomichenko PA, Hou JJ, Ivanov KN, Aures A, Zwermann W, Velkov K. Deterministic time-dependent neutron transport benchmark without spatial homogenization (C5G7-TD). OECD Nuclear Energy Agency; 2017.

2. Application of the MAF method for time-dependent MOC based on the linear source approximation

2.1. Introduction

As discussed in Chapter 1, neutron transport calculations for large heterogeneous geometries have become easier and the MOC [1] is being widely used for reactor analysis. In the field of reactor kinetics, time-dependent transport calculations without spatial homogenization are one of the most challenging topics [2–6] since the computational cost of MOC in large heterogeneous geometry is still expensive. Thus, various numerical methods were developed to improve the computational efficiency of time-dependent transport calculations. For example, the predictor-corrector quasi-static (PCQS) method [7], the MAF method [8–10], and the transient multilevel (TML) scheme [11] are successful to achieve faster computation since coarser time steps are available for the MOC calculation by the factorization of the scalar flux into the amplitude and shape functions. Especially, the MAF method was also successful to minimize the degradation of the accuracy by considering the spatial dependence of the amplitude function, and its effectiveness is also confirmed by other researchers [10]. However, since the MAF method was derived based on the flat flux assumption in past studies [9, 10], a large number of flux regions are required in strongly heterogeneous geometry to reduce the spatial discretization error. Although higher-order spatial treatments for MOC are proposed, *e.g.*, the orthogonal function expansion implemented in PROTEUS-MOC [12] or the linear source approximation [13, 14], etc., the linear source approximation for the time-dependent MOC has not been applied yet as far as the author’s knowledge.

Therefore, in this chapter, a calculation scheme of the MAF method based on the linear source approximation is proposed to improve the computational efficiency of the time-dependent MOC calculations. The accuracy of the present scheme is confirmed through two benchmark calculations, *i.e.*, the transport extension of the TWIGL seed blanket problem [15] and the C5G7-TD 2D benchmark problem [16]. In this chapter, the theoretical extension of the MAF method based on the linear source approximation and the calculation results for the benchmark problems are described in Sections 2.2 and 2.3, respectively. Finally, concluding remarks are provided in Section 2.4.

2.2. Methodology

In this section, a calculation scheme of the MAF method based on the linear source approximation is described. The MAF method is one of the factorization methods, which describes the scalar flux as a product of two functions, *i.e.*, the shape and amplitude functions as follows [8, 9]:

$$\phi_g(\vec{r},t) = \varphi_g(\vec{r},t)P_{g,I}(t)\,, \tag{2.1}$$

where

$\phi_{g,r}(\vec{r},t)$	:	scalar flux,
$\varphi_g(\vec{r},t)$	:	shape function,
$P_{g,I}(t)$	:	amplitude function.

g and *I* are the subscripts for the energy group and the coarse mesh, respectively. The shape function represents a weak and strong dependence on time and space, respectively. Contrary, the amplitude function represents strong and weak dependences for time and space, respectively. In the MAF method, the weak spatial dependence of the amplitude function is represented by the coarse-mesh-wise distribution of the integrated neutron density, which is defined as:

$$P_{g,I}(t) \equiv \int_{V_I} \frac{\phi_g(\vec{r},t)}{v_g(\vec{r})}dV\,, \tag{2.2}$$

where V_I denotes the volume of the coarse mesh I. The computational costs of these functions are smaller than that of the scalar flux since the shape and amplitude functions can be calculated by a coarse time step calculation in a fine geometry and a fine time step calculation in coarse geometry, respectively. The basic concept of the MAF method is to obtain spatially and temporally fine results by combining these two calculations with fewer computation resources. In the following subsections, the theoretical basis of each calculation is described based on the linear source approximation, which is not applied in the previous study [9].

2.2.1. Coarse step calculation in fine geometry

In this subsection, the balance equation based on MOC with a coarse time step is derived based on the linear source approximation. The time-dependent transport equations assuming isotropic scattering and source are written as:

$$\frac{1}{v_g(\vec{r})}\frac{\partial\psi_g(\vec{r},\vec{\Omega},t)}{\partial t} = -\vec{\Omega}\cdot\nabla\psi_g\big(\vec{r},\vec{\Omega},t\big) - \Sigma_{t,g}(\vec{r},t)\psi_g\big(\vec{r},\vec{\Omega},t\big) + Q_g(\vec{r},t)\,, \tag{2.3}$$

$$Q_g(\vec{r},t) = \frac{1}{4\pi}\left\{ \begin{array}{c} \chi_g^p(\vec{r})\big(1-\beta(\vec{r})\big)\sum_{g'} \nu\Sigma_{f,g'}(\vec{r},t)\phi_{g'}(\vec{r},t) \\ +\sum_{g'} \Sigma_{s,g'\to g}(\vec{r},t)\phi_{g'}(\vec{r},t) + \sum_{j} \chi_{j,g}^d(\vec{r})\lambda_j C_j(\vec{r},t) \end{array} \right\}, \tag{2.4}$$

$$\frac{\partial C_j(\vec{r},t)}{\partial t} = \beta_j(\vec{r})\sum_{g'} \nu\Sigma_{f,g'}(\vec{r},t)\phi_{g'}(\vec{r},t) - \lambda_j C_j(\vec{r},t)\,, \tag{2.5}$$

where each symbol and subscript are defined in the list of symbols of this dissertation. Generally speaking, an approximation for the temporal derivative of the angular flux is necessary to perform the kinetic calculation using MOC within practical memory requirements. In the present study, the isotropic approximation for the temporal derivative of the angular flux is employed as well as DeCART code, *i.e.*, Equation (2.3) is approximated as [3]:

$$\frac{1}{4\pi}\frac{1}{v_g(\vec{r})}\frac{\partial \phi_g(\vec{r},t)}{\partial t} = -\vec{\Omega}\cdot\nabla\psi_g\big(\vec{r},\vec{\Omega},t\big) - \Sigma_{t,g}(\vec{r},t)\psi_g\big(\vec{r},\vec{\Omega},t\big) + Q_g(\vec{r},t)\,, \tag{2.6}$$

The validity of this approximation is confirmed in the previous study [17]. Discretizing the neutron flight direction and space for Equation (2.6), the balance equation along a neutron path line is described as

$$\frac{1}{4\pi}\frac{1}{v_{g,r}}\frac{\partial \phi_{g,m,k,i}(s,t)}{\partial t} = -\frac{\partial \psi_{g,m,k,i}(s,t)}{\partial s} - \Sigma_{t,g,r}(t)\psi_{g,m,k,i}(s,t) + Q_{g,m,k,i}(s,t)\,, \tag{2.7}$$

where

m : neutron flight direction,
k : sequential number of the path line,
i : segment,
r : flux region,
s : coordinate along the neutron flight direction,

and Figure 2.1 shows their definitions.

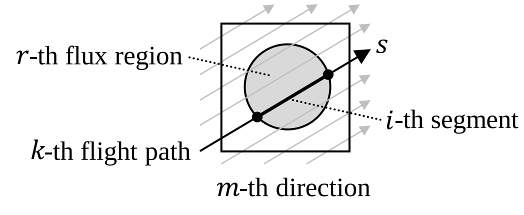

Figure 2.1 Neutron flight direction, flight path, segment, and flux region

In the present study, the linear source approximation is employed, *i.e.*, the scalar flux, the neutron source, and the precursor density are described as follows [13, 14]:

$$\phi_{g,m,k,i}(s,t) = \phi_{g,r}(t) + x_{m,k,i}(s)\phi_{g,r}^{x}(t) + y_{m,k,i}(s)\phi_{g,r}^{y}(t)\,, \tag{2.8}$$

$$Q_{g,m,k,i}(s,t) = \frac{1}{4\pi}\left\{\begin{matrix} \chi_{g,r}^{p}(1-\beta_r)\sum_{g'}\nu\Sigma_{f,g',r}(t)\phi_{g',m,k,i}(s,t) \\ +\sum_{g'}\Sigma_{s,g'\to g,r}(t)\phi_{g',m,k,i}(s,t) + \sum_{j}\chi_{j,g,r}^{d}\lambda_j C_{j,m,k,i}(s,t) \end{matrix}\right\}, \tag{2.9}$$

$$C_{j,m,k,i}(s,t) = C_{j,r}(t) + x_{m,k,i}(s)C_{j,r}^{x}(t) + y_{m,k,i}(s)C_{j,r}^{y}(t)\,, \tag{2.10}$$

where, $x_{m,k,i}(s)$ and $y_{m,k,i}(s)$ are the local coordinates whose origins are the geometrical centroid of the flux region, which are described as [13]:

$$\int_{V_r} x_{m,k,i}(s)dV = \sum_{m}\omega_m\sum_{k}\Delta A_{m,k}\int_{s_{m,k,i}} x_{m,k,i}(s)ds = 0\,, \tag{2.11}$$

$$\int_{V_r} y_{m,k,i}(s)dV = \sum_{m}\omega_m\sum_{k}\Delta A_{m,k}\int_{s_{m,k,i}} y_{m,k,i}(s)ds = 0\,, \tag{2.12}$$

where $\Delta A_{m,k}$ denotes the width of the path line. Noting the definition of the amplitude function, Equation (2.2) is described as

$$\begin{aligned} P_{g,I}(t) &\equiv \int_{V_I}\frac{\phi_g(\vec{r},t)}{v_g(\vec{r})}dV = \sum_{r\in I}\frac{\int_{V_r}\phi_g(\vec{r},t)dV}{v_{g,r}} \\ &= \sum_{r\in I}\frac{\int_{V_r}\left(\phi_{g,r}(t) + x_{m,k,i}(s)\phi_{g,r}^{x}(t) + y_{m,k,i}(s)\phi_{g,r}^{y}(t)\right)dV}{v_{g,r}} \\ &= \sum_{r\in I}\frac{\phi_{g,r}(t)V_r}{v_{g,r}}\,, \end{aligned} \tag{2.13}$$

where V_r denotes the volume of the flux region r. Equation (2.13) indicates the global shape of the 0th-order flux coefficient distribution can be captured by the amplitude function. Thus, the 0th-order coefficient of the scalar flux is factorized as a product of the shape and amplitude functions,

$$\phi_{g,r}(t) = \varphi_{g,r}(t)P_{g,I}(t)\,, \tag{2.14}$$

$$\begin{aligned}\frac{d\phi_{g,r}(t)}{dt} &= \varphi_{g,r}(t)\frac{dP_{g,I}(t)}{dt} + \frac{d\varphi_{g,r}(t)}{dt}P_{g,I}(t) \\ &= \varphi_{g,r}(t)P_{g,I}(t)\frac{1}{P_{g,I}(t)}\frac{dP_{g,I}(t)}{dt} + \frac{d\varphi_{g,r}(t)}{dt}P_{g,I}(t) \\ &= \omega_{g,I}(t)\phi_{g,r}(t) + \frac{d\varphi_{g,r}(t)}{dt}P_{g,I}(t)\ ,\end{aligned} \tag{2.15}$$

where $\omega_{g,I}(t)$ is space- and energy-dependent dynamic frequency defined as

$$\omega_{g,I}(t) \equiv \frac{1}{P_{g,I}(t)}\frac{dP_{g,I}(t)}{dt}\ , \tag{2.16}$$

Assuming the temporal derivative of the 1st order coefficients of the scalar flux as zero because it is considered to be small, Equation (2.7) s approximated as:

$$\begin{aligned}\frac{1}{4\pi}\frac{1}{v_{g,r}}\frac{\partial\phi_{g,m,k,i}(s,t)}{\partial t} &\approx \frac{1}{4\pi}\frac{1}{v_{g,r}}\frac{d\phi_{g,r}(t)}{dt} \\ &= \frac{1}{4\pi}\frac{1}{v_{g,r}}\left(\omega_{g,I}(t)\phi_{g,r}(t) + \frac{d\varphi_{g,r}(t)}{dt}P_{g,I}(t)\right) \\ &= -\frac{\partial\psi_{g,m,k,i}(s,t)}{\partial s} - \Sigma_{t,g,r}(t)\psi_{g,m,k,i}(s,t) + Q_{g,m,k,i}(s,t)\ ,\end{aligned} \tag{2.17}$$

where the validity of this approximation is confirmed in Section 2.3. Solving Equation (2.17) for the temporal derivative of the shape function,

$$\frac{1}{4\pi v_{g,r}}\frac{d\varphi_{g,r}(t)}{dt} = \frac{1}{P_{g,I}(t)}\begin{pmatrix} -\dfrac{\partial\psi_{g,m,k,i}(s,t)}{\partial s} - \Sigma_{t,g,r}(t)\psi_{g,m,k,i}(s,t) \\ +Q_{g,m,k,i}(s,t) - \dfrac{\omega_{g,I}(t)}{4\pi v_{g,r}}\phi_{g,r}(t)\end{pmatrix}. \tag{2.18}$$

To numerically solve Equation (2.18), the fully implicit method is employed in the present study for the temporal derivative of the shape function as:

$$\frac{\varphi_{g,r}(t_{n+1}) - \varphi_{g,r}(t_n)}{4\pi v_{g,r}\Delta t_{shape}} = \frac{\begin{pmatrix} -\dfrac{\partial\psi_{g,m,k,i}(s,t_{n+1})}{\partial s} - \Sigma_{t,g,r}(t_{n+1})\psi_{g,m,k,i}(s,t_{n+1}) \\ +Q_{g,m,k,i}(s,t_{n+1}) - \dfrac{\omega_{g,I}(t_{n+1})}{4\pi v_{g,r}}\phi_{g,r}(t_{n+1})\end{pmatrix}}{P_{g,I}(t_{n+1})}\ . \tag{2.19}$$

where n and Δt_{shape} denote time step and time step size for the shape function, respectively. Note that coarse time step size is available for the temporal discretization because the shape function represents weak dependence on time. Multiplying the amplitude function at $t = t_{n+1}$ for both sides, Equation (2.19) is described as

$$\frac{\partial \psi_{g,m,k,i}(s,t_{n+1})}{\partial s} + \Sigma_{t,g,r}(t_{n+1})\psi_{g,m,k,i}(s,t_{n+1}) =$$
$$Q_{g,m,k,i}(s,t_{n+1}) - \frac{\phi_{g,r}(t_{n+1})}{4\pi v_{g,r}}\left(\frac{1}{\Delta t_{shape}} + \omega_{g,I}(t_{n+1})\right) + \frac{\phi_{g,r}(t_n)}{4\pi v_{g,r}\Delta t_{shape}}\frac{P_{g,I}(t_{n+1})}{P_{g,I}(t_n)}. \tag{2.20}$$

As for the precursor density, the factorization method was also proposed in a past study [8]. In this study, it is employed for the 0th-order coefficient of the precursor density, *i.e.*,

$$C_{j,r} = \tilde{P}_{j,I}(t)\tilde{\varphi}_{j,r}(t), \tag{2.21}$$

$$\tilde{\omega}_{j,I}(t) \equiv \frac{1}{\tilde{P}_{j,I}(t)}\frac{d\tilde{P}_{j,I}(t)}{dt}. \tag{2.22}$$

Using Equations (2.21), (2.22), and the theta method, the numerical solution of Equation (2.5) is described as follows [8]:

$$C_{j,r}(t_{n+1}) = \mu_j C_{j,r}(t_n) + \eta_j \sum_{g'} \nu\Sigma_{f,g',r}(t_n)\phi_{g',r}(t_n)$$
$$+\xi_j \sum_{g'} \nu\Sigma_{f,g',r}(t_{n+1})\phi_{g',r}(t_{n+1}), \tag{2.23}$$

$$\mu_j = \frac{1-(1-\theta)\lambda_j\Delta t_{shape} - (1-\theta)\tilde{\omega}_{j,I}(t_n)\Delta t_{shape}}{1+\theta\lambda_j\Delta t_{shape} + \theta\Delta t_{shape}\tilde{\omega}_{j,I}(t_{n+1})}\frac{\tilde{P}_{j,I}(t_{n+1})}{\tilde{P}_{j,I}(t_n)}, \tag{2.24}$$

$$\eta_j = \frac{(1-\theta)\beta_{j,r}\Delta t_{shape}}{1+\theta\lambda_j\Delta t_{shape} + \theta\Delta t_{shape}\tilde{\omega}_{j,I}(t_{n+1})}\frac{\tilde{P}_{j,I}(t_{n+1})}{\tilde{P}_{j,I}(t_n)}, \tag{2.25}$$

$$\xi_j = \frac{\theta\beta_{j,r}\Delta t_{shape}}{1+\theta\lambda_j\Delta t_{shape} + \theta\Delta t_{shape}\tilde{\omega}_{j,I}(t_{n+1})}. \tag{2.26}$$

where θ is the weighting parameter in the theta method. In the present study, $\theta = 1$ is assumed as well as the temporal derivative of the shape function for the scalar flux. The 1st-order spatial coefficients of the precursor density are calculated without factorization in the present study. Thus, the formulation of the numerical solution is the same as Equations (2.23)–(2.26) but $\tilde{P}_{j,I}(t_{n+1})/\tilde{P}_{j,I}(t_n) = 1$ and $\tilde{\omega}_{j,I}(t) = 0$ are used for them. Substituting Equation (2.23) into Equation (2.20), the balance equation in the fine geometry is described as

$$\begin{aligned}\frac{\partial \psi_{g,m,k,i}(s,t_{n+1})}{\partial s} &+ \Sigma_{t,g,r}(t_{n+1})\psi_{g,m,k,i}(s,t_{n+1}) \\ &= \hat{Q}_{g,m,k,i}(s,t_{n+1}) + \hat{S}_{g,m,k,i}(s,t_n)\,,\end{aligned} \tag{2.27}$$

where

$$\hat{Q}_{g,m,k,i}(s,t_{n+1}) = \frac{1}{4\pi}\left\{\begin{aligned} &\gamma_{g,r}\sum_{g'}\nu\Sigma_{f,g',r}(t_{n+1})\phi_{g',m,k,i}(s,t_{n+1}) \\ &+\sum_{g'}\Sigma_{s,g'\to g,r}(t_{n+1})\phi_{g',m,k,i}(s,t_{n+1}) \\ &-\frac{\phi_{g,r}(t_{n+1})}{v_{g,r}}\left(\frac{1}{\Delta t_{shape}} + \omega_{g,I}(t_{n+1})\right)\end{aligned}\right\}, \tag{2.28}$$

$$\gamma_{g,r} = \chi^{p}_{g,r}(1-\beta_r) + \sum_j \chi^{d}_{j,g,r}\lambda_j\xi_j\ , \tag{2.29}$$

$$\begin{aligned}\hat{S}_{g,m,k,i}(s,t_n) = \frac{1}{4\pi}\Bigg\{&\frac{\phi_{g,r}(t_n)}{v_{g,r}\Delta t_{shape}}\frac{P_{g,I}(t_{n+1})}{P_{g,I}(t_n)} \\ &+\sum_j \chi^{d}_{j,g,r}\lambda_j\left(\mu_j C_{j,m,k,i}(s,t_n) + \eta_j\sum_{g'}\nu\Sigma_{f,g',r}(t)\phi_{g',m,k,i}(s,t_n)\right)\Bigg\}.\end{aligned} \tag{2.30}$$

Note that Equation (2.27) is a balance equation for the angular flux. In the MAF method, Equation (2.27) is used for the kinetic calculation, and it enables us to eliminate the normalization of the shape function.

2.2.2. Fine step calculation in coarse geometry

The purpose of the fine time step calculation in a coarse geometry is to obtain the amplitude function and the dynamic frequency that reflect fine temporal dependence. From their definition, they can be calculated from the scalar flux in the coarse geometry as follows:

$$P_{g,I}(t) \equiv \int_{V_I}\frac{\phi_g(\vec{r},t)}{v_g(\vec{r})}dV = \frac{\int_{V_I}\frac{\phi_g(\vec{r},t)}{v_g(\vec{r})}dV}{\int_{V_I}\phi_g(\vec{r},t)dV}\int_{V_I}\phi_g(\vec{r},t)dV = \frac{V_I}{v^{CM}_{g,I}}\phi^{CM}_{g,I}(t)\,, \tag{2.31}$$

$$\omega_{g,I}(t) \equiv \frac{1}{P_{g,I}(t)}\frac{dP_{g,I}(t)}{dt} = \frac{1}{\phi^{CM}_{g,I}(t)}\frac{d\phi^{CM}_{g,I}(t)}{dt}\ . \tag{2.32}$$

where $v^{CM}_{g,I}$ and $\phi^{CM}_{g,I}$ are the averaged neutron velocity and the scalar flux in a coarse mesh defined as follows:

$$v_{g,I}^{CM} \equiv \int_{V_I} \frac{\phi_g(\vec{r},t)}{v_g(\vec{r})} dV \Big/ \int_{V_I} \phi_g(\vec{r},t) dV \,, \tag{2.33}$$

$$\phi_{g,I}^{CM}(t) \equiv \frac{1}{V_I} \int_{V_I} \phi_g(\vec{r},t) dV \,, \tag{2.34}$$

To calculate the fine temporal variation of the scalar flux in the coarse geometry, the time-dependent coarse mesh finite difference (TCMFD) method [8] is employed in the present study.

In the TCMFD method, integrating both sides of Equation (2.6) for total solid angle and spatially averaging it within each coarse mesh I, the left side of Equation (2.6) is described as

$$\frac{1}{V_I} \int_{V_I} \int_{4\pi} \frac{1}{4\pi} \frac{1}{v_g(\vec{r})} \frac{\partial \phi_g(\vec{r},t)}{\partial t} d\Omega dV = \frac{d}{dt} \int_{V_I} \frac{1}{V_I} \frac{\phi_g(\vec{r},t)}{v_g(\vec{r})} dV = \frac{1}{v_{g,I}^{CM}} \frac{d\phi_{g,I}^{CM}(t)}{dt} \,, \tag{2.35}$$

The right side of Equation (2.6) is described as

$$\begin{aligned} &\frac{1}{V_I} \left(\begin{matrix} -\int_{V_I} \int_{4\pi} \vec{\Omega} \cdot \nabla \psi_g(\vec{r},\vec{\Omega},t)\, d\Omega dV - \int_{V_I} \int_{4\pi} \Sigma_{t,g}(\vec{r},t) \psi_g(\vec{r},\vec{\Omega},t) d\Omega dV \\ + \int_{V_I} \int_{4\pi} Q_g(\vec{r},t) d\Omega dV \end{matrix} \right) \\ &= -\frac{1}{V_I} \int_{S_I} \int_{4\pi} \vec{\Omega} \psi_g(\vec{r},\vec{\Omega},t)\, d\Omega \cdot \vec{n} dS - \Sigma_{t,g,I}^{CM}(t) \phi_{g,I}^{CM}(t) + Q_{g,I}^{CM}(t) \\ &= -\frac{1}{V_I} \int_{S_I} \vec{J}_g(\vec{r},t) \cdot \vec{n} dS - \Sigma_{t,g,I}^{CM}(t) \phi_{g,I}^{CM}(t) + Q_{g,I}^{CM}(t) \,, \end{aligned} \tag{2.36}$$

where S_I and $\vec{n}$ denotes the surface of the coarse mesh I and the normal vector to the surface, respectively. $\Sigma_{t,g,I}^{CM}$, $Q_{g,I}^{CM}(t)$, and $\vec{J}_g(\vec{r},t)$ are described as:

$$\Sigma_{t,g,I}^{CM}(t) = \frac{\int_{V_I} \Sigma_{t,g}(\vec{r},t) \phi_g(\vec{r},t) dV}{\int_{V_I} \phi_g(\vec{r},t) dV} = \frac{\int_{V_I} \Sigma_{t,g}(\vec{r},t) \varphi_g(\vec{r},t) dV}{\int_{V_I} \varphi_g(\vec{r},t) dV} \,, \tag{2.37}$$

$$\begin{aligned} Q_{g,I}^{CM}(t) = \chi_{g,I}^{p,CM} (1 - \beta_I^{CM}) \sum_{g'} \nu \Sigma_{f,g',I}^{CM}(t) \phi_{g',I}^{CM}(t) + \sum_{g'} \Sigma_{s,g' \to g,I}^{CM}(t) \phi_{g',I}^{CM}(t) \\ + \sum_j \chi_{j,g,I}^{d,CM} \lambda_j C_{j,I}^{CM}(t) \,, \end{aligned} \tag{2.38}$$

$$\vec{J}_g(\vec{r},t) \equiv \int_{4\pi} \vec{\Omega}\, \psi_g(\vec{r},\vec{\Omega},t)\, d\Omega \,, \tag{2.39}$$

Finally, the balance equation in coarse geometry is derived as

$$\frac{1}{v_{g,I}^{CM}} \frac{d\phi_{g,I}^{CM}(t)}{dt} = -\frac{1}{V_I} \int_{S_I} \vec{J}_g(\vec{r},t) \cdot \vec{n} dS - \Sigma_{t,g,I}^{CM}(t) \phi_{g,I}^{CM}(t) + Q_{g,I}^{CM}(t) , \tag{2.40}$$

Since the amplitude function has a strong dependence on time, employing the theta method with a fine time step size Δt_{amp}, Equation (2.40) is described as

$$\begin{aligned} &\frac{1}{V_I} \int_{S_I} \vec{J}_g(\vec{r},t_{N+1}) \cdot \vec{n} dS + \left(\Sigma_{t,g,I}^{CM}(t_{N+1}) + \frac{1}{\theta v_{g,I}^{CM} \Delta t_{amp}} \right) \phi_{g,I}^{CM}(t_{N+1}) \\ &\qquad = \hat{Q}_{g,I}^{CM}(t_{N+1}) + \hat{S}_{g,I}^{CM}(t_N) , \end{aligned} \tag{2.41}$$

where N denotes the fine time step for amplitude functions. The neutron source terms are described as:

$$\begin{aligned} \hat{Q}_{g,I}^{CM}(t_{N+1}) = &\left\{ \chi_{g,I}^{p,CM} (1 - \beta_I^{CM}) + \sum_j \chi_{j,g,I}^{d,CM} \lambda_j \xi_j^{CM} \right\} \sum_{g'} \nu \Sigma_{f,g',I}^{CM}(t_{N+1}) \phi_{g',I}^{CM}(t_{N+1}) \\ &+ \sum_{g'} \Sigma_{s,g' \to g,I}^{CM}(t_{N+1}) \phi_{g',I}^{CM}(t_{N+1}) \ , \end{aligned} \tag{2.42}$$

$$\begin{aligned} \hat{S}_{g,I}^{CM}(t_{N+1}) = &\sum_j \chi_{j,g,I}^{d,CM} \lambda_j \left(\mu_j^{CM} C_{j,I}^{CM}(t_N) + \eta_j^{CM} \sum_{g^{\prime}} \nu \Sigma_{f,g^{\prime},I}^{CM}(t_N) \phi_{g^{\prime},I}^{CM}(t_N) \right) \\ &+ \frac{\phi_{g^{\prime},I}^{CM}(t_N)}{\theta v_{g,I}^{CM} \Delta t_{amp}} + \frac{1-\theta}{\theta} R_{g,I}^{CM}(t_N) , \end{aligned} \tag{2.43}$$

$$R_{g,I}^{CM}(t_N) = -\frac{1}{V_I} \int_{S_I} \vec{J}_g(\vec{r},t_N) \cdot \vec{n} dS - \Sigma_{t,g,I}^{CM}(t_N) \phi_{g,I}^{CM}(t_N) + Q_{g,I}^{CM}(t_N) \ , \tag{2.44}$$

$$\begin{aligned} C_{j,I}^{CM}(t_{N+1}) = &\mu_j^{CM} C_{j,I}^{CM}(t_N) + \eta_j^{CM} \sum_{g'} \nu \Sigma_{f,g',I}^{CM}(t_N) \phi_{g',I}^{CM}(t_N) \\ &+ \xi_j^{CM} \sum_{g'} \nu \Sigma_{f,g',I}^{CM}(t_{N+1}) \phi_{g',I}^{CM}(t_{N+1}) , \end{aligned} \tag{2.45}$$

Since the neutron current in Equation (2.41) must be consistent with that of MOC, with the coarse mesh finite difference (CMFD) approach [18], the neutron current between the coarse meshes, I and I+1, is defined as follows:

$$\begin{aligned} J_{g,I+1/2}^{CM}(t) = &-\frac{2 D_{g,I}^{CM}(t) D_{g,I+1}^{CM}(t)}{D_{g,I+1}^{CM}(t) h_I + D_{g,I}^{CM}(t) h_{I+1}} \left(\phi_{g,I+1}^{CM}(t) - \phi_{g,I}^{CM}(t) \right) \\ &+ D_{g,I+1/2}^{COR}(t) \left(\phi_{g,I+1}^{CM}(t) + \phi_{g,I}^{CM}(t) \right) \ , \end{aligned} \tag{2.46}$$

$$D_{g,I}^{CM}(t)=\frac{1}{3\Sigma_{tr,g,I}^{CM}}=\frac{1}{3}\frac{\int_{V_I}\phi_g(\vec{r},t)dV}{\int_{V_I}\Sigma_{tr,g}(\vec{r},t)\phi_g(\vec{r},t)dV}=\frac{1}{3}\frac{\int_{V_I}\varphi_g(\vec{r},t)dV}{\int_{V_I}\Sigma_{tr,g}(\vec{r},t)\varphi_g(\vec{r},t)dV}\ , \tag{2.47}$$

$$\begin{aligned} D_{g,I+1/2}^{COR}(t) &\equiv \frac{J_{g,I+1/2}^{MOC}(t)-J_{g,I+1/2}^{FDD}(t)}{\phi_{g,I+1}^{CM}(t)+\phi_{g,I}^{CM}(t)} \\ &= \frac{J_{g,I+1/2}^{MOC}(t)+\frac{2D_{g,I}^{CM}(t)D_{g,I+1}^{CM}(t)}{D_{g,I+1}^{CM}(t)h_I+D_{g,I}^{CM}(t)h_{I+1}}\left(\phi_{g,I+1}^{CM}(t)-\phi_{g,I}^{CM}(t)\right)}{\phi_{g,I+1}^{CM}(t)+\phi_{g,I}^{CM}(t)} \end{aligned} \tag{2.48}$$

where h, D^{CM}, and D^{COR} denote the coarse mesh width, the diffusion coefficient, and the correction factor to reproduce the neutron current of MOC, respectively. Using Equations (2.46)–(2.48), Equation (2.41) is described as a matrix form for the fixed source problem as

$$\mathbf{A}_{\boldsymbol{g}}^{\mathbf{CM}}(t_{N+1})\vec{\phi}_g^{CM}(t_{N+1})=\vec{Q}_g^{CM}(t_{N+1})+\vec{S}_g^{CM}(t_N) \tag{2.49}$$

Using Equation (2.49), the fine time step calculation in the coarse geometry is carried out.

2.2.3. Calculation flow

Combining the two kinetic schemes described in previous subsections, the kinetic calculation in the MAF method is carried out as shown in Figure 2.2. In Figure 2.2, the description of the convergence acceleration is omitted to clearly show the calculation flow of the MAF method.

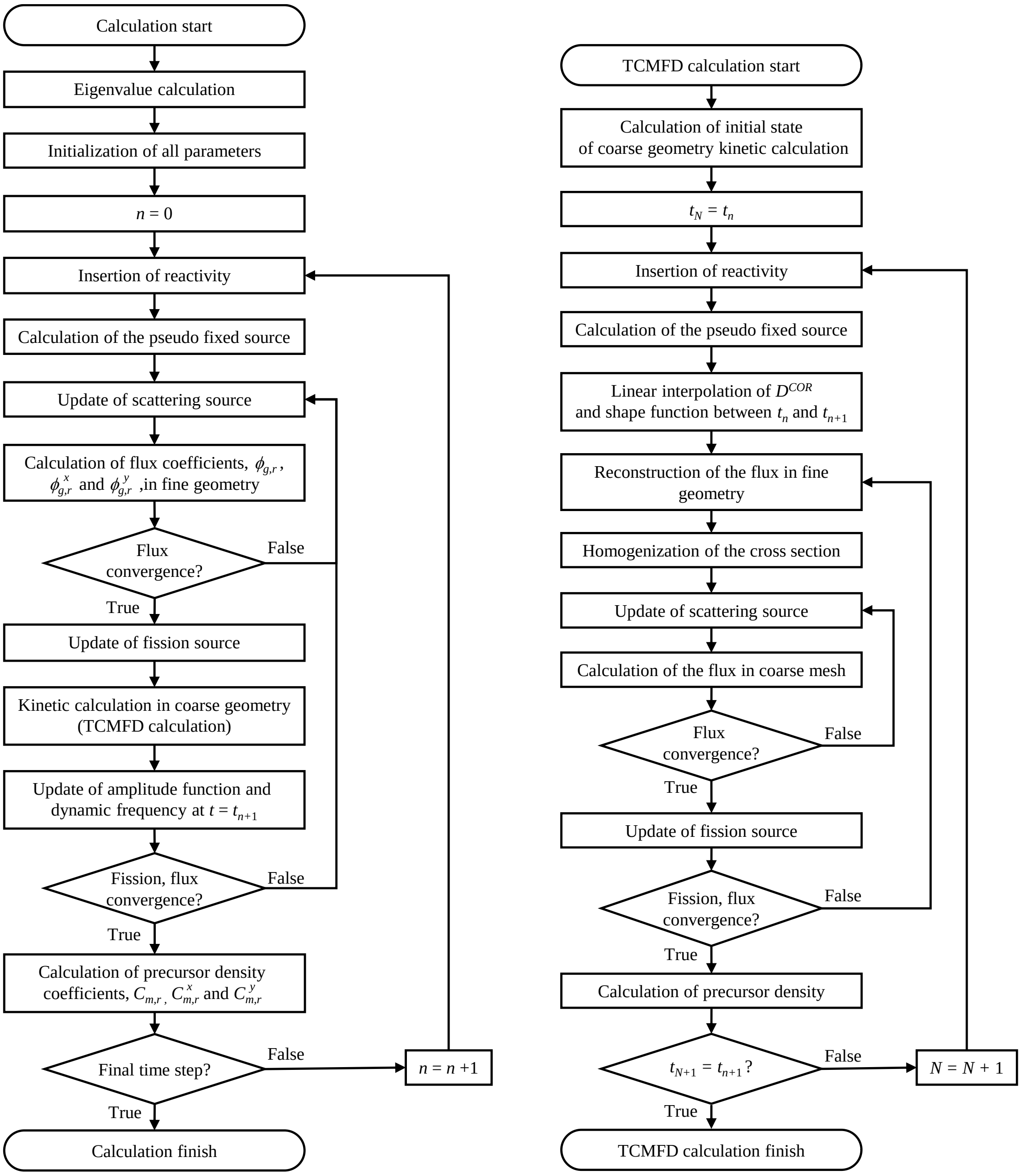

(a) Coarse time step calculation in the fine geometry

(b) Fine time step calculation in coarse geometry (TCMFD calculation)

Figure 2.2 Calculation flow of the MAF method

In the present study, the coarse time step kinetic calculation is carried out using MOC in the fine geometry with appropriate initial guesses for the amplitude function and the dynamic frequency, *i.e.*, the initial value of the amplitude function ratio $P_{g,I}(t_{n+1})/P_{g,I}(t_n)$ is 1.0 and that of dynamic frequency is 0.0. Once the neutron currents and the spatial expansion coefficients of the scalar fluxes are obtained, the fine time step kinetic calculation (TCMFD calculation) is carried out.

In the TCMFD calculation, the homogenized scalar fluxes and precursor densities at $t = t_n$ are calculated as an initial condition. Then, the kinetic calculation with the fine time step Δt_{amp} is carried out in the coarse geometry using Equation (2.49). However, the shape function, which is necessary to calculate the homogenized cross sections, and the correction factor of the neutron current are not calculated at the fine time step in the fine geometry as shown in Figure 2.3.

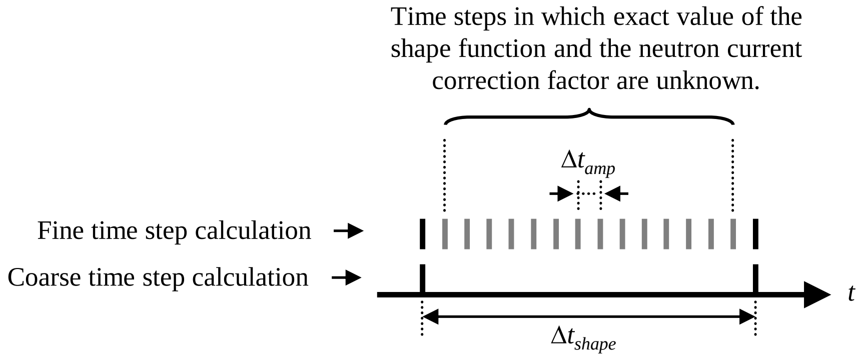

Figure 2.3 Time step discretization in the MAF method

Thus, they are linearly interpolated in each fine time step between the coarse time steps from $t = t_n$ to $t = t_{n+1}$ as follows [8]:

$$D^{COR}_{g,I+1/2}(t_{N+1}) = \frac{D^{COR}_{g,I+1/2}(t_{n+1}) - D^{COR}_{g,I+1/2}(t_n)}{\Delta t_{shape}}(t_{N+1} - t_n) + D^{COR}_{g,I+1/2}(t_n)\,, \tag{2.50}$$

$$\varphi_g(\vec{r}, t_{N+1}) = \frac{\varphi_g(\vec{r}, t_{n+1}) - \varphi_g(\vec{r}, t_n)}{\Delta t_{shape}}(t_{N+1} - t_n) + \varphi_g(\vec{r}, t_n)\,, \tag{2.51}$$

When the TCMFD calculation is finished until $t = t_{n+1}$, the amplitude functions and the dynamic frequencies at $t = t_{n+1}$ are calculated by Equations (2.31) and (2.32) to reflect fine temporal dependence for the MOC calculation. The temporal derivative of the coarse-mesh-averaged scalar flux, which is necessary to calculate the dynamic frequency, is calculated by Equation (2.40).

These calculations are iterated until the fission sources and scalar fluxes are sufficiently converged. Once the fluxes are sufficiently converged, precursor densities at $t = t_{n+1}$ are calculated and proceed to the next time step.

In the MAF method, the kinetic calculation with the fine time step in fine geometry is separated into "fine time step kinetic calculation in the coarse geometry" and "coarse time step kinetic calculation in the fine geometry" by factorizing the scalar flux. These calculations have less computational cost than that of the fine time step and the fine mesh calculation. Especially, since the TCMFD method is based on the diffusion theory and is much faster than the MOC calculation, a reduction in the number of the MOC calculations can have a large impact on the computational time. In addition, since the homogenized cross sections are calculated at each fine time step using the interpolated shape function calculated in fine geometry, the reduction of the number of flux regions by the linear source approximation also contributes to reducing the computational cost of the cross section homogenization during the TCMFD calculation. Therefore, the present scheme has the potential to provide an efficient computation scheme for kinetic calculation using MOC.

2.3. Numerical results

In this section, the effectiveness of the present scheme is verified. Two 2D benchmark problems, *i.e.*, the transport extension of the TWIGL seed blanket problem [15] and the C5G7-TD 2D benchmark problem [16], are calculated for the fundamental verification of the present scheme in the present verification. The calculation results of the TWIGL and C5G7-TD 2D benchmark problems are described in Subsections 2.3.1 and 2.3.2, respectively. Each subsection has two types of separated subsubsections.

The Subsubsections, 2.3.1.1 and 2.3.2.1, show the verification of the accuracy of the temporal integration of the present scheme. It is verified through the comparison between the present scheme and the conventional fully implicit method, *i.e.*, the temporal derivative of the scalar flux is directly discretized with fine time step without the MAF method. In the present calculations, the linear source approximation is also employed for the conventional fully implicit scheme, and the temporal derivative of the 1st order coefficients of the scalar flux are not taken into account as same as the present scheme. Thus, the present comparison shows the difference comes from different temporal integration methods.

The Subsubsections, 2.3.1.2 and 2.3.2.2, show the verification of the accuracy of the spatial discretization of the present scheme. It is verified through the comparison between the present scheme and the conventional MAF method with the flat source approximation. The present comparison shows the impact of the linear source approximation. In addition, the approximation error for the temporal derivative of the 1st-order coefficients of the scalar flux is confirmed.

All calculations are carried out by Intel(R) Core$^{\mathrm{TM}}$ i9-9900K (3.6–5.0GHz, 8core-16thread) with 16 GB memory. Parallel calculation based on ray-trace-wise decomposition is carried out using 16 threads for the MOC calculation. The TCMFD calculation is not parallelized in the present calculations.

2.3.1. TWIGL benchmark problem

The TWIGL benchmark problem has been widely used as a 2D test problem for time-dependent diffusion calculation [19]. However, a specification for the transport calculation is also proposed [15]. Figure 2.4 shows the top view of the TWIGL benchmark problem for transport calculation. The perturbed seed and the unperturbed seed regions have an identical cross section at the initial state. The material properties are provided in Table 2.1, where the number of the neutron energy groups is two and that of the delayed precursor group is one.

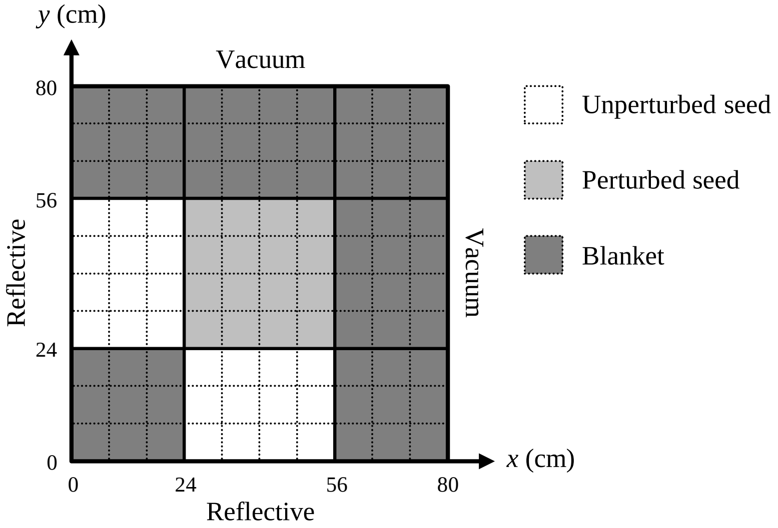

Figure 2.4 Top view for the TWIGL benchmark problem for transport calculations

Table 2.1 Material properties of the TWIGL benchmark problem for transport calculations

Material	Energy group	$\Sigma_{tr,g}$ (1/cm)	$\Sigma_{a,g}$ (1/cm)	$\nu\Sigma_{f,g}$ (1/cm)	$\Sigma_{s,g\rightarrow 1}$ (1/cm)	$\Sigma_{s,g\rightarrow 2}$ (1/cm)	χ_g (-)
Seed	1	0.23810	0.01000	0.00700	0.21810	0.01000	1.0
	2	0.83333	0.15000	0.20000	0.00000	0.68333	0.0
Blanket	1	0.25641	0.00800	0.00300	0.23841	0.01000	1.0
	2	0.66667	0.05000	0.06000	0.00000	0.61667	0.0
	ν	v_1(cm/sec)	v_2(cm/sec)	β (-)	λ (1/sec)		
	2.43	10^7	2×10^5	0.0075	0.08		

In the TWIGL benchmark problem, two cases of reactivity perturbations are provided, *i.e.*, the step and the ramp perturbations as follows:

$$\text{Step perturbation} \quad : \quad \Sigma_{a,2}^{PS}(t) = \Sigma_{a,2}^{PS}(0) - 0.0035 \ (t > 0)\,, \tag{2.52}$$

$$\text{Ramp perturbation} \quad : \quad \Sigma_{a,2}^{PS}(t) = \begin{cases} \Sigma_{a,2}^{PS}(0)(1 - 0.116667t) & (t \le 0.2) \\ 0.976666\Sigma_{a,2}(0) & (t > 0.2) \end{cases}, \tag{2.53}$$

where $\Sigma_{a,2}^{PS}$ denotes the 2nd energy group absorption cross section of the perturbed seed region in

Figure 2.4.

2.3.1.1. Verification for temporal discretization

In the present verification, the accuracy of the present scheme for temporal integration is verified. Table 2.2 shows the calculation conditions of the present verification.

Table 2.2 Calculation conditions of the TWIGL benchmark problem (MAF vs FI)

Parameters	Calculation conditions
Azimuthal division	64 for 2π with cyclic quadrature set [1]
Polar division	3 for $\pi/2$ with TY-opt quadrature set [20]
Ray separation	0.02 cm using cyclic ray tracing
Convergence criterion	Fission : 10^{-8}, flux : 5×10^{-8}
Flux region division	0.5 cm × 0.5 cm square mesh
Source approximation	Linear

Test cases	FI	MAF+FI	MAF+CN	Reference solution
Time discretization*	FI for the scalar flux	FI for SF FI for AF	FI for SF CN for AF	FI for the scalar flux
Time step size	Δt = 1,10,100 msec	Δt_{shape}= 100 msec Δt_{amp} = 1,10 msec	Δt_{shape}= 100 msec Δt_{amp} = 1,10 msec	Δt = 0.1 msec
Coarse mesh for amplitude function	-	1 cm × 1 cm square mesh	1 cm × 1 cm square mesh	-

* FI : fully implicit method, CN : Crank-Nicolson method [21],

SF : shape function, AF : amplitude function

As shown in Table 2.2, there are three test cases, *i.e.*, FI, MAF+FI, and MAF+CN. The test case, FI, is calculated with the conventional fully implicit method without the MAF method, *i.e.*, the scalar flux is directly discretized for time without factorization. The test cases, MAF+FI and MAF+CN, are calculated with the MAF method, *i.e.*, the scalar flux is factorized into the amplitude and shape functions. The shape function is discretized by the fully implicit method for both cases, but the theta method with $\theta = 1$ (fully implicit method) and $\theta = 0.5$ (Crank-Nicolson method) are employed for the coarse-mesh fine time step calculation for MAF+FI and MAF+CN, respectively. As for the precursor density calculation, the analytical solution of the balance equation for the precursor density, which is derived assuming the linear transition of the fission source between the time steps [21], is employed for the test case FI and the TCMFD calculation of the MAF method. The reference solution is calculated with the fully implicit method using the finest time step size, $\Delta t = 0.1$ msec. In the present verification, the linear source approximation is employed for all test cases to see only temporal discretization errors.

In the present verification, the accuracy with respect to the reference solution and the computation time of the MAF method is compared with those of the conventional method. Figure 2.5 shows the reference solutions for the step and ramp perturbations. The initial k-effective is 0.916117 in the present calculation condition.

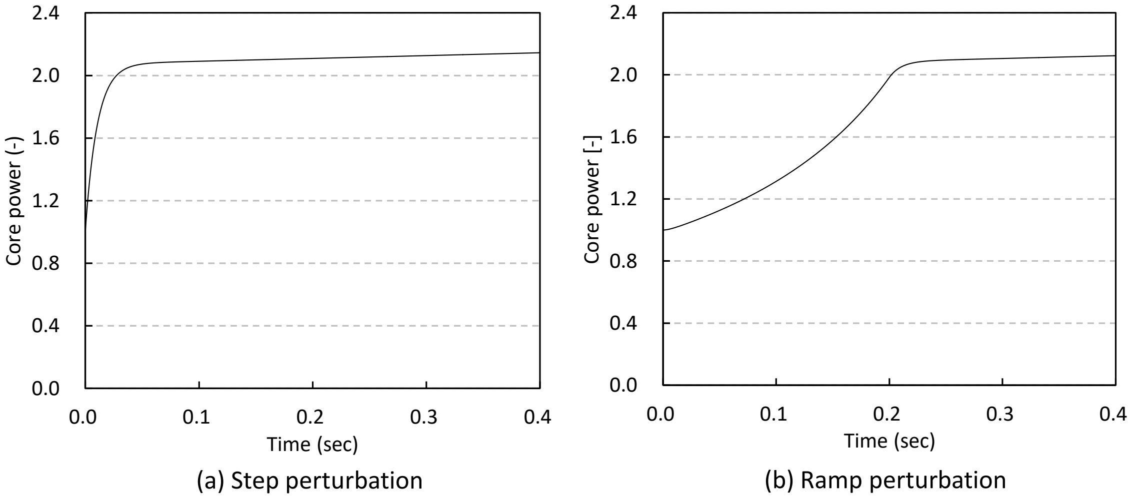

(a) Step perturbation (b) Ramp perturbation

Figure 2.5 Reference solution for the TWIGL benchmark problem

Figure 2.6 shows the transition of the relative difference for the core power, which is calculated as:

$$\text{Relative difference for core power (\%)} = \frac{CP - CP^{ref}}{CP^{ref}} \times 100\,, \tag{2.54}$$

where CP and ref denote the core power and the reference solution, respectively. In Figure 2.6, Δt_{FI} denotes the time step size for the conventional fully implicit method.

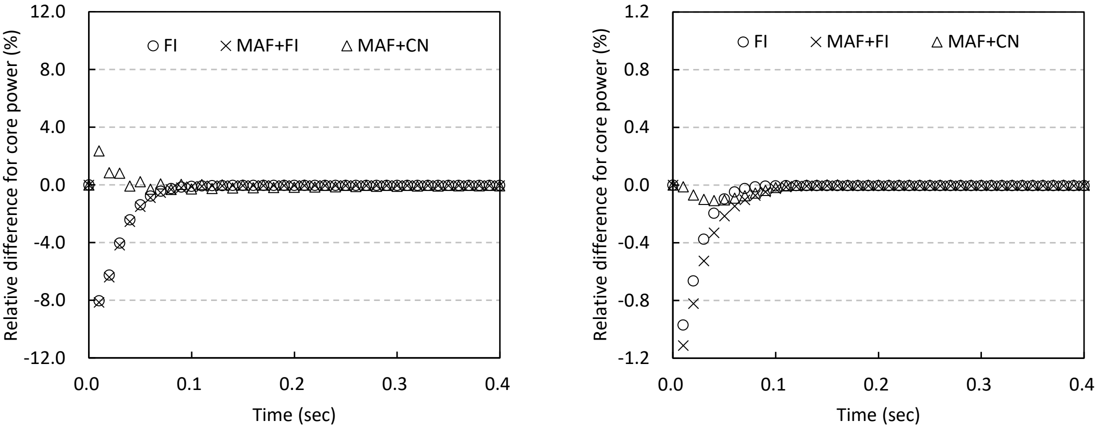

(a) Step perturbation, Δt_{FI} =Δt_{amp} = 10 msec

(b) Step perturbation, Δt_{FI}=Δt_{amp} = 1 msec

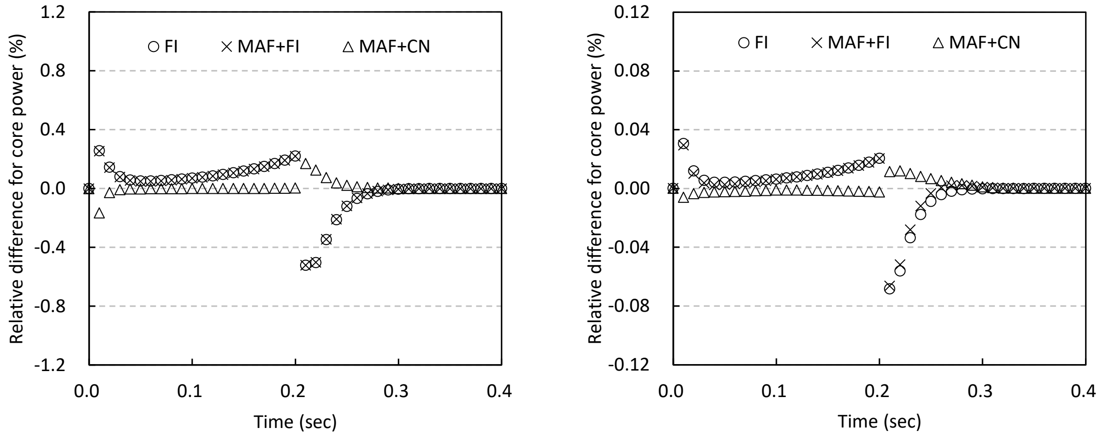

(c) Ramp perturbation, Δt_{FI}=Δt_{amp} = 10 msec

(d) Ramp perturbation, Δt_{FI}=Δt_{amp} = 1 msec

Figure 2.6 Time step dependence for the TWGL benchmark problem (MAF vs FI)

Comparing the calculation cases MAF+FI with FI, the MAF method almost reproduces the dependence for the time step of the conventional method (FI) although the time step size for the shape function (100 msec) is much larger than that of the conventional one (1 or 10 msec). It suggests that a major part of the temporal dependence of the scalar flux can be captured by the amplitude function, and that of the shape function has less impact on the temporal dependence of the scalar flux.

A comparison between MAF+CN and FI has a more noticeable trend, which shows the different trends among the test cases. Since the test case, MAF+CN, uses the theta method with θ = 0.5 for the fine time step kinetic calculation in the coarse geometry, the amplitude function reflects less temporal discretization error. As a result, it reproduces the reference solution more accurately. From another viewpoint, the test case MAF+CN has one more important feature about the implementation of the theta method for time-dependent MOC calculations. Applying the theta method for Equation (2.7), it is described as:

$$\frac{1}{4\pi}\frac{1}{v_{g,r}}\frac{\phi_{g,m,k,i}(s,t_{n+1})-\phi_{g,m,k,i}(s,t_n)}{\Delta t} \\ =\theta R_{g,m,k,i}(s,t_{n+1})+(1-\theta)R_{g,m,k,i}(s,t_n)\,, \tag{2.55}$$

where

$$R_{g,m,k,i}(s,t)=-\frac{\partial\psi_{g,m,k,i}(s,t)}{\partial s}-\Sigma_{t,g,r}(t)\psi_{g,m,k,i}(s,t)+Q_{g,m,k,i}(s,t)\,, \tag{2.56}$$

The leakage term at the previous time step included in Equation (2.56) is hard to store in complicated geometries. Thus, considering the previous time step for Equation (2.27) as shown in Equation (2.57) and substituting it into Equation (2.56), the residual term is described as Equation (2.58) [22].

$$\frac{\partial\psi_{g,m,k,i}(s,t_n)}{\partial s}+\Sigma_{t,g,r}(t_n)\psi_{g,m,k,i}(s,t_n)=\hat{Q}_{g,m,k,i}(s,t_n)+\hat{S}_{g,m,k,i}(s,t_{n-1})\,, \tag{2.57}$$

$$R_{g,m,k,i}(s,t_n)=-\hat{Q}_{g,m,k,i}(s,t_n)-\hat{S}_{g,m,k,i}(s,t_{n-1})+Q_{g,m,k,i}(s,t_n)\,, \tag{2.58}$$

However, this derivation implicitly approximates the angular dependence of the residual term as isotopic. In addition, since the pseudo source at $(n-1)$th step is not defined at n = 0, the residual term is generally assumed as zero (= steady-state). This assumption causes the degradation of the accuracy at the step perturbation condition because the temporal derivative of the scalar flux is underestimated in such a case. On the other hand, the leakage term at the previous time step can be directly calculated within the TCMFD framework using neutron currents because it is based on diffusion theory. Therefore, no approximation is necessary for the residual term at the previous time step in the present scheme and it becomes an advantage for implementation easiness of the theta method for kinetics calculation codes using MOC.

Finally, the computation time of each test case is described in Table 2.3. Note that the speed-up ratio in Table 2.3 is defined as the ratio of the computation time of the conventional fully implicit method and the present method in $\Delta t_{FI}=\Delta t_{amp}$ condition, where the accuracy of them becomes almost same as shown in Figure 2.6. It indicates the degree of computation time reduction to achieve the same accuracy.

Table 2.3 Computation time for the TWIGL benchmark problem (MAF vs FI)

(a) Step perturbation

Test cases	FI			MAF+FI		MAF+CN	
Time step width (msec) (Shape/Amp. for MAF)	1	10	100	100/1	100/10	100/1	100/10
Computation time (min)	54.4	9.2	1.8	2.3	1.8	2.4	2.0
Speed up (FI/MAF)*	-	-	-	23.8	5.1	22.7	4.7

* Comparison in $\Delta t_{FI} = \Delta t_{amp}$ condition

(b) Ramp perturbation

Test cases	FI			MAF+FI		MAF+CN	
Time step width (msec) (Shape/Amp. for MAF)	1	10	100	100/1	100/10	100/1	100/10
Computation time (min)	71.4	11.0	1.9	2.5	1.9	2.5	1.9
Speed up (FI/MAF)*	-	-	-	28.5	5.8	28.2	5.7

* Comparison in $\Delta t_{FI} = \Delta t_{amp}$ condition

Table 2.3 indicates that the computation time of the MAF method is shorter than that of the conventional one to achieve the same accuracy. The maximum speedup ratio in the present verification is 28.5. These calculation results suggest the effectiveness of the present scheme.

2.3.1.2. Verification for spatial discretization

In the present verification, the accuracy of the present scheme for spatial discretization is verified. Table 2.4 shows the calculation conditions of the present verification.

Table 2.4 Calculation conditions of the TWIGL benchmark problem (LS vs FS)

Parameters	Calculation conditions				
Azimuthal division	64 for 2π with cyclic quadrature set [1]				
Polar division	3 for $\pi/2$ with TY-opt quadrature set [20]				
Ray separation	0.02 cm using cyclic ray tracing				
Convergence criterion	Fission : 10^{-8}, flux : 5×10^{-8}				
Time discretization	The MAF method (Fully implicit method for the shape function and the TCMFD calculation)				
Time step size	Δt_{shape} = 100 msec, Δt_{amp} = 1 msec				
Coase mesh structure for amplitude function	1 cm x 1cm square mesh				
Test cases	FS1	FS2	FS3	FS4	LS
Source approximation	Flat	Flat	Flat	Flat	Linear
Flux region division inside 1cm x 1cm mesh	2×2 meshes	4×4 meshes	8×8 meshes	16×16 meshes	2×2 meshes

As shown in Table 2.4, there are five test cases, *i.e.*, FS1, FS2, FS3, FS4, and LS. The test cases FS1–FS4 are calculated with the conventional flat source approximation using the different flux region structures. The test case, LS, is calculated with the linear source approximation. For all test cases, the MAF method is employed for the temporal integration of the scalar flux and the precursor density, where the shape and amplitude functions for them are discretized by the fully implicit method for all cases. As for the precursor density, the analytical solution of the balance equation for the precursor density, which is derived assuming the linear transition of the fission source between the time steps [21], is employed for all TCMFD calculations. The finest test case calculated with the conventional flat source approximation, FS4, is assumed as a reference solution in the present verification.

Table 2.5 shows the initial eigenvalue and the inserted reactivity for each test case.

Table 2.5 Initial eigenvalue and inserted reactivity for the TWIGL benchmark problem

Test cases	FS1	FS2	FS3	FS4	LS
Initial k_{eff}	0.915916	0.916066	0.916104	0.916114	0.916117
k_{eff} (after perturbation)	0.919481	0.919633	0.919672	0.919682	0.919685
Inserted reactivity (pcm)	423.3	423.4	423.5	423.5	423.5

Figure 2.7 shows the transition of the relative difference for the core power, which is calculated as:

$$\text{Relative difference for core power (\%)} = \frac{CP - CP^{ref}}{CP^{ref}} \times 100\,. \tag{2.59}$$

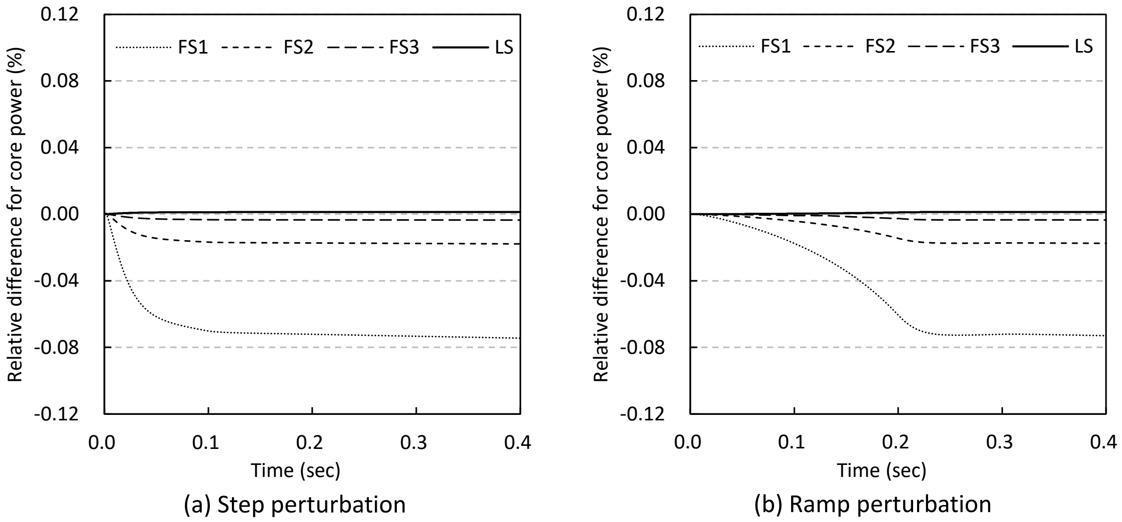

Figure 2.7 Transition of the core power difference for the TWIGL benchmark problem (LS vs FS)

As shown in Table 2.5 and Figure 2.7, the initial eigenvalue, inserted reactivity, and the core power transitions calculated with the flat source approximation asymptotically approach those of the reference solution by reducing the flux region size but very fine spatial mesh structure is required to reproduce reference solution. On the other hand, the linear source approximation almost reproduces the reference solution with the coarser mesh structure. It indicates the spatial discretization error is accurately reduced by the linear source approximation. In addition, although the linear source calculation includes the approximation error for the temporal derivatives of the 1st order coefficients of the scalar flux, which are assumed as zero in the present study, it has a negligible impact on the accuracy of the core power transition as the liner source calculation reproduces the reference solution.

Table 2.6 shows the computation time of each test case.

Table 2.6 Computation time for the TWIGL benchmark problem (LS vs FS)

Test cases	FS1	FS2	FS3	FS4	LS
Step perturbation (min)	1.2	2.4	6.5	22.2	2.3
Ramp perturbation (min)	1.4	3.0	8.0	25.9	2.5

As shown in Table 2.6, the linear source approximation achieves about 10 times faster computation than the reference solution while achieving the same accuracy. It suggests the effectiveness of the present scheme.

2.3.2. C5G7-TD 2D benchmark problem

The C5G7-TD 2D benchmark problem [16] is developed as the kinetic extension for the C5G7 benchmark problem [23], which is widely used for the verifications of deterministic transport calculation codes. It consists of two UO_2 and MOX PWR heterogeneous fuel assemblies surrounded by water reflectors as shown in Figures 2.8 and 2.9. Since the spatial gradient of the flux distributions is quite large in the present benchmark problem due to the difference in the neutron spectrum among the UO_2, MOX, and reflector, a large number of spatial meshes are required in the conventional flat source approximation, *i.e.*, improvement of the spatial discretization by the linear source approximation in the present calculation scheme is verified in this subsection.

The cross sections for seven energy groups and the delayed neutron parameters for 8 precursor groups for each material are specified in the benchmark problem and they are used in the present verification. In the C5G7-TD 2D benchmark problem, 3 exercises, TD1–TD3, are provided for the 2D benchmark calculations.

(1) TD1 : 1% control rod insertion and withdrawal transient
(2) TD2 : 10% control rod insertion and withdrawal transient
(3) TD3 : Moderator density change transient

Each exercise includes multiple test problems with different perturbation conditions, *i.e.*, TD1-1–

TD3-4, which are shown in Table 2.7 [16]. In all test problems, the cross sections linearly vary for t = 0.0 sec – 1.0 sec and 1.0 sec – 2.0 sec as shown in Figure 2.10. The perturbation condition in the present verification is TD1-1, which is the 1% control rod insertion and withdrawal perturbation for the upper left UO_2 assembly. The detailed calculation results for the other perturbation conditions are described in Appendix.

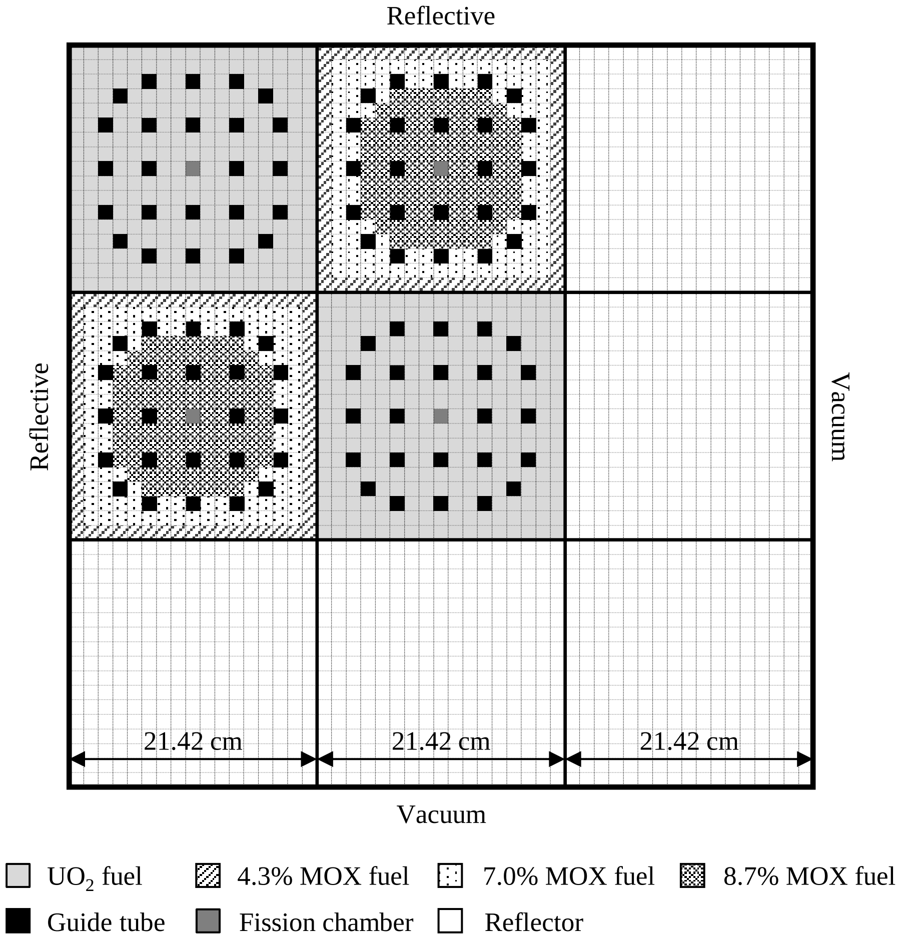

Figure 2.8 Top view for the C5G7-TD 2D benchmark problem

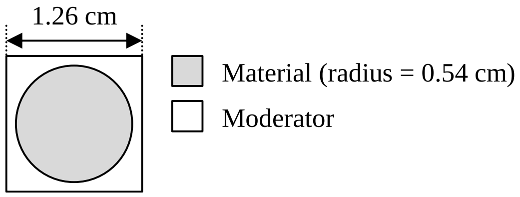

Figure 2.9 pin cell layout

Table 2.7 Perturbation conditions in the C5G7-TD 2D benchmark problem

Test problem	Perturbation	Perturbed assemblies/regions
TD 1-1	1 % control rod insertion and withdrawal	Upper left UO_2 assembly
TD 1-2	1 % control rod insertion and withdrawal	Lower left MOX assembly
TD 1-3	1 % control rod insertion and withdrawal	Lower right UO_2 assembly
TD 1-4	1 % control rod insertion and withdrawal	Fuel assemblies except for upper right UO_2 assembly
TD 1-5	1 % control rod insertion and withdrawal	All fuel assemblies
TD 2-1	10 % control rod insertion and withdrawal	Upper left UO_2 assembly
TD 2-2	10 % control rod insertion and withdrawal	Lower left MOX assembly
TD 2-3	10 % control rod insertion and withdrawal	Lower right UO_2 assembly
TD 3-1	5% moderator density decrease and increase	Moderator region*
TD 3-2	10% moderator density decrease and increase	Moderator region*
TD 3-3	15% moderator density decrease and increase	Moderator region*
TD 3-4	20% moderator density decrease and increase	Moderator region*

* Reflector is not affected.

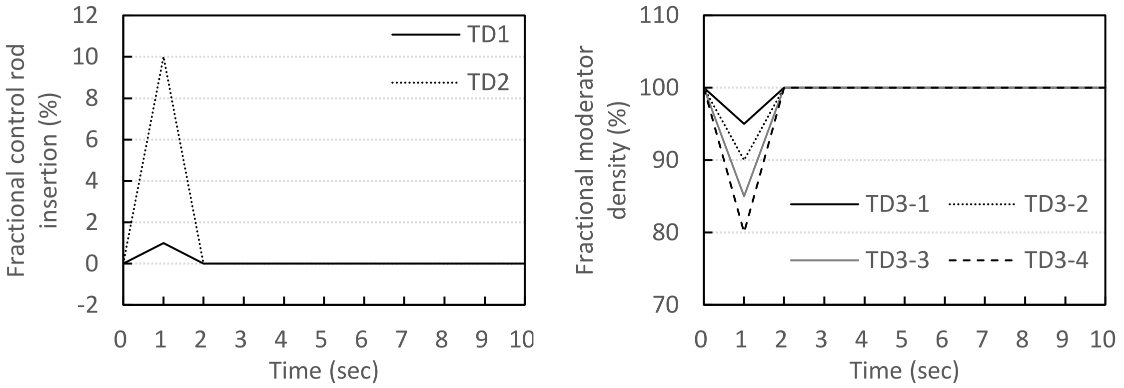

(a) Control rod movements (b) Moderator density transitions

Figure 2.10 Perturbations in the C5G7-TD 2D benchmark problem

2.3.2.1. Verification for temporal discretization

In the present verification, the accuracy of the present scheme for temporal integration is verified. Table 2.8 and Figure 2.11 show the calculation conditions and the spatial discretization of the present calculation, respectively.

Table 2.8 Calculation condition of TD 1-1 (MAF vs FI)

Parameters	Calculation conditions	
Azimuthal division	128 for 2π with cyclic quadrature set [1]	
Polar division	3 for $\pi/2$ with TY-opt quadrature set [20]	
Ray separation	0.01 cm using cyclic ray tracing	
Convergence criterion	Fission : 10^{-6} flux : 10^{-6}	
Flux region division	Reflector cell : 0.42 cm × 0.42 cm square mesh Other cells : material boundary + 8 azimuthal division (as shown in Figure 2.11)	
Initial core power	1.0	
Source approximation	Linear	
Test cases	FI	MAF
Time discretization	Fully implicit method for the scalar flux	Fully implicit method for the shape and amplitude functions
Time step size	Δt = 10, 100, 1000 msec	Δt_{shape} = 1000 msec, Δt_{amp} = 10, 100 msec
Coarse mesh size for amplitude function	-	1.26 cm × 1.26 cm square mesh

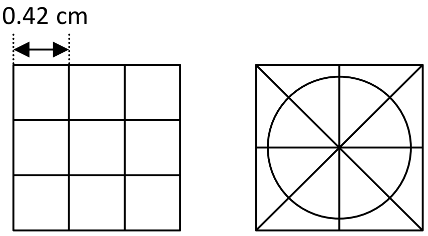

(a) Reflector cell (b) Fuel/GT/IT cells

Figure 2.11 Flux region discretization for the C5G7-TD 2D benchmark problem

The test case, FI, is calculated with the conventional fully implicit method without the MAF method, *i.e.*, the scalar flux is directly discretized for time without factorization. The test case, MAF, is calculated with the MAF method, *i.e.*, the scalar flux is factorized into the amplitude and shape functions. A larger enough time step size is used for the shape function than the amplitude function. In the test case, MAF, the fully implicit method is used for the fine time step diffusion calculation in the coarse mesh geometry. As for the precursor density calculation, the analytical solution of the balance equation for the precursor density, which is derived assuming the linear transition of the fission source between the time steps [21], is employed for the test case, FI, and the TCMFD calculation of the MAF method. In the present verification, the linear source approximation is employed for all test cases to see only temporal discretization errors.

The initial k-effective is 1.186538 in the present calculation condition. Compared to the reference MCNP5 solution for the eigenvalue, which is provided as 1.18646 ± 0.07% [16], the relative difference is +7 pcm. Figure 2.12 shows the transition and the relative difference for core power for the test case, FI, where the relative difference is calculated as

$$\text{Relative difference for core power (\%)} = \frac{CP - CP^{ref}}{CP^{ref}} \times 100\,, \tag{2.60}$$

where the solution of the test case, FI with $\Delta t = 10$ msec, is treated as the reference solution in the present comparison.

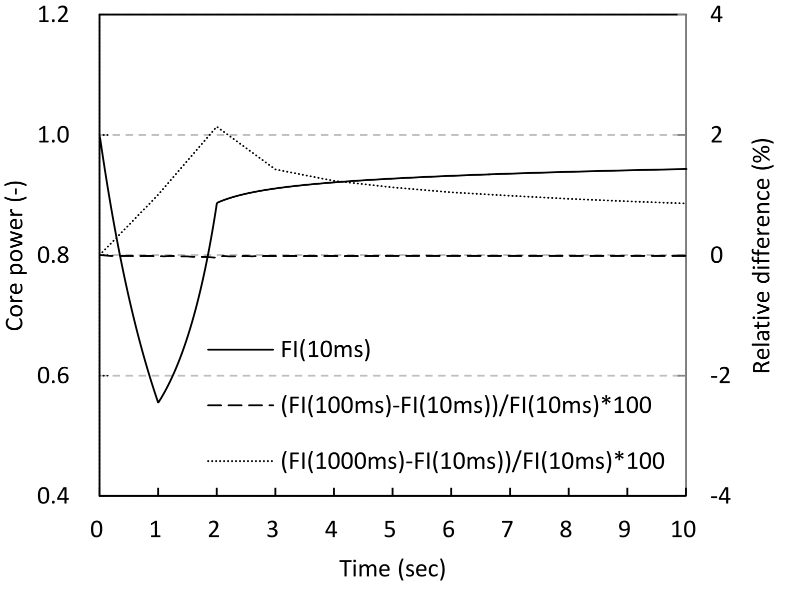

Figure 2.12 Time step dependence of the fully implicit method for TD 1-1

As shown in Figure 2.12, the temporal discretization error almost converges less than 0.1% at Δt = 100 msec. Thus, the test case, FI, with Δt = 10 msec is sufficiently fine as a reference solution. The test case, MAF, also reproduces the power transition as shown in Figure 2.13, where the relative difference for the core power and pin power with respect to those of the test case, FI, are calculated as follows:

$$\text{Relative difference for core power (\%)} \quad = \frac{CP - CP^{FI}}{CP^{FI}} \times 100\,, \tag{2.61}$$

$$\text{Relative difference for pin power (\%)} \quad = \max\left(\frac{P_i^{MAF} - P_i^{FI}}{P_i^{FI}} \times 100\right), \tag{2.62}$$

where P_i denotes the pin power at cell i. The superscript, MAF and FI, denote the solution of the MAF and fully implicit methods, respectively.

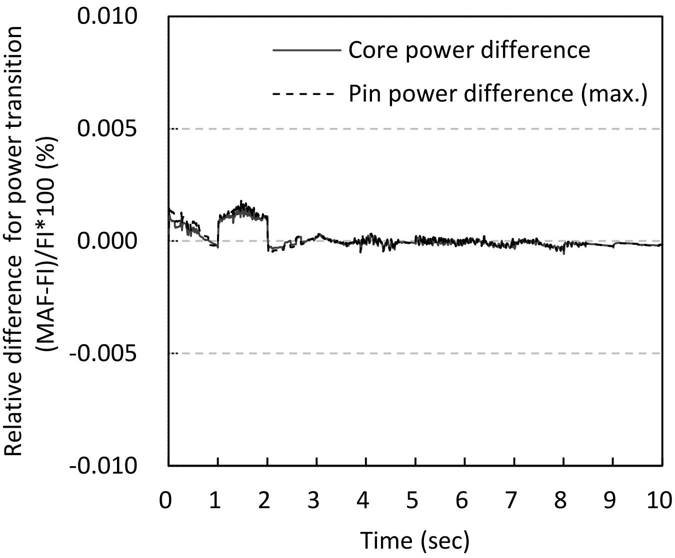

(a) $\Delta t_{FI} = \Delta t_{amp} = 10$ msec

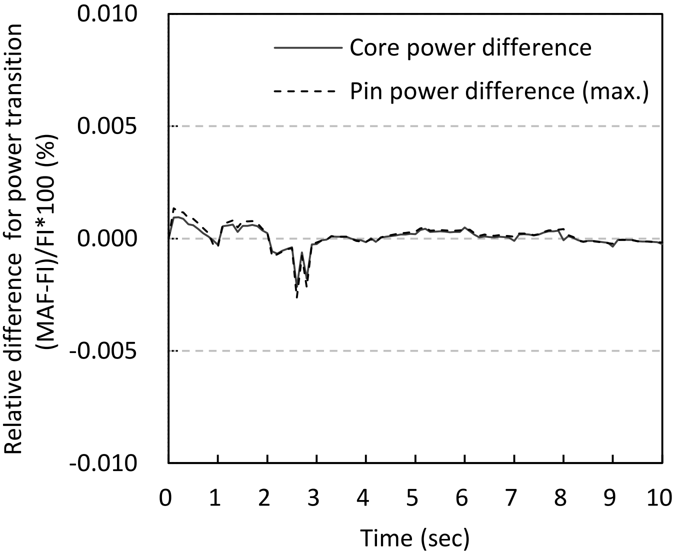

(b) $\Delta t_{FI} = \Delta t_{amp} = 100$ msec

Figure 2.13 Comparison of the power transition for TD 1-1 (MAF vs FI)

Figure 2.13 indicates that the homogenization and the spatial correction for the TCMFD calculation are accurately carried out and the linear interpolations for the shape function and the correction factor of neutron current have less impact on the accuracy.

Table 2.9 shows the computation time for each test case. Note that the speed-up ratio in Table 2.9 is defined as the ratio of the computation time of the conventional fully implicit method and the present method in $\Delta t_{FI} = \Delta t_{amp}$ condition to show the degree of computation time reduction to achieve the same accuracy.

Table 2.9 Computation time for TD 1-1 (MAF vs FI)

Test cases	FI			MAF	
Time step width (msec) (Shape/Amp. for MAF)	10	100	1000	1000/10	1000/100
Computation time (min)	2137	313	52	66	56
Speed up (FI/MAF)*	–	–	–	32.2	5.6

* Comparison in $\Delta t_{FI} = \Delta t_{amp}$ condition

As shown in Table 2.9, the MAF method enables much faster computation than the conventional method because computation time is dominated by the number of MOC calculations. Since the computational burden of the C5G7-TD 2D benchmark problem is much higher than that of the TWIGL benchmark problem, the speed-up ratio improves more than that of the TWIGL benchmark problem. These results show the effectiveness of the present scheme for time-dependent heterogeneous transport calculations using MOC.

2.3.2.2. Verification for spatial discretization

In the present verification, the accuracy of the present scheme for spatial discretization is verified. Table 2.10 and Figure 2.14 show the calculation conditions and the spatial discretization of the present calculation, respectively.

Table 2.10 Calculation conditions of TD 1-1 (LS vs FS)

Parameters	Calculation conditions
Azimuthal division	128 for 2π with cyclic quadrature set [1]
Polar division	3 for π/2 with TY-opt quadrature set [20]
Ray separation	0.01 cm using cyclic ray tracing
Convergence criterion	Fission : 10^{-6}, flux : 10^{-6}
Initial core power	1.0
Time discretization	The MAF method (Fully implicit method for the shape function and the TCMFD calculation)
Time step size	Δt_{shape} = 1000 msec, Δt_{amp} = 10 msec
Coarse mesh size for amplitude function	1.26 cm × 1.26 cm square mesh

Test cases	FS1	FS2	FS3	FS4	LS
Source approximation	Flat	Flat	Flat	Flat	Linear
Flux region division for reflector cells	4×4 meshes	8×8 meshes	16×16 meshes	24×24 meshes	3×3 meshes
Flux region division for fuel/GT/IT cells	4×4 meshes (Figure 2.14(a))	8×8 meshes (Figure 2.14(b))	16×16 meshes (Figure 2.14(c))	24×24 meshes (Figure 2.14(d))	Octant (Figure 2.11(b))

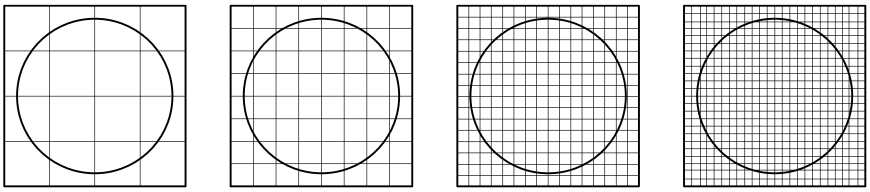

(a) 4x4 meshes (b) 8x8 meshes (c) 16x16 meshes (d) 24x24 meshes

Figure 2.14 Flat flux region discretization for the C5G7-TD 2D benchmark problem

As shown in Table 2.10, there are five test cases, *i.e.*, FS1, FS2, FS3, FS4, and LS. The test cases FS1–FS4 are calculated with the conventional flat source approximation using the different flux region structures. The test case, LS, is calculated with the linear source approximation. For all test cases, the MAF method is employed for the temporal integration of the scalar flux and the precursor density, where the shape and amplitude functions for them are discretized by the fully implicit method for all cases. As for the precursor density, the analytical solution of the balance equation for the precursor density, which is derived assuming the linear transition of the fission source between the time steps [21], is employed for all TCMFD calculations. The finest test case calculated with the conventional flat source approximation, FS4, is assumed as a reference solution in the present verification.

Table 2.11 shows the initial eigenvalue and the inserted reactivity for each test case.

Table 2.11 Initial eigenvalue and inserted reactivity for TD 1-1

Test cases	FS1	FS2	FS3	FS4	LS
Initial k_{eff}	1.186987	1.186723	1.186567	1.186533	1.186538
k_{eff} (after perturbation)	1.182419	1.182133	1.181968	1.181931	1.181936
Inserted reactivity (pcm)	-325.5	-327.2	-327.9	-328.2	-328.1

Figure 2.15 shows the transitions of the relative differences for the core power and the pin power, which are calculated as:

$$\text{Relative difference for core power (\%)} \quad = \frac{CP - CP^{ref}}{CP^{ref}} \times 100\,, \tag{2.63}$$

$$\text{Relative difference for pin power (\%)} \quad = \max\left(\frac{P_i - P_i^{ref}}{P_i^{ref}} \times 100\right). \tag{2.64}$$

where ref denotes the reference solution, FS4.

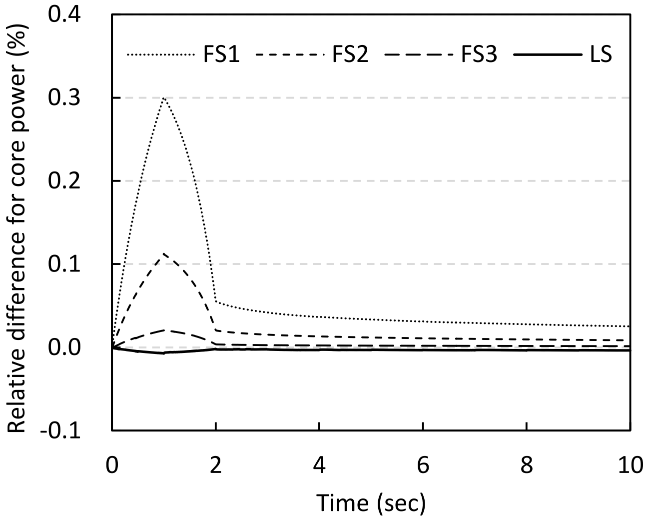

(a) Core power difference

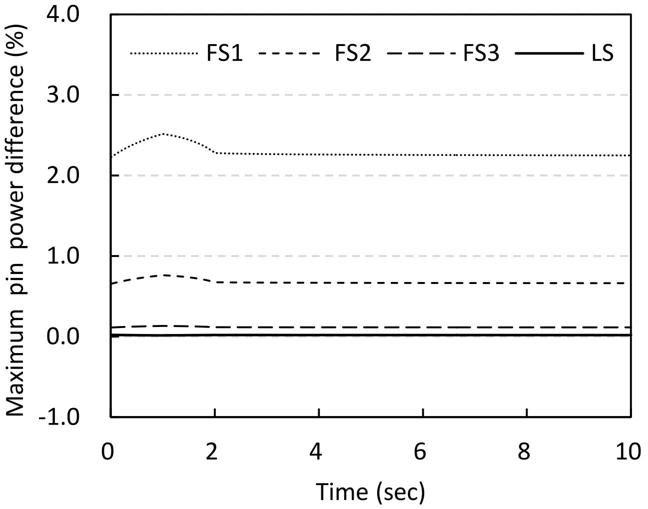

(b) Pin power difference

Figure 2.15 Transition of the core/pin power difference for TD 1-1 (LS vs FS)

As shown in Table 2.11 and Figure 2.15, a large number of flat flux regions are required to reduce the spatial discretization error in the C5G7-TD 2D benchmark problem with the conventional flat source approximation due to the heterogeneity of the calculation geometry. On the other hand, the linear source approximation successfully reduces the spatial discretization error and almost reproduces the reference solution even if the much coarser flux region structure is used in the liner source calculation. It indicates the spatial discretization error is accurately reduced by the linear source approximation and the approximation for the temporal derivatives of the 1st order coefficients of the scalar flux also has a negligible impact on the accuracy of the power transition in the strongly heterogeneous geometry such as the C5G7-TD 2D benchmark problem.

Table 2.12 shows the computation time for the present calculation.

Table 2.12 Comparison of computation time for TD 1-1 (LS vs FS)

Test cases	FS1	FS2	FS3	FS4	LS
Computation time (min)	26	64	165	408	66

The comparison between the test cases, FS4 and LS, shows the improvement from the conventional flat-source-based MAF method to the present scheme, where the speed-up ratio (=FS4/LS) is 6.2 in the present verification. These results suggest the effectiveness of the present scheme, which enables us to fasten time-dependent MOC calculations while achieving the same accuracy.

2.4. Conclusion

In this chapter, a calculation scheme of the MAF method for the time-dependent MOC is derived based on the linear source approximation to improve the efficiency of time-dependent MOC calculations. With the linear source approximation, the 0th-order expansion coefficient of the scalar flux is factorized into the amplitude and shape functions since the 1st-order coefficients represent the local shape of the scalar flux inside the flux region rather than the amplitude. The accuracy and computation time of the present scheme is compared with that of the conventional methods in the TWIGL and C5G7-TD 2D benchmark problems. As a result, it is confirmed that the present scheme can accurately reproduce the spatial and temporal variation of the solution with a shorter computation time. In the present verification, the maximum speedup ratio with respect to the conventional flat-source-based MAF method was 6.2 for the C5G7-TD 2D benchmark problem. In addition, it is also demonstrated that the temporal discretization error is dominated by the coarse mesh diffusion calculation in the MAF method. It indicates that the implementation of the theta method can be employed without the approximation for the residual term at the previous time step. These results show the effectiveness of the present scheme for the time-dependent MOC calculations.

However, issues with computation time remain to apply the time-dependent MOC for real-time applications, *e.g.*, it takes approximately 1 hour even using the present method for 10 seconds transient in the C5G7-TD 2D benchmark problem. In the next chapters, approaches to achieving real-time applications are investigated.

2.5. Reference

[1] Halsall MJ. CACTUS, A characteristics solution to the neutron transport equation in complicated geometries, Winfrith (United Kingdom): UKAEA; 1980, (AEEW-R 1291).

[2] Hursin M, Downar TJ, Kochunas B. Analysis of the core power response during a PWR rod ejection transient using the PARCS nodal code and the DeCART MOC code. Nucl Sci Eng. 2012;170(2):151–167.

[3] Hursin M, Downar TJ, Thomas J. PWR control rod ejection analysis with the method of characteristic code DeCART. Proc PHYSOR 2008; 2008 Sep 14–19; Interlaken, Switzerland.

[4] Ryu M, Joo HG. nTRACER whole core transport solutions to C5G7-TD benchmark. Proc M&C 2017; 2017 Apr 16–20; Jeju, Korea.

[5] Nguyen TN, Jung YS, Downar TJ, Lee C. Implementation of the transient fixed source problem in the neutron transport code PROTEUS-MOC. Ann Nucl Energy. 2019; 129:199–206.

[6] Shen Q, Wang Y, Jabaay D, Kochunas B, Downar TJ. Transient analysis of C5G7-TD benchmark with MPACT. Ann Nucl Energy. 2019;125:107–120.

[7] Dulla S, Mund EH, Ravetto P. Accuracy of a predictor-corrector quasi-static method for space-time reactor dynamics. Proc PHYSOR 2006; 2006 Sep 10–14; Vancouver, Canada.

[8] Ban Y, Endo T, Yamamoto A. A unified approach for numerical calculation of space-dependent kinetic equation. J Nucl Sci Technol. 2012;49:496–515.

[9] Tsujita K, Endo T, Yamamoto A. Application of the multigrid amplitude function method for time-dependent transport equation using MOC. Proc M&C 2013; 2013 May 5–9; Sun Valley, Idaho.

[10] Shaner SC. Transient method of characteristics via the adiabatic, theta and multigrid amplitude function methods. Cambridge (Massachusetts): Massachusetts Institute of Technology; 2014.

[11] Shen Q, Kochunas B, Xu Y, Downar TJ. Transient multilevel scheme with one group CMFD acceleration. Proc PHYSOR 2018; 2018 Apr 22–26; Cancun, Mexico.

[12] Zhang G, Hsieh A, Yang WS, Jung YS. Consistent pCMFD acceleration schemes of the three-dimensional transport code PROTEUS-MOC. Nucl Sci Eng. 2019;193(8):828–853.

[13] Ferrer R, Rhodes J. Linear source approximation in CASMO5. Proc PHYSOR 2012; 2012 Apr 15-20; Knoxville, Tennessee.

[14] Yamamoto A, Giho A, Yuki K, Endo T. GENESIS: a three-dimensional heterogeneous transport solver based on the Legendre polynomial expansion of angular flux method. Nucl Sci Eng. 2017;186:1-22.

[15] Taylor JB. The development of a three-dimensional nuclear reactor kinetics methodology based on the method of characteristics. University Park (Pennsylvania): Pennsylvania State University; 2007.

[16] Boyarinov VF, Fomichenko PA, Hou JJ, Ivanov KN, Aures A, Zwermann W, Velkov K. Deterministic time-dependent neutron transport benchmark without spatial homogenization (C5G7-TD). OECD Nuclear Energy Agency; 2017.

[17] Tsujita K, Endo T, Yamamoto A, Kamiyama Y, Kirimura K. Higher order treatment on temporal derivative of angular flux for time-dependent MOC. Proc M&C 2013; 2013 May 5–9; Sun Valley, Idaho.

[18] Tatsumi M, Yamamoto A. Advanced PWR Core Calculation based on multi-group nodal-transport method in three-dimensional pin-by-pin geometry. J Nucl Sci Technol. 2003;40:376–387.

[19] Hageman LA, Yasinsky JB. Comparison of alternating direction time differencing methods with other implicit methods for the solution of the neutron group diffusion equations. Nucl Sci Eng. 1969;38:8–32.

[20] Yamamoto A, Tabuchi M, Sugimura N, Ushio T, Mori M. Derivation of optimum polar angle quadrature set for the method of characteristics based on approximation error for the Bickley function. J Nucl Sci Technol. 2007;44:129–136.

[21] Stacey WM, Nuclear Reactor Physics. New York: John Wiley & Sons; 2001.

[22] Endo T, Tatsumi M. Study on kinetic transport solvers for pin-by-pin core calculation. Proc PHYSOR 2008; 2008 Sep 14–19; Interlaken, Switzerland.

[23] OECD Nuclear Energy Agency. Benchmark on deterministic transport calculations without spatial homogenization. OECD Publications; 2003.

3. Fast reproduction of time-dependent diffusion calculations using the ROM based on the POD

3.1. Introduction

As discussed in Chapter 2, the MAF method derived based on the linear source approximation successfully reduces the computation time of time-dependent MOC calculations [1]. However, it is still difficult to apply such simulations for real-time applications due to their heavy computational load, *e.g.*, it takes approximately 1 hour even using the MAF method and the linear source approximation for 10 seconds transient in the C5G7-TD 2D benchmark problem. Such a heavy computational load comes from an enormous number of variables along neutron flight paths. Thus, efficient numerical methods, which reproduce the calculation results of detailed FOMs with fewer computational costs and achieve real-time applications, are desirable. The dimensionality reduction techniques can address this issue and are successfully applied to improve computational efficiency with less degradation of accuracy [2–10]. Especially, the POD [9] is known as an efficient technique to reduce the DOF of the original problem and it is also applied to the steady-state S_N transport calculations in past studies [10].

In the POD approach, flux distribution is expanded by an orthogonal basis, which is obtained by the SVD and the low-rank approximation (LRA) for the flux vectors sampled from the calculation results of a FOM. The SVD enables us to represent the original flux distributions with fewer DOFs than the conventional eigenfunctions when the flux distributions in the solution space of the target problem are appropriately considered. However, to apply the POD for kinetic calculations, various flux distributions can be considered to construct an orthogonal basis, *e.g.*, utilization of flux distributions calculated with steady-state eigenvalue calculations or those at specific time steps during kinetic calculations. It is explained as the construction of the orthogonal bases using the flux distribution in λ or the natural modes [11], respectively.

Therefore, in this chapter, an efficient way to construct the proper orthogonal basis for kinetic calculations is investigated. In the present study, several orthogonal bases are constructed by applying the SVD and LRA to various spatial distributions of scalar flux obtained by steady-state or kinetic calculations. The accuracy and computation time of the POD calculations using the orthogonal bases are compared through numerical benchmark calculations. It should be noted that the diffusion calculation with the conventional finite-difference discretization is considered as the FOM in this chapter to show the proof of the principle, and the application of the POD for time-dependent MOC calculations is investigated in Chapter 4.

The remaining part of this chapter is organized as follows. The theoretical basis of the present ROM using the POD, SVD, and LRA is described in Section 3.2. The numerical results and discussions are shown in Section 3.3. Finally, concluding remarks are summarized in Section 3.4.

3.2. Methodology

In the present study, flux distribution is expanded with an orthogonal basis on space. The orthogonal basis is not an analytic function. It is numerically obtained in the spatially discretized form. Then, the discretized neutron diffusion equation is transformed into the equation of expansion coefficients for the basis. To construct an orthogonal basis that well captures the characteristics of the result of the FOM with fewer DOFs, the SVD and LRA are applied for the spatially discretized scalar flux vectors taken from various FOM calculations.

In this section, the theoretical basis of the dimensionality reduction using the POD for steady-state and kinetic calculations is described in Subsections 3.2.1 and 3.2.2, respectively. The construction of the orthogonal basis, which is the key point in the present study, is provided in Subsection 3.2.3.

3.2.1. Application of the POD to steady-state eigenvalue calculations

The diffusion equation can be numerically solved through discretization in energy and space. The discretized form for a steady-state eigenvalue calculation is written as:

$$\mathbf{A}_{\boldsymbol{g}}\vec{\phi}_g = \frac{\chi_g}{k_{\text{eff}}}\sum_{g'}^{G}\mathbf{F}_{\boldsymbol{g'}}\vec{\phi}_{g'} + \sum_{g'}^{G}\mathbf{S}_{\boldsymbol{g'\to g}}\vec{\phi}_{g'}\ , \tag{3.1}$$

where g is the subscript for the energy group; the other operators and the coefficients are as follows:

$\vec{\phi}_g$: column vector representing the spatial distribution of g-th neutron flux,

$\mathbf{A}_{\boldsymbol{g}}$: annihilation matrix,

$\mathbf{F}_{\boldsymbol{g}}$: fission matrix,

$\mathbf{S}_{\boldsymbol{g'\to g}}$: scattering matrix,

k_{eff} : λ-mode eigenvalue,

χ_g : fission spectrum.

Note that number of elements in the column vector $\vec{\phi}_g$ corresponds to the total number of spatial meshes in the calculation geometry, which is generally large in detail reactor core simulations.

Now the column flux vector is expanded by orthogonal bases as:

$$\vec{\phi}_g = \sum_{i}^{k} \vec{u}_i \varphi_{g,i} , \tag{3.2}$$

$$\vec{u}_i^T \vec{u}_j = \delta_{ij}, \tag{3.3}$$

where $\vec{u}_i$ and $\varphi_{g,i}$ are the i-th orthogonal basis and the expansion coefficient, respectively. k is the number of orthogonal bases used for expansion. Equation (3.2) can be written in a matrix form as:

$$\vec{\phi}_g = \mathbf{U}\vec{\varphi}_g , \tag{3.4}$$

where

$$\mathbf{U} = [\vec{u}_1 \quad \dots \quad \vec{u}_k] , \tag{3.5}$$

$$\vec{\varphi}_g = [\varphi_{g,1} \quad \cdots \quad \varphi_{g,k}]^T . \tag{3.6}$$

Substituting Equation (3.4) into Equation (3.1) and multiplying $\mathbf{U}^T$ for both sides, we can obtain the equation for the expansion coefficients, $\vec{\varphi}_g$, as follows [10]:

$$\hat{\mathbf{A}}_{\boldsymbol{g}} \vec{\varphi}_g = \frac{\chi_g}{k_{\text{eff}}} \sum_{g'}^{G} \hat{\mathbf{F}}_{\boldsymbol{g'}} \vec{\varphi}_{g'} + \sum_{g'}^{G} \hat{\mathbf{S}}_{\boldsymbol{g'\to g}} \vec{\varphi}_{g'} , \tag{3.7}$$

$$\hat{\mathbf{A}}_{\boldsymbol{g}} = \mathbf{U}^T \mathbf{A}_{\boldsymbol{g}} \mathbf{U} , \tag{3.8}$$

$$\hat{\mathbf{F}}_{\boldsymbol{g}} = \mathbf{U}^T \mathbf{F}_{\boldsymbol{g}} \mathbf{U} , \tag{3.9}$$

$$\hat{\mathbf{S}}_{\boldsymbol{g'\to g}} = \mathbf{U}^T \mathbf{S}_{\boldsymbol{g'\to g}} \mathbf{U} , \tag{3.10}$$

Note that number of elements in $\vec{\varphi}_g$ is k and the size of matrices ($\hat{\mathbf{A}}_{\boldsymbol{g}}$, $\hat{\mathbf{F}}_{\boldsymbol{g}}$, $\hat{\mathbf{S}}_{\boldsymbol{g'\to g}}$) is $k \times k$. When the number of expansion coefficients (k) is much smaller than that of meshes (N), Equation (3.7) can be solved with much less computational cost than the original Equation (3.1). For example, when the flux distribution for 100 meshes (N=100) can be represented by 10 orthogonal bases (k=10), the size of each matrix becomes as follows:

$\mathbf{A}_{\boldsymbol{g}}, \mathbf{F}_{\boldsymbol{g}}, \mathbf{S}_{\boldsymbol{g'\to g}}$	:	100×100,
$\vec{\phi}_g$	:	100×1,
$\mathbf{U}$	:	100×10,
$\vec{\varphi}_g$	:	10×1,
$\hat{\mathbf{A}}_{\boldsymbol{g}}, \hat{\mathbf{F}}_{\boldsymbol{g}}, \hat{\mathbf{S}}_{\boldsymbol{g'\to g}}$	:	10×10.

Since the complexity of the algorithm to solve Equations (3.1) and (3.7) is generally $O(n^2)$–$O(n^3)$, *i.e.*, the second to third power of total number (n) of spatial meshes or expansion coefficients, this dimensionality reduction reduces the computational cost in the present calculation condition.

3.2.2. Application of the POD to kinetic calculations

In this subsection, the kinetic equations using the POD are derived. Equations (3.11) and (3.12) are time-dependent diffusion equations.

$$\frac{1}{v_g}\frac{d}{dt}\vec{\Phi}_g = -\mathbf{A}_g\vec{\Phi}_g + (1-\beta)\chi_g^p\sum_{g'}^{G}\mathbf{F}_{g'}\vec{\Phi}_{g'} + \sum_{g'}^{G}\mathbf{S}_{g'\to g}\vec{\Phi}_{g'} + \sum_{m}^{M}\lambda_m\chi_{m,g}^d\vec{C}_m\,, \tag{3.11}$$

$$\frac{d}{dt}\vec{C}_m = \beta_m\sum_{g'}^{G}\mathbf{F}_{g'}\vec{\Phi}_{g'} - \lambda_m\vec{C}_m\,, \tag{3.12}$$

where

v_g : neutron velocity,

λ_m : decay constant,

β_m : delayed neutron fraction ($\beta = \sum_m^M \beta_m$),

$\vec{C}_m$: column vector for precursor density,

χ_g^p : prompt fission spectrum,

$\chi_{m,g}^d$: delayed fission spectrum,

m : subscripts for the precursor family.

Note that the number of elements of $\vec{C}_m$ is the total number of meshes. In kinetic calculations, delayed neutron precursors should be considered in addition to scalar flux. Regarding the treatment of delayed neutron precursors, the following options can be considered:

(1) Expand column vector $\vec{C}_m$ with the same orthogonal basis for scalar flux spatial distributions

(2) Expand column vector $\vec{C}_m$ with the orthogonal basis for the precursor density distributions

(3) Temporally integrate the precursor density in each mesh using the reconstructed flux distribution (no expansion for precursor density)

The first option is the simplest but the expansion error for the precursor density distribution will be included for the temporal integration of the precursor expansion coefficients. With the second option, an orthogonal basis is explicitly calculated for precursors as well as scalar flux. However, a transformation of the orthogonal bases between precursors and scalar flux is necessary since these have different orthogonal bases. The third option is accurate, but it increases the DOFs of the precursor density calculation and will increase the computational load. In the present study, the first option is employed. The validity of the present approach will be discussed with numerical results.

Discretizing Equation (3.11) using the fully implicit method, the following equations are obtained [11]:

$$\left(\mathbf{A}_{\boldsymbol{g}}^{\boldsymbol{n+1}} + \frac{1}{v_g \Delta t}\mathbf{I}\right)\vec{\phi}_g^{n+1} = \vec{Q}_g^{n+1} + \vec{S}_g^{n} , \tag{3.13}$$

$$\vec{Q}_g^{n+1} = \gamma_g \sum_{g'}^{G} \mathbf{F}_{\boldsymbol{g'}}^{\boldsymbol{n+1}} \vec{\phi}_{g'}^{n+1} + \sum_{g'}^{G} \mathbf{S}_{\boldsymbol{g'\to g}}^{\boldsymbol{n+1}} \vec{\phi}_{g'}^{n+1} , \tag{3.14}$$

$$\gamma_g = (1-\beta)\chi_g^p + \sum_{m}^{M} \lambda_m \xi_m \chi_{m,g}^d , \tag{3.15}$$

$$\vec{S}_g^n = \frac{\vec{\phi}_g^n}{v_g \Delta t} + \sum_{m}^{M} \lambda_m \chi_{m,g}^d \left(\mu_m \vec{C}_m^n + \eta_m \sum_{g'}^{G} \mathbf{F}_{\boldsymbol{g'}}^{\boldsymbol{n}} \vec{\phi}_{g'}^n\right), \tag{3.16}$$

where n is the superscript for the time step and $\mathbf{I}$ is an identity matrix. μ_m, η_m and ξ_m are the coefficients for the temporal integration of precursors, which are calculated using the analytical solution of Equation (3.12) assuming the linear variation of the fission source between the successive time steps as [11]:

$$\vec{C}_m^{n+1} = \mu_m \vec{C}_m^n + \eta_m \sum_{g'}^{G} \mathbf{F}_{\boldsymbol{g'}}^{\boldsymbol{n}} \vec{\phi}_{g'}^n + \xi_m \sum_{g'}^{G} \mathbf{F}_{\boldsymbol{g'}}^{\boldsymbol{n+1}} \vec{\phi}_{g'}^{n+1} , \tag{3.17}$$

$$\mu_m = \exp(-\lambda_m \Delta t) , \tag{3.18}$$

$$\eta_m = \frac{\beta_m}{\lambda_m}\left(\frac{1-\mu_m}{\lambda_m \Delta t} - \mu_m\right), \tag{3.19}$$

$$\xi_m = \frac{\beta_m}{\lambda_m}\left(1 - \frac{1-\mu_m}{\lambda_m \Delta t}\right). \tag{3.20}$$

Substituting Equation (3.4) into Equation (3.13) and multiplying $\mathbf{U}^T$ for both sides, we can obtain the equation for the expansion coefficients as follows:

$$\left(\widehat{\mathbf{A}}_{\boldsymbol{g}}^{\boldsymbol{n+1}} + \frac{1}{v_g \Delta t}\mathbf{I}\right)\vec{\varphi}_g^{n+1} = \vec{\mathcal{Q}}_g^{n+1} + \vec{\mathcal{S}}_g^{n} , \tag{3.21}$$

$$\vec{\mathcal{Q}}_g^{n+1} = \gamma_g \sum_{g'}^{G} \hat{\mathbf{F}}_{\boldsymbol{g'}}^{\boldsymbol{n+1}} \vec{\varphi}_{g'}^{n+1} + \sum_{g'}^{G} \hat{\mathbf{S}}_{\boldsymbol{g'\to g}}^{\boldsymbol{n+1}} \vec{\varphi}_{g'}^{n+1} , \tag{3.22}$$

$$\vec{s}_g^{\,n} = \frac{\vec{\varphi}_g^{\,n}}{v_g \Delta t} + \sum_{m}^{M} \lambda_m \chi_{m,g}^{d} \left(\mu_m \vec{\varsigma}_m^{\,n} + \eta_m \sum_{g'}^{G} \hat{\mathbf{F}}_{\boldsymbol{g'}}^{\boldsymbol{n}} \vec{\varphi}_{g'}^{\,n} \right) , \tag{3.23}$$

$$\vec{\varsigma}_m^{\,n+1} = \mu_m \vec{\varsigma}_m^{\,n} + \eta_m \sum_{g'}^{G} \hat{\mathbf{F}}_{\boldsymbol{g'}}^{\boldsymbol{n}} \vec{\varphi}_{g'}^{\,n} + \xi_m \sum_{g'}^{G} \hat{\mathbf{F}}_{\boldsymbol{g'}}^{\boldsymbol{n+1}} \vec{\varphi}_{g'}^{\,n+1} , \tag{3.24}$$

where $\mathbf{U}^T\mathbf{U} = \mathbf{I}$ is used and the precursor density is also expanded using the orthogonal basis:

$$\vec{C}_m = \mathbf{U}\vec{\varsigma}_m , \tag{3.25}$$

where $\vec{\varsigma}_m$ is the expansion coefficient for the m-th precursor densities. Note that the precursor densities are expanded by the same orthogonal basis for the scalar flux in the present study. The accuracy of this assumption is discussed in Subsection 3.3.2.

3.2.3. Orthogonal basis construction

In the POD, an orthogonal basis, which well represents the flux distribution in the target problem with fewer DOFs, is desirable from the viewpoint of computational efficiency. To find such a basis, eigenfunctions or flux distributions with general perturbations are often employed in past studies [3–5]. They are applicable for general perturbations but higher order is necessary to represent the complicated flux distributions. Thus, the orthogonal basis is numerically constructed using the flux distributions that appeared in the calculation results of the FOM. To extract the orthogonal basis that well captures the characteristics of the flux distributions obtained by the FOM, the SVD and LRA are used. It enables us to make an efficient and appropriate orthogonal basis for the target problem with fewer DOFs.

The next issue is the choice of flux distributions that represent the characteristics of the target problem. In the present study, the following two options are tested.

(1) Sampling from the steady-state eigenvalue calculation results of the FOM

(2) Sampling from the kinetic calculation results of the FOM

In the first option, the flux distributions are chosen from the eigenvalue calculation results of the FOM. Various cross section sets, which cover the perturbation of the target problem, are used for the eigenvalue calculations. The sampled flux distributions are described in a matrix form:

$$\mathbf{M_E} = (\mathbf{M_{E,1}} \quad \cdots \quad \mathbf{M}_{\mathbf{E},\boldsymbol{g}} \quad \cdots \quad \mathbf{M_{E,G}}) , \tag{3.26}$$

$$\mathbf{M}_{\mathbf{E},g} \equiv \begin{pmatrix} \phi_{g,1}^{XS1} & \cdots & \phi_{g,1}^{XSn} \\ \vdots & & \vdots \\ \phi_{g,j}^{XS1} & \cdots & \phi_{g,j}^{XSn} \\ \vdots & & \vdots \\ \phi_{g,N}^{XS1} & \cdots & \phi_{g,N}^{XSn} \end{pmatrix}, \tag{3.27}$$

where $\phi_{g,j}^{XSn}$ denotes the flux at the energy group g, the mesh j, and the calculation case using the cross section set XSn. In Equation (3.27), the amplitude of the flux distributions for all calculation cases is normalized so that the core power becomes 1.0. Applying the SVD, the orthogonal basis for the target problem is calculated as the left singular vectors $\mathbf{U}_\mathbf{E}$ of the matrix $\mathbf{M}_\mathbf{E}$, as:

$$\mathbf{M}_\mathbf{E} = \mathbf{U}_\mathbf{E}\mathbf{\Sigma}_\mathbf{E}\mathbf{V}_\mathbf{E}^T , \tag{3.28}$$

where $\mathbf{U}_\mathbf{E}$, $\mathbf{\Sigma}_\mathbf{E}$, and $\mathbf{V}_\mathbf{E}$ denote the left singular vectors, the singular values, and the right singular vectors, respectively. The present orthogonal basis can be used both for steady-state and kinetic calculations. However, it is obtained based on the eigenvalue calculations and it covers the relative spatial distribution of the fundamental λ-mode [11] of the scalar flux with various cross section sets. Thus, it might cause the degradation of the accuracy because major components of higher-order natural mode [11] flux distributions excited in kinetic calculations are not accurately represented with the present orthogonal basis. The applicability and accuracy of this orthogonal basis are confirmed in Subsection 3.3.2.

In the second option, the flux distribution is chosen from the kinetic calculation results of the FOM. If the temporal variation of scalar flux in the target problem is available, the sampled flux distributions are described as:

$$\mathbf{M}_\mathbf{K} = (\mathbf{M}_{\mathbf{K},\mathbf{1}} \quad \cdots \quad \mathbf{M}_{\mathbf{K},g} \quad \cdots \quad \mathbf{M}_{\mathbf{K},\mathbf{G}}) , \tag{3.29}$$

$$\mathbf{M}_{\mathbf{K},g} \equiv \begin{pmatrix} \phi_{g,1}^{1} & \cdots & \phi_{g,1}^{TSn} \\ \vdots & & \vdots \\ \phi_{g,j}^{1} & \cdots & \phi_{g,j}^{TSn} \\ \vdots & & \vdots \\ \phi_{g,N}^{1} & \cdots & \phi_{g,N}^{TSn} \end{pmatrix}, \tag{3.30}$$

where $\phi_{g,j}^{TSn}$ denotes the flux at energy group g, mesh j, and the time step TSn. In Equation (3.29), the amplitude of the flux distribution at each time step is also normalized so that the core power at each time step becomes 1.0 to avoid the overfitting of the orthogonal basis where the amplitude of the scalar flux is large. The amplitude of the flux distributions is covered by the expansion coefficients. By applying the SVD to the matrix $\mathbf{M}_\mathbf{K}$, the orthogonal basis based on the kinetic calculation is obtained as:

$$\mathbf{M_K} = \mathbf{U_K \Sigma_K V_K^{\mathit{T}}} \,. \tag{3.31}$$

This option would provide a more accurate solution for the target problem because the higher-order natural mode flux distributions during the transient can be taken into account on an orthogonal basis. Moreover, the fine time step calculation with the FOM is not necessarily required for the construction of the orthogonal basis because the flux amplitude is normalized in each time step and only the relative spatial distributions of the scalar flux are important. Thus, there is an option to employ a coarse time step calculation to provide data for the construction of the orthogonal basis as well as the past study [12], which employs coarse burnup calculation for the construction of the orthogonal basis. This approach has an advantage from the viewpoint of the data preparation time to construct an orthogonal basis.

3.3. Numerical results

In the present study, the TWIGL benchmark problem [13], which is widely used 2D test problem for the verification of the kinetic calculation code, is used to verify the accuracy and performance of the ROM. Figure 3.1 and Table 3.1 show the calculation geometry and cross sections.

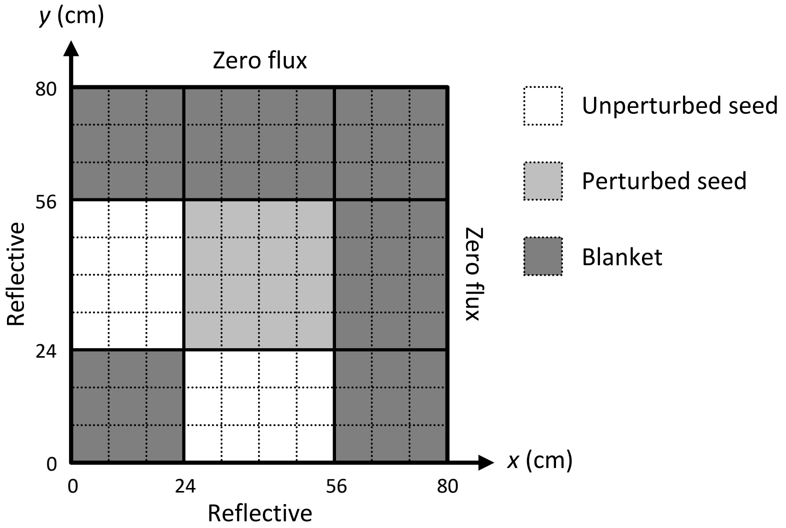

Figure 3.1 Top view for the TWIGL benchmark problem for diffusion calculations

Table 3.1 Material properties of the TWIGL benchmark problem for diffusion calculations

Material	Energy group	D_g (cm)	$\Sigma_{a,g}$ (1/cm)	$\nu\Sigma_{f,g}$ (1/cm)	χ_g (1/cm)	$\Sigma_{s,1\to2}$ (1/cm)
Unperturbed seed	1	1.4	0.010	0.007	1.0	0.01
	2	0.4	0.150	0.200	0.0	
Perturbed Seed	1	1.4	0.010	0.007	1.0	0.01
	2	0.4	0.150	0.200	0.0	
Blanket	1	1.3	0.008	0.003	1.0	0.01
	2	0.5	0.050	0.060	0.0	
	ν	v_1(cm/sec)	v_2(cm/sec)	β (-)	λ (1/sec)	
	2.43	10^7	2×10^5	0.0075	0.08	

The unperturbed and perturbed seed regions have the same cross section at the initial steady state. The perturbation conditions specified in the original benchmark problem, *i.e.*, the step and ramp perturbations shown in Equations (3.32) and (3.33), are used in the present verification.

$$\text{Step perturbation} \quad : \quad \Sigma_{a,2}^{PS}(t) = \Sigma_{a,2}^{PS}(0) - 0.0035\ (t > 0)\,, \tag{3.32}$$

$$\text{Ramp perturbation} \quad : \quad \Sigma_{a,2}^{PS}(t) = \begin{cases} \Sigma_{a,2}^{PS}(0)(1 - 0.116667t) & (t \le 0.2) \\ 0.976666\Sigma_{a,2}(0) & (t > 0.2) \end{cases}, \tag{3.33}$$

where $\Sigma_{a,2}^{PS}$ denotes the 2nd energy group absorption cross section of the perturbed seed region.

3.3.1. Verification for steady-state calculations

In the present verification, the accuracy of the ROM is verified for steady-state eigenvalue calculations. Since the cross section at the perturbed seed region is varied in the TWIGL benchmark problem, the eigenvalue calculations are also carried out by changing the cross section in the perturbed seed region. Table 3.2 shows the calculation condition of the FOM, which is the conventional diffusion calculation using the finite difference method. An in-house diffusion calculation code is used throughout the present study. The validity of the in-house diffusion code has been confirmed through the comparison with other calculation codes.

Table 3.2 Steady state calculation condition of the TWIGL benchmark problem for FOM

Parameters	Calculation condition
Mesh structure	1 cm × 1 cm square mesh (totally 6400 meshes)
Convergence criterion	Fission : 10^{-8}, flux : 10^{-8}
Spatial discretization	Finite difference method

Assuming the cross sections specified in the TWIGL benchmark problem as the base condition, the eigenvalue calculations are carried out assuming ± 30% perturbation for 2nd energy group absorption and production cross sections, respectively. Although ± 30% perturbation is quite larger than that of the original benchmark specification (-2.33% perturbation only for absorption cross section), it is selected to see the capability and limitation of the present ROM. Figure 3.2 shows the eigenvalue calculated with the FOM for various cross sections. These results are used as the reference solutions in the present verification.

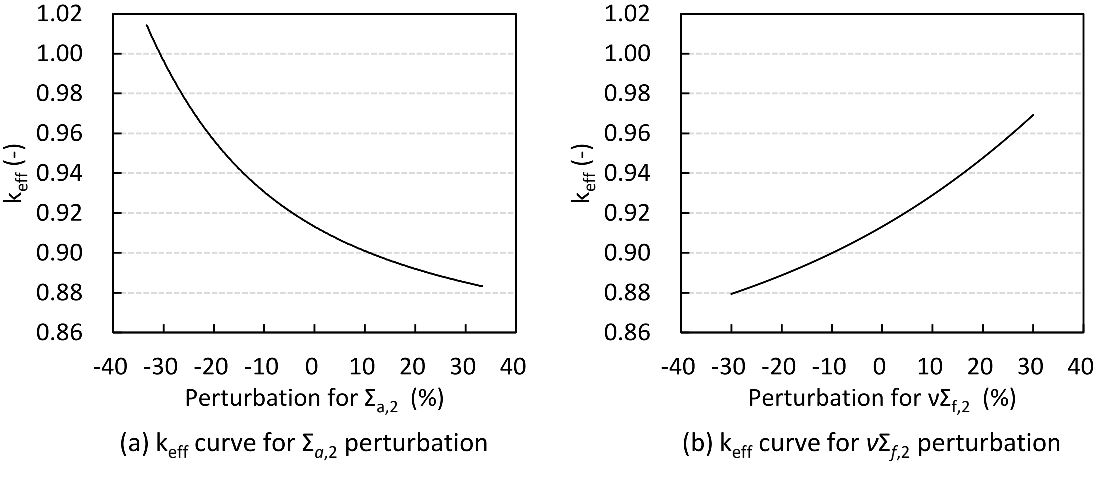

(a) k_{eff} curve for $\Sigma_{a,2}$ perturbation (b) k_{eff} curve for $\nu\Sigma_{f,2}$ perturbation

Figure 3.2 Reference eigenvalue obtained by FOM for various cross sections

The flux distribution matrix $\mathbf{M_E}$ is constructed using the following 11 flux spatial distributions:

- Flux distribution of the base condition
- Flux distributions calculated with ± 1.3%, ± 2.7%, ± 4.0%, ± 5.3%, ± 6.7% perturbation for 2nd energy group absorption cross section

The size of the matrix $\mathbf{M_E}$ becomes 6400×22 in the present calculation condition. The number of rows corresponds to the total number of spatial meshes (80×80=6400). That of columns is the total number of the cross section sets times that of energy groups (11×2=22) as shown in Equations (3.26) and (3.27). The above perturbation to construct the orthogonal basis is narrower than that for reference calculations (± 30%). In principle, the perturbation range used to construct an orthogonal basis should cover the perturbations in target problems. However, in the present study, the narrower perturbation range is intentionally chosen to confirm the capability of the present ROM.

Figure 3.3 shows the singular values of the flux distribution matrix $\mathbf{M_E}$.

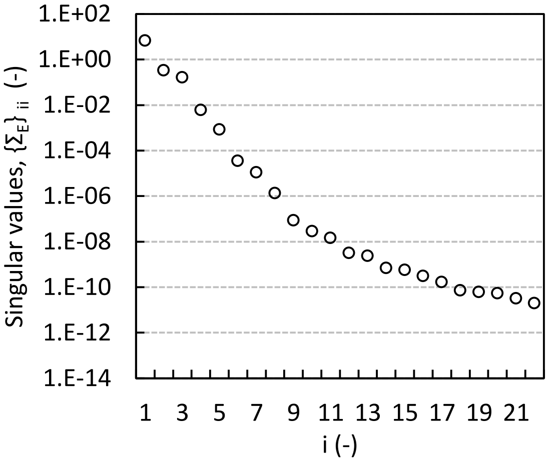

Figure 3.3 Singular values of the matrix, $\mathbf{M_E}$

Figure 3.3 indicates that the singular values are rapidly decreasing as the number of singular values increases, suggesting the flux distribution matrix can be accurately represented by a small number of singular values. Thus, the LRA is applied and the dimensions whose singular value is less than the threshold are truncated [14]. Table 3.3 shows the case matrix.

Table 3.3 Case matrix for the steady state calculation

Test case	Truncation threshold	Size of orthogonal basis ($\mathbf{U}_{\mathbf{E}}$)*	Size of coefficient matrices ($\widehat{\mathbf{A}}_g, \widehat{\mathbf{F}}_g, \widehat{\mathbf{S}}_{g'\to g}$)
BE-4	10^{-3}	6400×4	4×4
BE-7	10^{-5}	6400×7	7×7
BE-11	10^{-8}	6400×11	11×11

* The dimensions whose singular value is less than the truncation threshold.

As shown in Table 3.3, there are 3 test cases, *i.e.*, BE-4, BE-7, and BE-11, where the number after the case name, “BE (Basis calculated from Eigenvalue calculations)”, denotes the rank of the compressed coefficient matrices. For all test cases, the order of the coefficient matrices is successfully reduced rather than that of the original diffusion equation.

Using the compressed coefficient matrices, eigenvalue calculations are carried out. Figure 3.4 shows the relative difference of the eigenvalue and power distribution between each test case and the FOM, where the power distribution is calculated as the product of mesh-wise fission cross section, volume, and reconstructed mesh-wise flux as:

$$\left(P_j\right)_{j=1\ldots N} = \sum_{g'}^{G} \left(\Sigma_{f,g',j} V_j\right)_{j=1\ldots N} \mathbf{U}_{\mathbf{E}} \vec{\varphi}_{g'} \,, \tag{3.34}$$

where P_j and V_j denote the fission power and volume of the mesh j. The maximum relative difference for the reconstructed power distribution is calculated as:

$$\text{Maximum relative difference (\%)} \quad = \max \left| \frac{P_j - P_j^{FOM}}{P_j^{FOM}} \right| \times 100 \,, \tag{3.35}$$

where FOM is the superscript for the reference FOM solution.

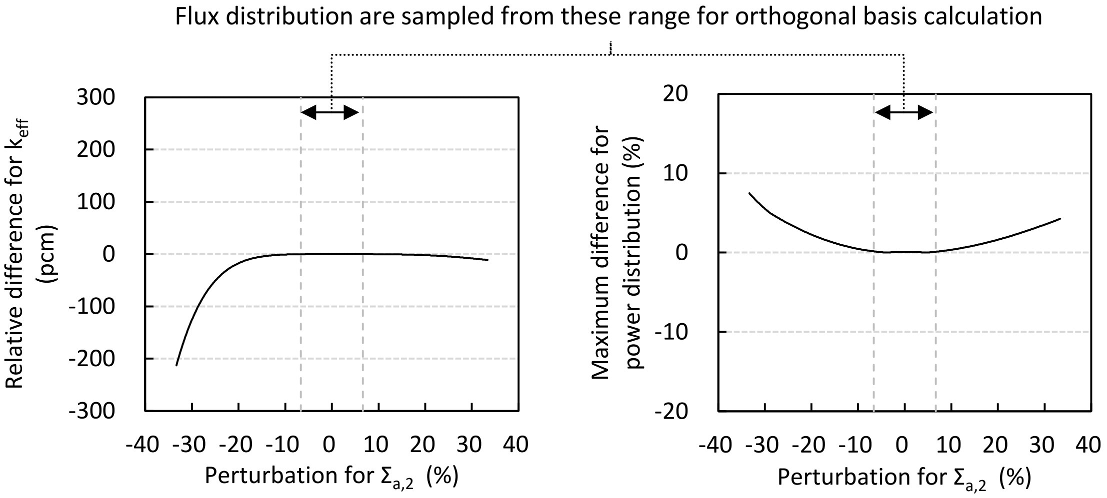

(a) BE-4 k_{eff} difference

(b) BE-4 power distribution difference

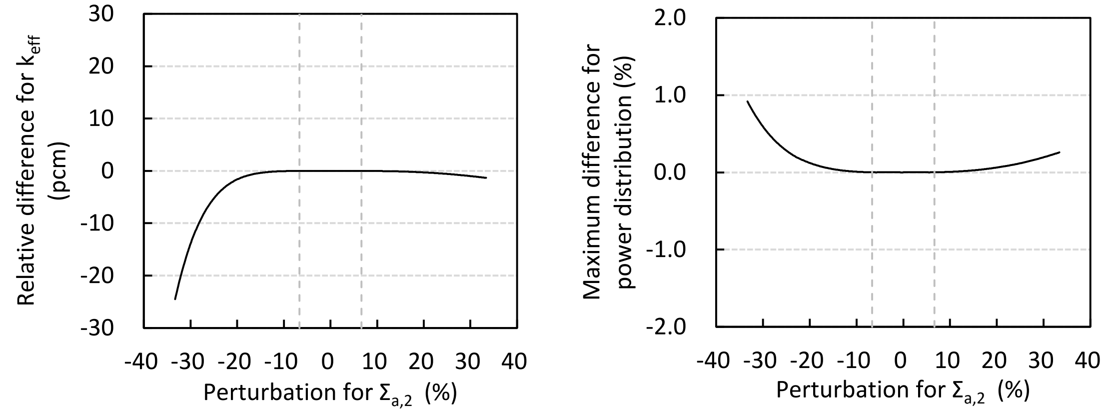

(c) BE-7 k_{eff} difference

(d) BE-7 power distribution difference

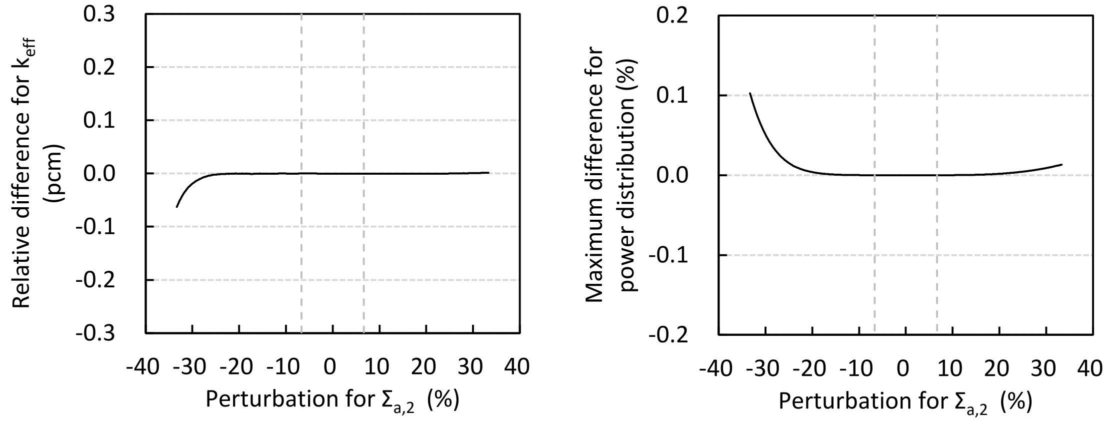

(e) BE-11 k_{eff} difference

(f) BE-11 power distribution difference

Figure 3.4 Relative difference of eigenvalue and power distribution for $\Sigma_{a,2}$ perturbation

As shown in Figure 3.4, the test case BE-11 successfully reproduces the reference FOM calculation solution with high accuracy even if the perturbation is larger than that used in the construction of the orthogonal basis. The maximum relative difference of the eigenvalue and the power distribution between the test case BE-11 and the FOM is 0.1 pcm and 0.1 %, respectively. Although the accuracy of the test cases, BE-4 and BE-7, is degraded, they still almost reproduce the FOM solution within the range in which the flux distributions are chosen to construct the orthogonal basis. The degradation of the accuracy outside of ±6.7% perturbation range is due to a reduction of the representativeness of the orthogonal basis, *i.e.*, the expansion error with orthogonal basis becomes larger since the orthogonal basis is constructed from the flux distributions calculated within ±6.7% perturbation range.

However, as for the perturbation for the production cross section, BE-11 does not reproduce the FOM solution as shown in Figure 3.5 because the present orthogonal basis is calculated to cover the solution space only for the absorption cross section perturbation. Since the 0% perturbation condition for the production cross section (the base condition) is included in the solution space covered by the present orthogonal basis, the difference between the ROM and the FOM becomes larger for the perturbation of the production cross section.

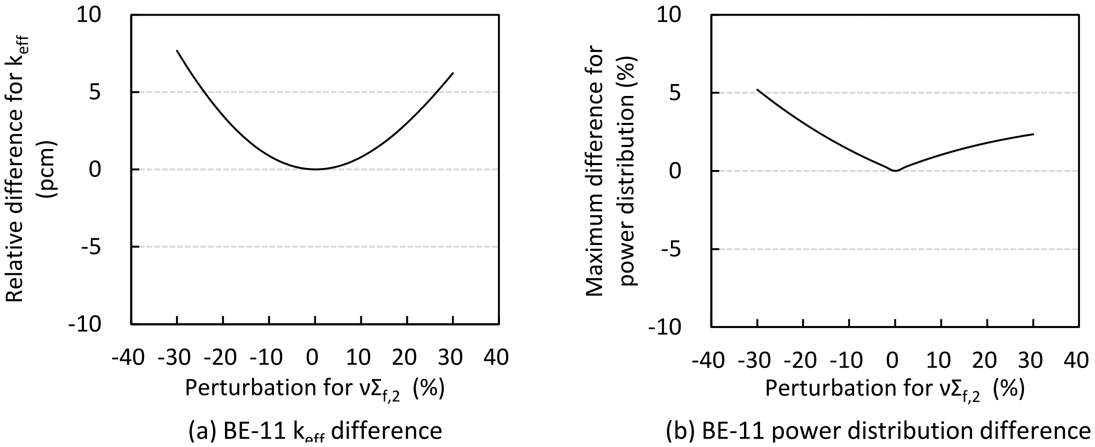

Figure 3.5 Relative difference of eigenvalue and power distribution for $\nu\Sigma_{f,2}$ perturbation

3.3.2. Verification for kinetic calculations

The accuracy of the ROM for the kinetic calculations is verified using the TWIGL benchmark problem. Table 3.4 shows the calculation condition of the FOM, which is the conventional diffusion calculation using the finite difference and the fully implicit methods. As for the precursor density calculations, the analytical solution assuming the linear variation of the fission source between the successive time steps is employed.

Table 3.4 Kinetic calculation condition of the TWIGL benchmark problem for FOM

Parameters	Calculation condition
Mesh structure	1 cm × 1 cm square mesh (6400 meshes)
Convergence criterion	Fission : 10^{-8}, flux : 10^{-8}
Spatial discretization	Finite difference method
Temporal discretization	Fully implicit method for flux, analytical solution for precursor*
Time step size	1 msec for reference solution, 40 msec for orthogonal basis calculation

* Linear transition for the fission source is assumed. [11]

As shown in Table 3.4, the kinetic calculation with coarse time step size, Δt = 40 msec, is also carried out for the orthogonal basis calculation. Since the TWIGL benchmark problem is for 0.4 sec kinetic calculation, 11 time steps flux distributions can be obtained, where it is fine enough to cover the solution space of the TWIGL benchmark problem. The reference FOM solution is calculated with a fine time step size, Δt = 1 msec.

Figure 3.6 shows the reference FOM solution for each perturbation.

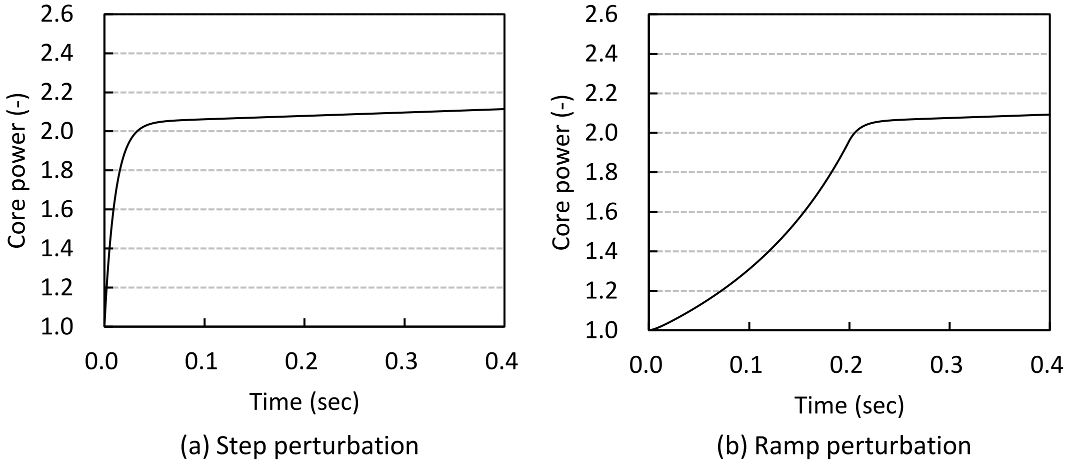

(a) Step perturbation

(b) Ramp perturbation

Figure 3.6 Reference FOM solution of the TWIGL benchmark problem ($\Delta t =$ 1 msec)

The following two orthogonal bases are considered for the ROM calculations:

(1) Utilize the orthogonal basis, $\mathbf{U_E}$, obtained by steady-state calculations in Subsection 3.3.1.

(2) Calculate the orthogonal basis, $\mathbf{U_K}$, using the flux distributions sampled from the coarse time step FOM kinetic solution.

As for the former option, -2.33% perturbation for the 2nd energy group absorption cross section at the perturbed seed is considered in the eigenvalue calculation. This perturbation appears in the step and ramp perturbation conditions in the kinetic calculation of the TWIGL benchmark problem. Thus, the orthogonal basis $\mathbf{U_E}$ can cover the solution space of these transients. For the latter option, 11 flux distributions from t = 0.0 sec to t = 0.4 sec with 40 msec intervals are sampled from the coarse time step FOM solution for the ramp perturbation condition to calculate the orthogonal basis. There are two reasons to choose the ramp perturbation to construct an orthogonal basis. Firstly, the inserted reactivity is the same in both perturbation conditions in the TWIGL benchmark problem and the calculation results of the ramp perturbation have a more gradual variation for the flux distribution than that of the step perturbation. Secondly, to see the applicability of the orthogonal basis that is constructed with different transient conditions. If the accuracy of the ROM is comparable to the step and ramp perturbation conditions, we can guess that a dedicated orthogonal basis would not be necessary for various transients when the perturbation and inserted reactivity are comparable.

Figure 3.7 shows the accuracy of the coarse time step FOM solution for the ramp perturbation condition, where the root mean square (RMS) difference for the flux distribution is calculated as:

$$\text{RMS difference (\%)} \quad = \sqrt{\frac{1}{N}\sum_{j}^{N}\left(\frac{\phi_{g,j}-\phi_{g,j}^{ref}}{\phi_{g,j}^{ref}}\right)^{2}} \times 100 \ , \tag{3.36}$$

where $\phi_{g,j}$ denotes the scalar flux at energy group g and mesh j. The superscript ref denotes the reference FOM solution calculated with Δt = 1 msec. The accuracy of the relative flux distributions normalized the core power of each time step as 1.0 is also shown in Figure 3.7.

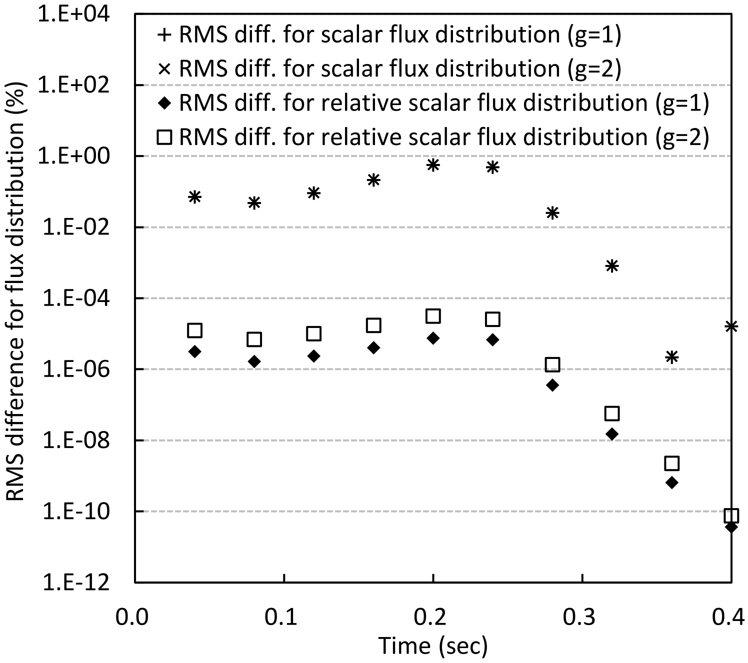

Figure 3.7 Accuracy of the coarse time step calculation for ramp perturbation condition with FOM

As shown in Figure 3.7, the large temporal discretization error remains for the scalar flux distribution in the coarse time step solution. However, the relative flux distribution is in quite good agreement with the reference FOM solution and the RMS difference for it is less than 10^{-4} %. Since only the relative spatial distribution of the scalar flux are necessary to calculate the orthogonal basis, the present results indicate that the coarse time step solution can be an alternate solution for the orthogonal basis construction. This characteristic also can be an advantage for the computation time because it means that the orthogonal basis for the natural mode flux distribution can be estimated with fewer computational costs with a coarse time step calculation. Figure 3.8 shows the singular values of the matrix, $\mathbf{M_K}$. Since the matrix $\mathbf{M_K}$ represents the solution space of the present kinetic calculation with the FOM, Figure 3.8 indicates the temporal variation of the flux distribution can be accurately represented by a small number of singular values. Note that the number of singular values is 22 because the 11 flux distributions are chosen to construct the matrix $\mathbf{M_K}$ and total number of energy groups is 2 in the TWIGL benchmark problem.

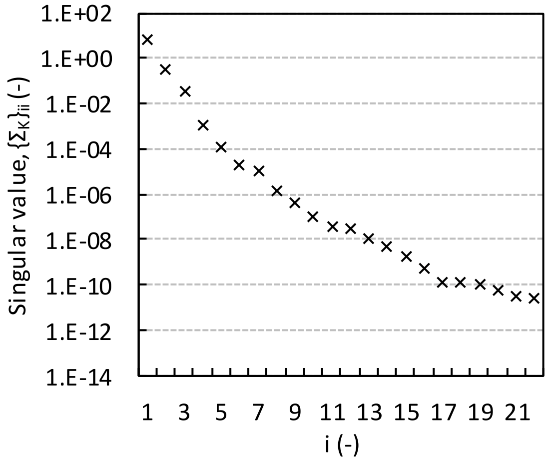

Figure 3.8 Singular values of the matrix, $\mathbf{M_K}$

In the present calculation, the order whose singular value is less than 10^{-8} is truncated and the dimensionality reduction for the coefficient matrices is carried out. Table 3.5 shows the case matrix of the present verification.

Table 3.5 Case matrix for the TWIGL benchmark problem

Test case	Size of orthogonal basis*	Size of coefficient matrices $(\hat{\mathbf{A}}_g, \hat{\mathbf{F}}_g, \hat{\mathbf{S}}_{g'\to g})$
BE-11	6400×11 ($\mathbf{U_E}$)	11×11
BK-13	6400×13 ($\mathbf{U_K}$)	13×13

* The dimensions whose singular value is less than 10^{-8}.

As shown in Table 3.5, the test cases, BE-11 and BK-13, indicate the difference in sampled flux distributions that are used to construct the orthogonal bases. The number after the case name, “BK

(Basis calculated from Kinetic calculations)", denotes the rank of the compressed coefficient matrices.

The test cases, BE-11 and BK-13, are calculated with Δt = 1 msec. Figure 3.9 shows the relative difference in the power between each test case and the FOM. The relative differences of the core power, RMS and maximum relative difference for mesh-wise power distribution are calculated as follows:

$$\text{Relative difference (\%)} = \frac{CP - CP^{FOM}}{CP^{FOM}} \times 100 \ , \tag{3.37}$$

$$\text{RMS difference (\%)} = \sqrt{\frac{1}{N}\sum_{j}^{N}\left(\frac{P_j - P_j^{FOM}}{P_j^{FOM}}\right)^2} \times 100 \ , \tag{3.38}$$

$$\text{Maximum relative difference (\%)} = \max\left|\frac{P_j - P_j^{FOM}}{P_j^{FOM}}\right| \times 100 \ , \tag{3.39}$$

where CP and P_j denote the core power and the power at mesh j. FOM is the superscript for the reference FOM solution calculated with Δt = 1 msec.

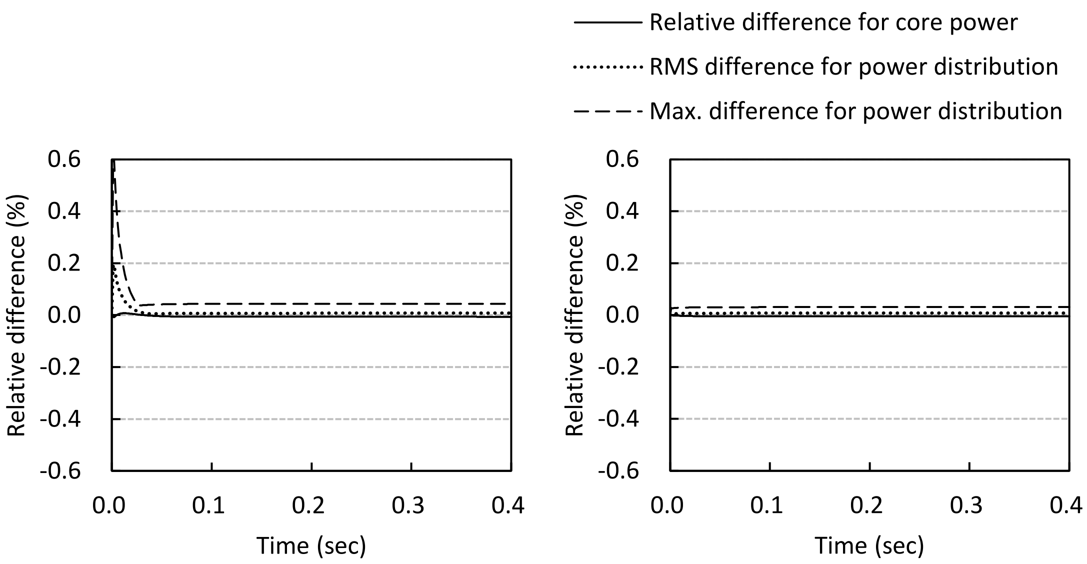

(a) BE-11 step perturbation

(b) BK-13 step perturbation

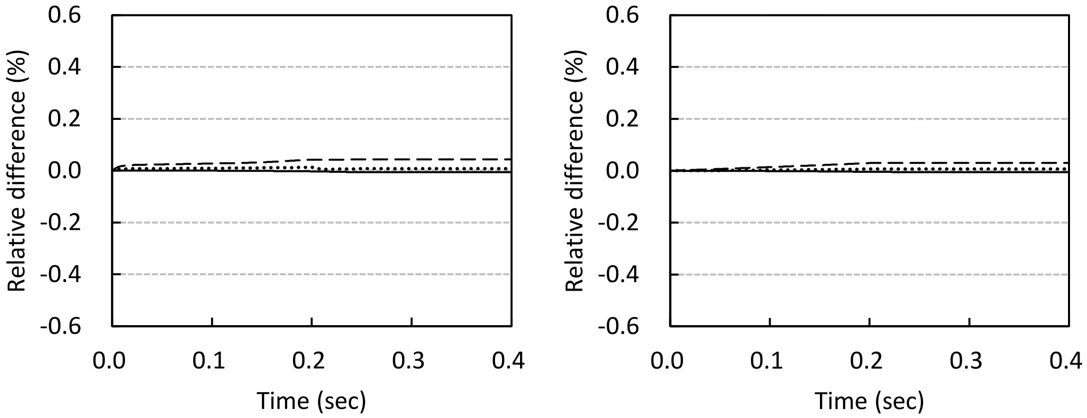

(c) BE-11 ramp perturbation

(b) BK-13 ramp perturbation

Figure 3.9 Variation of the core power and power distribution difference for the TWIGL benchmark problem

As shown in Figure 3.9, the reference FOM core power transients are successfully reproduced in both test cases. The power distributions are also in good agreement in both cases with less than 0.6 % in maximum even for rapid power increase by the step perturbation. Especially, the test case BK-13 shows better agreement with the reference FOM solution than BE-11. These results suggest that the higher-order natural mode of the flux distribution is important for accuracy and the coarse time step calculation is an effective approach for the orthogonal basis construction if the accurate relative flux distribution can be obtained in the coarse time step calculation. Figure 3.9 also shows that the accuracy of the test case BK-13 in the step perturbation condition is almost the same as that of the ramp perturbation condition. It suggests that the same orthogonal basis can be commonly used for the step and the ramp perturbation conditions in the present calculation condition.

As for the precursor density, Figure 3.10 shows the variation of the maximum relative difference of the expansion coefficients for the precursor density between the ROM ($\varsigma_{m,i}$) and reference FOM ($\varsigma_{m,i}^{ref}$) solutions as:

$$\text{Maximum relative difference (\%)} \quad = max\left|\frac{\varsigma_{m,i}-\varsigma_{m,i}^{ref}}{\varsigma_{m,i}^{ref}}\right| \times 100\ , \tag{3.40}$$

where the reference expansion coefficients in the FOM are calculated by Equation (3.41) using the orthogonal basis for each test case.

$$\vec{\varsigma}_m^{ref} = \mathbf{U}^{\mathbf{T}} \vec{C}_m^{FOM}. \tag{3.41}$$

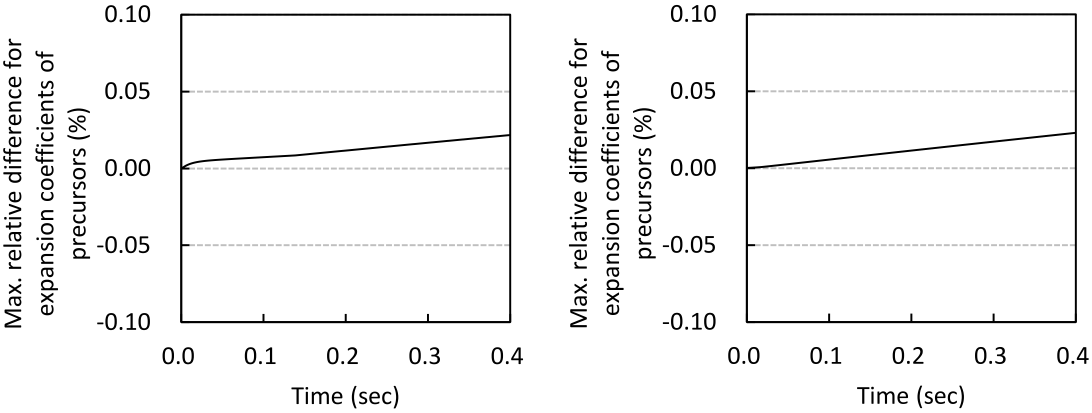

(a) BE-11 step perturbation (b) BK-13 step perturbation

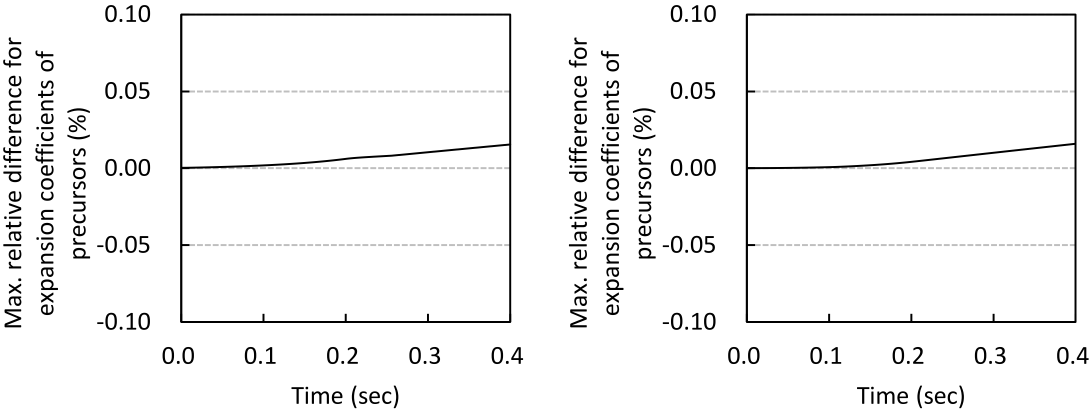

(c) BE-11 ramp perturbation (b) BK-13 ramp perturbation

Figure 3.10 Variation of maximum relative difference of expansion coefficients for precursor

As shown in Figure 3.10, the maximum error of the expansion coefficients for the precursor is less than 0.1 % during the transient and they are in good agreement with the reference solution in both test cases. The present results indicate that the error of expansion for the precursor density using the orthogonal basis calculated from scalar flux vectors has less impact on the accuracy in the TWIGL benchmark problem.

Finally, Table 3.6 shows the computation time of the ROM and the FOM. All calculations are carried out by a single thread on Intel(R) Core$^{\text{TM}}$ i9-9900K (3.6–5.0GHz) with 16 GB memory.

Table 3.6 Computation time of the TWIGL benchmark problem

(a) Elapsed time for the coefficient matrix preparation

	ROM (sec)		FOM
	BE-11	BK-13	(sec)
Flux distribution preparation	2.62*	1.12†	–
Singular value decomposition	0.16	0.15	–
Dimensionality reduction for coefficient matrices	2.35	2.38	–

[*] Elapsed time for eigenvalue calculations (0.238 sec/case × 11 cases = 2.62 sec)

[†] Elapsed time for the coarse time step kinetic calculation in the ramp perturbation condition

(b) Elapsed time for the kinetic calculation

Perturbation type	ROM (sec)		FOM
	BE-11	BK-13	(sec)
Step	0.25	0.28	17.19
Ramp	0.27	0.28	26.27

(c) Total elapsed time (=(a) + (b))

Perturbation type	ROM (sec)		FOM
	BE-11	BK-13	(sec)
Step	5.38	3.93	17.19
Ramp	5.40	3.93	26.27

As shown in Table 3.6, the present ROMs are about 100 times faster than the FOM for the kinetic calculation itself. If we consider the data preparation time for the orthogonal basis and the dimensionality reduction calculations, both test cases are still 3–6 times faster than the FOM. These results suggest that the present approach will be effective for fast core simulations whose calculation conditions can be predetermined, *e.g.*, online real-time monitoring is one of the candidates because the calculation geometry is fixed during the operation. Currently, it is difficult to apply the high fidelity simulations for it due to the limitation on the execution time. However, periodically calculating the various core situation nearby the current one even if it takes a longer time than real-time, an orthogonal basis that represents the solution space nearby the current core situation with fewer DOFs will be obtained by the SVD. Such an orthogonal basis will enable us the online real-time monitoring with the accuracy equivalent to high-fidelity simulation. The number of calculation cases to treat feedback effect and partial control rod insertion during transient would be an issue in future work.

In the present study, the diffusion calculation is employed as a FOM to see the feasibility of the ROM using the POD. However, the advantage of the POD will be larger for more detailed high-resolution models such as heterogeneous transport calculations because the correlation among the neutronic parameters will be higher thus compression efficiency becomes larger, *e.g.*, the correlation of the scalar fluxes between adjacent flux regions inside a fuel pin is much higher than that of adjacent fuel assemblies because of the distance between the meshes. In the next chapter, the application of the POD to the time-dependent transport calculations using MOC is investigated.

3.4. Conclusion

In this chapter, an efficient way to construct the proper orthogonal basis for kinetic calculations is investigated. In the present study, two types of different orthogonal bases, which are constructed from the scalar flux distributions of the steady-state eigenvalue or kinetic calculations of the FOM, are employed to construct ROMs using the POD. The accuracy and efficiency of the present ROMs are verified in the TWIGL benchmark problem.

The results reveal that both orthogonal bases obtained by the eigenvalue and kinetic calculations well reproduce the reference results while the orthogonal basis constructed using the kinetic calculations shows higher accuracy. As for the computation time, it is confirmed that the present ROMs achieve 100 times faster computation for the kinetic calculation itself than the FOM. When we consider the data preparation time for the dimensionality reduction to construct the ROM, they are still 3–6 times faster than the FOM. It should be also noted that the coarse time step calculations effectively capture the relative shape of the natural mode of flux distribution and shorten the computation time for the ROM construction in the present study. While the verification of the ROMs constructed from transient calculations, which is different from the target problem but inserted reactivity is comparable, is also carried out in the present study, there is less impact on the accuracy in the present calculation condition. It suggests that a dedicated orthogonal basis would not be necessary for various transients when the inserted reactivity is comparable. More comprehensive verification for this would be investigated in future work. These results suggest that the POD is effectively used for real-time applications when the calculation conditions or the computational geometry are predetermined and the variation of the flux distributions are constrained by them.

In this chapter, the diffusion calculation is employed as a FOM to see the feasibility of the ROM using the POD. However, the advantage of the POD will be larger for more detailed high-resolution models such as heterogeneous transport calculations. In the next chapter, the application of the POD for time-dependent MOC calculation is investigated.

3.5. Reference

[1] Tsujita K, Endo T, Yamamoto A. Application of the multigrid amplitude function method for time-dependent MOC based on the linear source approximation. J Nucl Sci Technol. 2020. 57:646–662.

[2] Abdel-Khalik H, Turinsky P, Jessee M. Efficient subspace methods-based algorithms for performing sensitivity, uncertainty, and adaptive simulation of large-scale computational models, Nucl. Sci. Eng. 2008; 159:256–272.

[3] Zhang S, Lu D, Wang T, Chao Y. A feasibility study of low-order harmonics expansion applied to loading pattern search. Proc PHYSOR 2006; Sep 10–14; Vancouver, Canada.

[4] Zhang S, Fu X, Wang T, Chao Y. Hybrid harmonics and linearization perturbation method for fast loading pattern evaluation. Proc PHYSOR2008, 2008 Sep 14–19, Interlaken, Switzerland.

[5] Wang W, Jiang X, Chao Y. Direct optimization of loading pattern search using the HHLP theory and the MILP method. Proc PHYSOR2010; 2010 May 9–14; Pittsburgh, PA.

[6] Yamamoto A, Endo T, Takeda S, Koike H, Yamaji K, Ieyama K, Sato D. A resonance calculation method using energy expansion bases based on a reduced order model. Proc M&C2019; 2019 Aug 25–29; Portland, Oregon.

[7] González-Pintor S, Ginestar D, Verdú G. Using proper generalized decomposition to compute the dominant mode of nuclear reactor. Math. Comput. Modell. 2013; 57:1807–1815.

[8] Alberti AL, Palmer TS. Reduced order modelling of the TWIGL problem using proper generalized decomposition. Proc M&C 2019; 2019 Aug 25–29; Oregon, Portland.

[9] Anttonen JSR, King PI, BERAN PS. POD-Based reduced-order models with deforming grids. Math. Comput. Modell. 2003; 38:41–62.

[10] Behne PA, Ragusa JC, Morel JE. Model order reduction for Sn radiation transport. Proc M&C 2019; 2019 Aug. 25–29; Oregon, Portland.

[11] Stacey WM, Space-time Nuclear Reactor Kinetics. New York: Academic Press; 1969.

[12] Katano R, Endo T, Yamamoto A, Abdo M, Abdel-Kahalik H. Estimation of sensitivity coefficients of core characteristics based on reduced-order modeling using sensitivity matrix of assembly characteristics. J Nucl Sci Technol. 2017;54(6):637–647. DOI: 10.1080/00223131.2017.1299052

[13] Hageman LA, Yasinsky JB. Comparison of alternating direction time differencing methods with other implicit methods for the solution of the neutron group diffusion equations. Nucl Sci Eng. 1969;38:8–32.

[14] Matsushita M, Endo T, Yamamoto A. Development of reduced order model of severe accident analysis code for probabilistic safety margin analysis. Proc PHYSOR 2018; 2018 Apr 22–26; Cancun, Mexico.

4. Efficient ROM based on the POD for time-dependent MOC calculations

4.1. Introduction

As discussed in Chapter 3, the construction of an orthogonal basis in the spatial domain and DR using the POD are quite effective ways to reduce the DOFs of the kinetic calculations since the calculation geometry itself is generally fixed during the transient and a large number of DOFs in the spatial domain are represented by the orthogonal basis. These results also suggest that the advantage of the POD will be larger for more detailed high-resolution models such as heterogeneous transport calculations because the correlation among the neutronic parameters will be higher thus compression efficiency becomes higher. Therefore, there is a possibility to achieve much faster computation without degrading the accuracy by applying the POD for time-dependent MOC calculations. However, there is a constraint that the neutron balance equation must be described in a matrix form to apply the POD. Since the neutron balance equation in the MOC is not generally described in a matrix form and enormous memory storage will be also required to describe all neutron balances along the neutron flight paths in a matrix form, it is quite difficult to directly apply the POD for MOC calculations. In past studies, the applications of the POD are found only in diffusion and S_N transport calculations and verified in simplified or homogeneous geometries [1–3].

Thus, in the present study, the way to construct a ROM that reproduces the time-dependent MOC solution in a heterogeneous geometry using the POD is investigated. In the present study, the coefficient matrices that reproduce a MOC solution are reconstructed using diffusion calculation with a correction term for neutron current, and then the POD is applied to it. The accuracy and the computation time of the present ROM are verified with the C5G7-TD 2D benchmark problem [4].

The remaining part of this chapter is organized as follows. The theoretical basis of the ROM for the time-dependent MOC calculations using the POD is described in Section 4.2. The numerical results and discussions are shown in Section 4.3. Finally, concluding remarks are summarized in Section 4.4.

4.2. Methodology

In the present study, the coefficient matrices that reproduce the MOC solution are reconstructed based on the diffusion calculation with a correction term. Then, the MOC-equivalent discretized diffusion equation is dimensionally reduced using the POD. In this section, the theoretical bases for the MOC-equivalent diffusion equation and the DR using the POD are described in Subsections 4.2.1 and 4.2.2, respectively.

4.2.1. Reconstruction of coefficient matrices for MOC

The time-dependent transport equation along a neutron flight path is written as:

$$\frac{1}{v_{g,r}}\frac{\partial \psi_{g,m,k,i}}{\partial t} = -\left(\frac{\partial}{\partial s} + \Sigma_{t,g,r}\right)\psi_{g,m,k,i} + \frac{1}{4\pi}Q_{g,r}\ , \tag{4.1}$$

$$Q_{g,r} = \sum_{j}\lambda_j \chi^{d}_{g,j,r} C_{j,r} + \sum_{g'}\Sigma_{s,g'\to g,r}\phi_{g',r} + (1-\beta_r)\chi^{p}_{g,r}\sum_{g'}\nu\Sigma_{f,g',r}\phi_{g',r}\ , \tag{4.2}$$

$$\beta_r = \sum_{j}\beta_{j,r}\ , \tag{4.3}$$

$$\frac{\partial C_{j,r}}{\partial t} = \beta_{j,r}\sum_{g'}\nu\Sigma_{f,g'}\phi_{g',r} - \lambda_j C_{j,r}\ , \tag{4.4}$$

where

s : coordinate along the neutron flight direction,

$v_{g,r}$: averaged neutron velocity,

$\phi_{g,r}$: scalar flux,

$\psi_{g,m,k,i}$: angular flux,

$\Sigma_{t,g,r}$: total cross section,

$\nu\Sigma_{f,g'}$: production cross section,

$\Sigma_{s,g'\to g}$: scattering cross section,

$\chi^{p}_{g,r}$: prompt fission spectrum,

$\chi^{d}_{g,j,r}$: delayed fission spectrum,

$C_{j,r}$: precursor density,

$\beta_{j,r}$: delayed neutron fraction,

λ_j : decay constant,

where g, j,m, k, i and r are the subscripts for energy group, delayed precursor family, neutron flight direction, sequential number of the neutron flight path, segment, and flux region, respectively. Figure 4.1 shows their definitions.

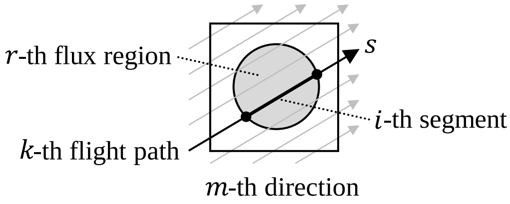

Figure 4.1 Neutron flight direction, flight path, segment, and flux region

The leakage term in Equation (4.1) is the matrix-free operator, which makes it difficult to directly apply the POD to the MOC. Integrating both sides of Equation (4.1) for the whole solid angle and spatially averaging it within each flux region,

$$\frac{1}{v_{g,r}}\frac{\partial \phi_{g,r}}{\partial t} = -\sum_{r'} \frac{J^{MOC}_{g,r\to r'} S_{r\to r'}}{V_r} - \Sigma_{t,g,r}\phi_{g,r} + Q_{g,r} , \tag{4.5}$$

where

$J^{MOC}_{g,r\to r'}$: net neutron current between the flux regions,

$S_{r\to r'}$: surface area between the adjacent flux regions,

V_r : volume of the flux region,

The net neutron current, $J^{MOC}_{g,r\to r'}$, is calculated as a summation of the incoming and outgoing angular fluxes between the adjacent regions as:

$$J^{MOC}_{g,r\to r'} S_{r\to r'} = \sum_m \sum_k \sum_{i\in r\to r'} \Delta J^{out}_{g,m,k,i} - \sum_m \sum_k \sum_{i\in r'\to r} \Delta J^{in}_{g,m,k,i} , \tag{4.6}$$

$$\Delta J^{out}_{g,m,k,i} = \Delta A_{m,k}\omega_m \psi^{out}_{g,m,k,i} \sin\theta_m , \tag{4.7}$$

$$\Delta J^{in}_{g,m,k,i} = \Delta A_{m,k}\omega_m \psi^{in}_{g,m,k,i} \sin\theta_m , \tag{4.8}$$

where

$\Delta A_{m,k}$: width of the neutron flight path,

θ_m : polar angle,

ω_m : solid angle weight,

$\psi^{out}_{g,m,k,i}$: outgoing angular flux from segment i,

$\psi^{in}_{g,m,k,i}$: incoming angular flux for segment i.

Note that Equations (4.6)–(4.8) can be calculated using the ray-tracing information and the present approach can be applied to any geometries in which the neutron flight paths can be defined. By describing the net neutron current with the finite difference method with a correction term as it is done in the CMFD method as [5]:

$$\frac{J^{MOC}_{g,r\to r'} S_{r\to r'}}{V_r} = -D^{FD}_{g,r\to r'}\left(\phi_{g,r'} - \phi_{g,r}\right) + D^{COR}_{g,r\to r'}\left(\phi_{g,r'} + \phi_{g,r}\right), \tag{4.9}$$

where $D^{FD}_{g,r\to r'}$ is a coupling coefficient and $D^{COR}_{g,r\to r'}$ is the correction factor to reproduce the net neutron current, $J^{MOC}_{g,r\to r'}$, between the adjacent flux regions, r and r'. In the present study, the coupling coefficient is calculated as:

$$D^{FD}_{g,r\to r'} = \frac{D_{g,r} D_{g,r'}}{\left(D_{g,r} + D_{g,r'}\right) S_r}, \tag{4.10}$$

where $D_{g,r}$ and S_r are the diffusion constant and the cross-sectional area of the flux region in the radial direction, respectively. Note that S_r in Equation (4.10) is different from the definition in the ordinary CMFD method to simplify the definition of the coupling coefficient for the unstructured mesh but the approximation error for it is corrected by $D^{COR}_{g,r\to r'}$. As for the boundary, the coefficient for neutron current is described as:

$$\frac{J^{MOC}_{g,r\to BC} S_{r\to BC}}{V_r} = -D^{BC}_{g,r} \phi_{g,r}, \tag{4.11}$$

where $J^{MOC}_{g,r\to BC}$ and $S_{r\to BC}$ are the net neutron current and surface area at the boundary, respectively. The coefficient for the neutron current, $D^{BC}_{g,r}$, is calculated so that it preserves the relationship in Equation (4.11). Substituting Equations (4.9), (4.10), and (4.11) into Equation (4.5), the MOC-equivalent neutron balance equation for each flux region is derived as:

$$\frac{1}{v_{g,r}} \frac{\partial \phi_{g,r}}{\partial t} = -\sum_{r'} A_{g,r'\to r} \phi_{g,r'} + Q_{g,r}, \tag{4.12}$$

where $A_{g,r'\to r}$ is the annihilation operator described as:

$$A_{g,r\to r} = \sum_{r'\neq r} \left(D^{COR}_{g,r\to r'} + D^{FD}_{g,r\to r'}\right) + \Sigma_{t,g,r} - D^{BC}_{g,r}, \tag{4.13}$$

$$A_{g,r'\to r} = D^{COR}_{g,r\to r'} - D^{FD}_{g,r\to r'} \quad (r \neq r'). \tag{4.14}$$

where $D^{BC}_{g,r} = 0$ for the flux region that is not facing the boundary.

Employing the fully implicit method for time integration [6], Equation (4.12) is described as:

$$\sum_{r'} \left(A^{n+1}_{g,r'\to r} + \frac{\delta_{r'r}}{v_g \Delta t} \right) \phi^{n+1}_{g,r'} = Q^{n+1}_{g,r} + S^{n}_{g,r} , \tag{4.15}$$

$$Q^{n+1}_{g,r} = \gamma_{g,r} \sum_{g'} \nu\Sigma^{n+1}_{f,g',r} \phi^{n+1}_{g',r} + \sum_{g'} \Sigma^{n+1}_{s,g'\to g,r} \phi^{n+1}_{g',r} , \tag{4.16}$$

$$\gamma_{g,r} = (1-\beta_r)\chi^{p}_{g,r} + \sum_{j} \lambda_j \xi_j \beta_{j,r} \chi^{d}_{g,j,r} , \tag{4.17}$$

$$S^{n}_{g,r} = \sum_{j} \lambda_j \chi^{d}_{g,j,r} \left(\mu_j C^{n}_{j,r} + \eta_j \beta_{j,r} P^{n}_{r} \right) + \frac{\phi^{n}_{g,r}}{v_g \Delta t} , \tag{4.18}$$

$$P^{n}_{r} = \sum_{g'} \nu\Sigma^{n}_{f,g',r} \phi^{n}_{g',r} , \tag{4.19}$$

$$C^{n+1}_{j,r} = \mu_j C^{n}_{j,r} + \eta_j \beta_{j,r} P^{n}_{r} + \xi_j \beta_{j,r} P^{n+1}_{r} , \tag{4.20}$$

where n is the superscript for a time step and $\delta_{r'r}$ is the Kronecker delta. μ_j, η_j, and ξ_j are the coefficients for temporal integration of precursors, which are derived assuming the linear transition of the fission source between the successive time steps as [6]:

$$\mu_j = \exp\left(-\lambda_j \Delta t\right) , \tag{4.21}$$

$$\eta_j = \frac{1}{\lambda_j} \left(\frac{1-\mu_j}{\lambda_j \Delta t} - \mu_j \right) , \tag{4.22}$$

$$\xi_j = \frac{1}{\lambda_j} \left(1 - \frac{1-\mu_j}{\lambda_j \Delta t} \right) . \tag{4.23}$$

Finally, the neutron balance equation for each flux region, which reproduces the neutron balance calculated with the MOC, is written in the following matrix form:

$$\left(\mathbf{A}^{\boldsymbol{n+1}}_{\boldsymbol{g}} + \frac{1}{\Delta t} \mathbf{V}^{\boldsymbol{inv}}_{\boldsymbol{g}} \right) \vec{\phi}^{n+1}_{g} = \vec{Q}^{n+1}_{g} + \vec{S}^{n}_{g} , \tag{4.24}$$

$$\vec{Q}^{n+1}_{g} = \mathbf{\Gamma}_{\boldsymbol{g}} \sum_{g'} \boldsymbol{\nu\Sigma}^{\boldsymbol{n+1}}_{\boldsymbol{f,g'}} \vec{\phi}^{n+1}_{g'} + \sum_{g'} \boldsymbol{\Sigma}^{\boldsymbol{n+1}}_{\boldsymbol{s,g'\to g}} \vec{\phi}^{n+1}_{g'} , \tag{4.25}$$

$$\mathbf{\Gamma}_{\boldsymbol{g}} = \boldsymbol{\chi}^{\boldsymbol{p}}_{\boldsymbol{g}} (\mathbf{I} - \boldsymbol{\beta}) + \sum_{j} \lambda_j \xi_j \boldsymbol{\chi}^{\boldsymbol{d}}_{\boldsymbol{g,j}} \boldsymbol{\beta}_{\boldsymbol{j}} , \tag{4.26}$$

$$\vec{S}^{n}_{g} = \sum_{j} \lambda_j \boldsymbol{\chi}^{\boldsymbol{d}}_{\boldsymbol{g,j}} \left(\mu_j \vec{C}^{n}_{j} + \eta_j \sum_{g'} \boldsymbol{\beta}_{\boldsymbol{j}} \boldsymbol{\nu\Sigma}^{\boldsymbol{n}}_{\boldsymbol{f,g'}} \vec{\phi}^{n}_{g'} \right) + \frac{1}{\Delta t} \mathbf{V}^{\boldsymbol{inv}}_{\boldsymbol{g}} \vec{\phi}^{n}_{g} , \tag{4.27}$$

$$\vec{C}_j^{n+1} = \mu_j \vec{C}_j^{n} + \eta_j \sum_{g'} \boldsymbol{\beta_j \nu \Sigma^{n}_{f,g'}} \vec{\phi}^{n}_{g'} + \xi_j \sum_{g'} \boldsymbol{\beta_j \nu \Sigma^{n+1}_{f,g'}} \vec{\phi}^{n+1}_{g'} \,, \tag{4.28}$$

where $\mathbf{I}$ is the identity matrix and the other matrices and vectors are described as follows:

$$\mathbf{A}_{\boldsymbol{g}}^{\boldsymbol{n+1}} = \begin{pmatrix} A^{n+1}_{g,1\to 1} & \cdots & A^{n+1}_{g,r'\to 1} & \cdots & A^{n+1}_{g,R\to 1} \\ \vdots & & \vdots & & \vdots \\ A^{n+1}_{g,1\to r} & \cdots & A^{n+1}_{g,r'\to r} & \cdots & A^{n+1}_{g,R\to r} \\ \vdots & & \vdots & & \vdots \\ A^{n+1}_{g,1\to R} & \cdots & A^{n+1}_{g,r'\to R} & \cdots & A^{n+1}_{g,R\to R} \end{pmatrix} , \tag{4.29}$$

$$\mathbf{V}_{\boldsymbol{g}}^{\boldsymbol{inv}} = \mathrm{diag}\left(\frac{1}{v_{g,1}} \quad \cdots \quad \frac{1}{v_{g,r}} \quad \cdots \quad \frac{1}{v_{g,R}} \right), \tag{4.30}$$

$$\boldsymbol{\nu\Sigma^{n+1}_{f,g}} = \mathrm{diag}\left(\nu\Sigma^{n+1}_{f,g,1} \ \cdots \ \nu\Sigma^{n+1}_{f,g,r} \ \cdots \ \nu\Sigma^{n+1}_{f,g,R} \right), \tag{4.31}$$

$$\boldsymbol{\Sigma^{n+1}_{s,g'\to g}} = \mathrm{diag}\left(\Sigma^{n+1}_{s,g'\to g,1} \ \cdots \ \Sigma^{n+1}_{s,g'\to g,r} \ \cdots \ \Sigma^{n+1}_{s,g'\to g,R} \right), \tag{4.32}$$

$$\boldsymbol{\beta} = \mathrm{diag}\left(\beta_1 \quad \cdots \quad \beta_r \quad \cdots \quad \beta_R \right), \tag{4.33}$$

$$\boldsymbol{\beta_j} = \mathrm{diag}\left(\beta_{j,1} \quad \cdots \quad \beta_{j,r} \quad \cdots \quad \beta_{j,R} \right), \tag{4.34}$$

$$\boldsymbol{\chi^{p}_{g}} = \mathrm{diag}\left(\chi^{p}_{g,1} \quad \cdots \quad \chi^{p}_{g,r} \quad \cdots \quad \chi^{p}_{g,R} \right), \tag{4.35}$$

$$\boldsymbol{\chi^{d}_{g,j}} = \mathrm{diag}\left(\chi^{d}_{g,j,1} \quad \cdots \quad \chi^{d}_{g,j,r} \quad \cdots \quad \chi^{d}_{g,j,R} \right), \tag{4.36}$$

$$\vec{\phi}^{n+1}_{g} = \left(\phi^{n+1}_{g,1} \quad \cdots \quad \phi^{n+1}_{g,r} \quad \cdots \quad \phi^{n+1}_{g,R} \right)^T, \tag{4.37}$$

$$\vec{C}^{n+1}_{j} = \left(C^{n+1}_{j,1} \quad \cdots \quad C^{n+1}_{j,r} \quad \cdots \quad C^{n+1}_{j,R} \right)^T, \tag{4.38}$$

where R is the number of flux regions in the calculation geometry. The size of the identity matrix in Equation (4.26) is also $R \times R$.

4.2.2. Dimensionality reduction using POD

Once the MOC-equivalent diffusion equation is derived in a matrix form, its DOFs can be reduced by the POD. In the POD approach, the flux and precursor density distributions are expanded by orthogonal bases suitable for the target problem, which are numerically obtained with the SVD for the distributions taken from the detailed FOM solutions. By substituting them for the neutron balance equation, the equation for the expansion coefficients that represents the target problem with fewer DOFs is obtained. In Chapter 3, an orthogonal basis that represents the flux distributions for all energy groups was employed to apply the POD. However, in this chapter, the orthogonal bases are respectively constructed for the scalar flux and precursor distributions at each energy group/precursor family as proposed in reference [1] to obtain more suitable bases that represent the parameter distributions with fewer DOFs. In this subsection, the equations for the expansion coefficients are derived by applying the POD to the MOC-equivalent diffusion equation.

The solution space of the scalar flux distributions, $\mathbb{R}_{\mathrm{F},g}$, is defined as:

$$\mathbb{R}_{\mathrm{F},g} \equiv \begin{pmatrix} \phi_{g,1}^{1} & \cdots & \phi_{g,1}^{N} \\ \vdots & & \vdots \\ \phi_{g,R}^{1} & \cdots & \phi_{g,R}^{N} \end{pmatrix}, \tag{4.39}$$

where N is the number of the scalar flux distributions taken from the FOM solution and $N < R$ is assumed in the following derivation. Applying the SVD for $\mathbb{R}_{\mathrm{F},g}$, an orthogonal basis for the target problem is obtained. In the present study, the thin SVD [7] is employed to reduce the computational cost of the decomposition:

$$\mathbb{R}_{\mathrm{F},g} = \mathbf{U}_{\mathbf{F},g}\mathbf{S}_{\mathbf{F},g}\mathbf{V}_{\mathbf{F},g}^{T}, \tag{4.40}$$

$$\begin{gathered} \mathbf{S}_{\mathbf{F},g} = \mathrm{diag}(\sigma_1 \quad \cdots \quad \sigma_K) \\ (\sigma_1 \geq \sigma_2 \geq \cdots \geq \sigma_K > 0), \end{gathered} \tag{4.41}$$

where σ and K denote the singular value and the rank of the solution space $\mathbb{R}_{\mathrm{F},g}$, respectively. The matrix $\mathbf{U}_{\mathbf{F}}$ contains the first K left singular vectors of the group g and its size is $R \times K$. $\mathbf{V}_{\mathbf{F}}$ consists of the first K right singular vectors of the group g and its size is $N \times K$. They are orthogonal bases for the column or row spaces of the solution space $\mathbb{R}_{\mathrm{F},g}$ so that

$$\mathbf{U}_{\mathbf{F},g}^{T}\mathbf{U}_{\mathbf{F},g} = \mathbf{I}, \tag{4.42}$$

$$\mathbf{V}_{\mathbf{F},g}^{T}\mathbf{V}_{\mathbf{F},g} = \mathbf{I}, \tag{4.43}$$

where $\mathbf{I}$ in Equations (4.41) and (4.42) is $K \times K$ identity matrix. Since the scalar flux distributions are represented in column space of $\mathbb{R}_{\mathrm{F},g}$, the flux distribution is expanded with $\mathbf{U}_{\mathbf{F},g}$ as:

$$\vec{\phi}_{g}^{n+1} = \mathbf{U}_{\mathbf{F},g}\vec{\varphi}_{g}^{n+1}, \tag{4.44}$$

$$\vec{\varphi}_{g}^{n+1} = \left(\varphi_{g,1}^{n+1} \quad \cdots \quad \varphi_{g,K}^{n+1}\right)^{T}, \tag{4.45}$$

where $\vec{\varphi}_{g}^{n+1}$ is the column vector of the expansion coefficients. Substituting Equation (4.44) into Equation (4.24) and multiplying the transposed orthogonal basis, the neutron balance equation for each flux region is converted into the equation for the expansion coefficients as:

$$\left(\widehat{\mathbf{A}}_{g}^{n+1} + \frac{1}{\Delta t}\widehat{\mathbf{V}}_{g}^{inv}\right)\vec{\varphi}_{g}^{n+1} = \vec{\mathcal{Q}}_{g}^{n+1} + \vec{\mathcal{S}}_{g}^{n}, \tag{4.46}$$

$$\widehat{\mathbf{A}}_{g}^{n+1} = \mathbf{U}_{\mathbf{F},g}^{T}\mathbf{A}_{g}^{n+1}\mathbf{U}_{\mathbf{F},g}, \tag{4.47}$$

$$\widehat{\mathbf{V}}_{g}^{inv} = \mathbf{U}_{\mathbf{F},g}^{T}\mathbf{V}_{g}^{inv}\mathbf{U}_{\mathbf{F},g}. \tag{4.48}$$

$$\vec{\mathcal{Q}}_{g}^{n+1} = \mathbf{U}_{\mathbf{F},g}^{T}\vec{Q}_{g}^{n+1}, \tag{4.49}$$

$$\vec{\mathcal{S}}_g^n = \mathbf{U}_{\mathbf{F},g}^T \vec{\mathcal{S}}_g^n \ . \tag{4.50}$$

Note that the size of the coefficient matrices on the left side of Equations (4.47) and (4.48) is reduced from $R \times R$ to $K \times K$. The source term, $\vec{\mathcal{Q}}_g^{n+1}$, is described as:

$$\vec{\mathcal{Q}}_g^{n+1} = \sum_{g'} \widehat{\boldsymbol{\nu\Sigma}}_{f,g'\to g}^{n+1} \vec{\varphi}_{g'}^{n+1} + \sum_{g'} \widehat{\boldsymbol{\Sigma}}_{s,g'\to g}^{n+1} \vec{\varphi}_{g'}^{n+1} \ , \tag{4.51}$$

$$\begin{aligned}\widehat{\boldsymbol{\nu\Sigma}}_{f,g'\to g}^{n+1} &= \mathbf{U}_{\mathbf{F},g}^T \boldsymbol{\Gamma}_g \boldsymbol{\nu\Sigma}_{f,g'}^{n+1} \mathbf{U}_{\mathbf{F},g'} \\ &= \mathbf{U}_{\mathbf{F},g}^T \boldsymbol{\chi}_g^p (\mathbf{I} - \boldsymbol{\beta}) \boldsymbol{\nu\Sigma}_{f,g'}^{n+1} \mathbf{U}_{\mathbf{F},g'} \\ &\quad + \sum_j \lambda_j \xi_j \mathbf{U}_{\mathbf{F},g}^T \boldsymbol{\chi}_{g,j}^d \boldsymbol{\beta}_j \boldsymbol{\nu\Sigma}_{f,g'}^{n+1} \mathbf{U}_{\mathbf{F},g'} \ ,\end{aligned} \tag{4.52}$$

$$\widehat{\boldsymbol{\Sigma}}_{s,g'\to g}^{n+1} = \mathbf{U}_{\mathbf{F},g}^T \boldsymbol{\Sigma}_{s,g'\to g}^{n+1} \mathbf{U}_{\mathbf{F},g'} \ , \tag{4.53}$$

where the left side of Equations (4.52) and (4.53) are also $K \times K$ matrices. In Equation (4.52), the production cross sections are compressed together with the fission spectrums. However, $\boldsymbol{\chi}_{g,j}^d$ and $\boldsymbol{\beta}_j \boldsymbol{\nu\Sigma}_{f,g}$ must be compressed separately to transform Equations (4.27) and (4.28) with the POD. Thus, in the present study, the matrices for the production cross section and the fission spectrum for the prompt fission are also separately compressed for the symmetry of the derivation. Then, Equation (4.52) is redefined from them. They are derived in the following procedure:

1. The prompt and delayed fission rate distribution vectors, $\vec{\mathcal{P}}_{PF}^{n+1}$ and $\vec{\mathcal{P}}_{DF,j}^{n+1}$, are employed to describe the fission source distributions. (Equations (4.54) and (4.55))
2. Employ the thin SVD for the solution spaces for the prompt and delayed fission rate distributions and obtain the orthogonal bases for them, $\mathbf{U}_{\mathbf{PF}}$ and $\mathbf{U}_{\mathbf{DF},j}$, respectively. (Equations (4.57)–(4.60))
3. Expand the prompt and delayed fission rate distributions, $\vec{\mathcal{P}}_{PF}^{n+1}$ and $\vec{\mathcal{P}}_{DF,j}^{n+1}$, with orthogonal bases, $\mathbf{U}_{\mathbf{PF}}$ and $\mathbf{U}_{\mathbf{DF},j}$. (Equations (4.61) and (4.62))
4. Compress the matrices for the prompt and delayed fission spectrum, $\boldsymbol{\chi}_g^p$ and $\boldsymbol{\chi}_{g,j}^d$, with orthogonal bases, $\mathbf{U}_{\mathbf{F},g}$, $\mathbf{U}_{\mathbf{PF}}$ and $\mathbf{U}_{\mathbf{DF},j}$. (Equations (4.64) and (4.65))
5. Compress the production cross section matrices for the prompt and delayed fission, $(\mathbf{I} - \boldsymbol{\beta})\boldsymbol{\nu\Sigma}_{f,g'}^{n+1}$ and $\boldsymbol{\beta}_j \boldsymbol{\nu\Sigma}_{f,g'}^{n+1}$, with orthogonal bases, $\mathbf{U}_{\mathbf{PF}}$, $\mathbf{U}_{\mathbf{DF},j}$ and $\mathbf{U}_{\mathbf{F},g}$. (Equations (4.68) and (4.69))
6. Redefine Equation (4.52) from Equations (4.64), (4.65), (4.68), and (4.69). (Equation (4.70))

The vectors for the prompt and delayed fission rate distributions, $\vec{\mathcal{P}}_{PF}^{n+1}$ and $\vec{\mathcal{P}}_{DF,j}^{n+1}$, are defined as:

$$\vec{\mathcal{P}}_{PF}^{n+1} = \sum_{g'} (\mathbf{I}-\boldsymbol{\beta})\boldsymbol{\nu\Sigma}_{\boldsymbol{f,g'}}^{\boldsymbol{n+1}}\mathbf{U}_{\mathbf{F},g'}\vec{\varphi}_{g'}^{n+1}\,, \tag{4.54}$$

$$\vec{\mathcal{P}}_{DF,j}^{n+1} = \sum_{g'} \boldsymbol{\beta}_{\boldsymbol{j}}\boldsymbol{\nu\Sigma}_{\boldsymbol{f,g'}}^{\boldsymbol{n+1}}\mathbf{U}_{\mathbf{F},g'}\vec{\varphi}_{g'}^{n+1}\,. \tag{4.55}$$

Using $\vec{\mathcal{P}}_{PF}^{n+1}$ and $\vec{\mathcal{P}}_{DF,j}^{n+1}$, the fission source term is described as:

$$\sum_{g'} \widehat{\boldsymbol{\nu\Sigma}}_{\boldsymbol{f,g'\to g}}^{\boldsymbol{n+1}}\vec{\varphi}_{g'}^{n+1} = \mathbf{U}_{\mathbf{F},g}^{\boldsymbol{T}}\boldsymbol{\chi}_{\boldsymbol{g}}^{\boldsymbol{p}}\vec{\mathcal{P}}_{PF}^{n+1} + \sum_{j} \lambda_j\xi_j\mathbf{U}_{\mathbf{F},g}^{\boldsymbol{T}}\boldsymbol{\chi}_{\boldsymbol{g,j}}^{\boldsymbol{d}}\vec{\mathcal{P}}_{DF,j}^{n+1}\,. \tag{4.56}$$

Note that the matrices for the fission spectrum can be separately compressed with the production cross section if the fission rate distributions are expanded with their orthogonal bases. Thus, the thin SVD is also employed to obtain the orthogonal bases for the solution spaces for the prompt and delayed fission rate distributions, $\mathbb{R}_{\mathrm{PF}}$ and $\mathbb{R}_{\mathrm{DF},j}$, as:

$$\mathbb{R}_{\mathrm{PF}} \equiv \begin{pmatrix} (1-\beta_1)P_1^1 & \dots & (1-\beta_1)P_1^N \\ \vdots & & \vdots \\ (1-\beta_R)P_R^1 & \dots & (1-\beta_R)P_R^N \end{pmatrix}, \tag{4.57}$$

$$\mathbb{R}_{\mathrm{DF},j} \equiv \begin{pmatrix} \beta_{j,1}P_1^1 & \dots & \beta_{j,1}P_1^N \\ \vdots & & \vdots \\ \beta_{j,R}P_R^1 & \dots & \beta_{j,R}P_R^N \end{pmatrix}, \tag{4.58}$$

$$\mathbb{R}_{\mathrm{PF}} = \mathbf{U}_{\mathbf{PF}}\mathbf{S}_{\mathbf{PF}}\mathbf{V}_{\mathbf{PF}}\,, \tag{4.59}$$

$$\mathbb{R}_{\mathrm{DF},j} = \mathbf{U}_{\mathbf{DF},\boldsymbol{j}}\mathbf{S}_{\mathbf{DF},\boldsymbol{j}}\mathbf{V}_{\mathbf{DF},\boldsymbol{j}}\,, \tag{4.60}$$

where the matrices $\mathbf{U}_{\mathbf{PF}}$, $\mathbf{S}_{\mathbf{PF}}$, $\mathbf{V}_{\mathbf{PF}}$, $\mathbf{U}_{\mathbf{DF},\boldsymbol{j}}$, $\mathbf{S}_{\mathbf{DF},\boldsymbol{j}}$, and $\mathbf{V}_{\mathbf{DF},\boldsymbol{j}}$ denote the $R \times K$ left singular vectors, $K \times K$ diagonal singular values, and the $N \times K$ right singular vectors for the solution space of the prompt and delayed fission rate distributions, respectively. The left and right singular vectors contain the first K vectors for each solution space. The rank of the solution space of the fission rate distributions is assumed as the same as that of flux distributions to simplify the notation, where it is not a necessary constraint. Using the orthogonal bases, the prompt and delayed fission rate distributions are expanded as:

$$\vec{\mathcal{P}}_{PF}^{n+1} = \mathbf{U}_{\mathbf{PF}}\vec{\varphi}_{PF}^{n+1}\,, \tag{4.61}$$

$$\vec{\mathcal{P}}_{DF,j}^{n+1} = \mathbf{U}_{\mathbf{DF},\boldsymbol{j}}\vec{\varphi}_{DF,j}^{n+1}\,, \tag{4.62}$$

where and $\vec{\varphi}_{PF}^{n+1}$ and $\vec{\varphi}_{DF,j}^{n+1}$ are the expansion coefficients for the prompt and delayed fission rate distributions, respectively. Substituting Equations (4.61) and (4.62) into Equation (4.56), the fission source is described as:

$$\begin{aligned}\sum_{g'} \widehat{\boldsymbol{\nu\Sigma}}_{\boldsymbol{f,g'\to g}}^{\boldsymbol{n+1}} \vec{\varphi}_{g'}^{n+1} &= \mathbf{U}_{\mathbf{F},\boldsymbol{g}}^{\boldsymbol{T}} \boldsymbol{\chi}_{\boldsymbol{g}}^{\boldsymbol{p}} \mathbf{U}_{\mathbf{PF}} \vec{\varphi}_{PF}^{n+1} + \sum_j \lambda_j \xi_j \mathbf{U}_{\mathbf{F},\boldsymbol{g}}^{\boldsymbol{T}} \boldsymbol{\chi}_{\boldsymbol{g,j}}^{\boldsymbol{d}} \mathbf{U}_{\mathbf{DF},\boldsymbol{j}} \vec{\varphi}_{DF,j}^{n+1} \\ &= \hat{\boldsymbol{\chi}}_{\boldsymbol{g}}^{\boldsymbol{p}} \vec{\varphi}_{PF}^{n+1} + \sum_j \lambda_j \xi_j \hat{\boldsymbol{\chi}}_{\boldsymbol{g,j}}^{\boldsymbol{d}} \vec{\varphi}_{DF,j}^{n+1} ,\end{aligned} \tag{4.63}$$

where $\hat{\boldsymbol{\chi}}_{\boldsymbol{g}}^{\boldsymbol{p}}$ and $\hat{\boldsymbol{\chi}}_{\boldsymbol{g,j}}^{\boldsymbol{d}}$ are the compressed matrices for the prompt and delayed fission spectrum described as:

$$\hat{\boldsymbol{\chi}}_{\boldsymbol{g}}^{\boldsymbol{p}} = \mathbf{U}_{\mathbf{F},\boldsymbol{g}}^{\boldsymbol{T}} \boldsymbol{\chi}_{\boldsymbol{g}}^{\boldsymbol{p}} \mathbf{U}_{\mathbf{PF}} , \tag{4.64}$$

$$\hat{\boldsymbol{\chi}}_{\boldsymbol{g,j}}^{\boldsymbol{d}} = \mathbf{U}_{\mathbf{F},\boldsymbol{g}}^{\boldsymbol{T}} \boldsymbol{\chi}_{\boldsymbol{g,j}}^{\boldsymbol{d}} \mathbf{U}_{\mathbf{DF},\boldsymbol{j}} . \tag{4.65}$$

Substituting Equations (4.54) and (4.55) into Equations (4.61) and (4.62) respectively, the matrices for the production cross section are also compressed as:

$$\vec{\varphi}_{PF}^{n+1} = \mathbf{U}_{\mathbf{PF}}^{\boldsymbol{T}} \vec{\mathcal{P}}_{PF}^{n+1} = \sum_{g'} \mathbf{U}_{\mathbf{PF}}^{\boldsymbol{T}} (\mathbf{I} - \boldsymbol{\beta}) \boldsymbol{\nu\Sigma}_{\boldsymbol{f,g'}}^{\boldsymbol{n+1}} \mathbf{U}_{\mathbf{F},\boldsymbol{g'}} \vec{\varphi}_{g'}^{n+1} = \sum_{g'} \widehat{\boldsymbol{\Sigma}}_{\mathbf{PF},\boldsymbol{g'}}^{\boldsymbol{n+1}} \vec{\varphi}_{g'}^{n+1}, \tag{4.66}$$

$$\vec{\varphi}_{DF,j}^{n+1} = \mathbf{U}_{\mathbf{DF},\boldsymbol{j}}^{\boldsymbol{T}} \vec{\mathcal{P}}_{DF,j}^{n+1} = \sum_{g'} \mathbf{U}_{\mathbf{DF},\boldsymbol{j}}^{\boldsymbol{T}} \boldsymbol{\beta}_{\boldsymbol{j}} \boldsymbol{\nu\Sigma}_{\boldsymbol{f,g'}}^{\boldsymbol{n+1}} \mathbf{U}_{\mathbf{F},\boldsymbol{g'}} \vec{\varphi}_{g'}^{n+1} = \sum_{g'} \widehat{\boldsymbol{\Sigma}}_{\mathbf{DF},\boldsymbol{g',j}}^{\boldsymbol{n+1}} \vec{\varphi}_{g'}^{n+1}, \tag{4.67}$$

where $\widehat{\boldsymbol{\Sigma}}_{\mathbf{PF},\boldsymbol{g'}}^{\boldsymbol{n+1}}$ and $\widehat{\boldsymbol{\Sigma}}_{\mathbf{DF},\boldsymbol{g',j}}^{\boldsymbol{n+1}}$ are the compressed matrices for the prompt and delayed production cross sections described as:

$$\widehat{\boldsymbol{\Sigma}}_{\mathbf{PF},\boldsymbol{g'}}^{\boldsymbol{n+1}} = \mathbf{U}_{\mathbf{PF}}^{\boldsymbol{T}} (\mathbf{I} - \boldsymbol{\beta}) \boldsymbol{\nu\Sigma}_{\boldsymbol{f,g'}}^{\boldsymbol{n+1}} \mathbf{U}_{\mathbf{F},\boldsymbol{g'}} , \tag{4.68}$$

$$\widehat{\boldsymbol{\Sigma}}_{\mathbf{DF},\boldsymbol{g',j}}^{\boldsymbol{n+1}} = \mathbf{U}_{\mathbf{DF},\boldsymbol{j}}^{\boldsymbol{T}} \boldsymbol{\beta}_{\boldsymbol{j}} \boldsymbol{\nu\Sigma}_{\boldsymbol{f,g'}}^{\boldsymbol{n+1}} \mathbf{U}_{\mathbf{F},\boldsymbol{g'}} . \tag{4.69}$$

Note that both the production cross sections and fission spectrum for the prompt and delayed fission are described as $K \times K$ matrices for each energy group. The coefficient matrix for the fission source can be reconstructed from them by substituting Equations (4.66) and (4.67) into Equation (4.63) as:

$$\widehat{\boldsymbol{\nu\Sigma}}_{\boldsymbol{f,g'\to g}}^{\boldsymbol{n+1}} = \hat{\boldsymbol{\chi}}_{\boldsymbol{g}}^{\boldsymbol{p}} \widehat{\boldsymbol{\Sigma}}_{\mathbf{PF},\boldsymbol{g'}}^{\boldsymbol{n+1}} + \sum_j \lambda_j \xi_j \hat{\boldsymbol{\chi}}_{\boldsymbol{g,j}}^{\boldsymbol{d}} \widehat{\boldsymbol{\Sigma}}_{\mathbf{DF},\boldsymbol{g',j}}^{\boldsymbol{n+1}} . \tag{4.70}$$

As for the pseudo source term, substituting Equation (4.27) into Equation (4.50) and using Equations (4.65) and (4.69),

$$\vec{\mathcal{S}}_g^n = \sum_j \lambda_j \mu_j \mathbf{U}_{\mathbf{F},\boldsymbol{g}}^{\boldsymbol{T}} \boldsymbol{\chi}_{\boldsymbol{g,j}}^{\boldsymbol{d}} \vec{C}_j^n + \sum_j \lambda_j \eta_j \hat{\boldsymbol{\chi}}_{\boldsymbol{g,j}}^{\boldsymbol{d}} \sum_{g'} \widehat{\boldsymbol{\Sigma}}_{\mathbf{DF},\boldsymbol{g',j}}^{\boldsymbol{n}} \vec{\varphi}_{g'}^n + \frac{1}{\Delta t} \widehat{\mathbf{V}}_{\boldsymbol{g}}^{\boldsymbol{inv}} \vec{\varphi}_g^n . \tag{4.71}$$

Since the DOFs of the precursor density distribution, $\vec{C}_j^n$, is still that of the FOM, assuming the precursor density can be expanded with the orthogonal basis for the delayed fission rate distribution, $\mathbf{U}_{\mathbf{DF},\boldsymbol{j}}$, as:

$$\vec{C}_j^n = \mathbf{U}_{\mathbf{DF},\boldsymbol{j}}\vec{\varsigma}_j^n \ , \tag{4.72}$$

where $\vec{\varsigma}_j^n$ denotes the expansion coefficients for the precursor density distribution. Substituting Equations (4.72) into Equation (4.71) and using Equation (4.65), the pseudo source term is described as:

$$\vec{s}_g^n = \sum_j \lambda_j \mu_j \hat{\boldsymbol{\chi}}^{\boldsymbol{d}}_{\boldsymbol{g},\boldsymbol{j}} \vec{\varsigma}_j^n + \sum_j \lambda_j \eta_j \hat{\boldsymbol{\chi}}^{\boldsymbol{d}}_{\boldsymbol{g},\boldsymbol{j}} \sum_{g'} \hat{\boldsymbol{\Sigma}}^{\boldsymbol{n}}_{\mathbf{DF},\boldsymbol{g'},\boldsymbol{j}} \vec{\varphi}^n_{g'} + \frac{1}{\Delta t} \hat{\mathbf{V}}^{\boldsymbol{inv}}_{\boldsymbol{g}} \vec{\varphi}^n_g \ . \tag{4.73}$$

Finally, multiplying the transposed orthogonal basis for delayed fission rate distribution, $\mathbf{U}^{\boldsymbol{T}}_{\mathbf{DF},\boldsymbol{j}}$, for Equation (4.28) and using Equations (4.44), (4.69), and (4.72) for it, the temporal integration for the expansion coefficient of the precursor density is described as:

$$\vec{\varsigma}_j^{n+1} = \mu_j \vec{\varsigma}_j^n + \eta_j \sum_{g'} \hat{\boldsymbol{\Sigma}}^{\boldsymbol{n}}_{\mathbf{DF},\boldsymbol{g'},\boldsymbol{j}} \vec{\varphi}^n_{g'} + \xi_j \sum_{g'} \hat{\boldsymbol{\Sigma}}^{\boldsymbol{n+1}}_{\mathbf{DF},\boldsymbol{g'},\boldsymbol{j}} \vec{\varphi}^{n+1}_{g'} \ , \tag{4.74}$$

Note that Equations (4.46), (4.51), (4.73), and (4.74) are the equations for expansion coefficients and they can be solved with fewer DOFs than the balance equation in the FOM. However, since the coefficient matrices before the DR are taken from the FOM solution, the compressed coefficient matrices are only available at the sampled time steps. Thus, the compressed coefficient matrices are interpolated between the successive sampled time steps. The accuracy of the interpolation is verified in Subsection 4.3.1.

4.3. Numerical results

In the present verifications, the C5G7-TD 2D benchmark problem [4] is used to verify the accuracy and performance of the present ROM. The following 3 exercises provided for the 2D benchmark calculation are used in the present verification. Each exercise includes multiple test problems with different perturbation conditions, *i.e.*, TD1-1– TD3-4. In all test problems, the cross sections linearly vary for t = 0.0 sec – 1.0 sec and 1.0 sec – 2.0 sec, respectively.

(3) TD1 : 1% control rod insertion and withdrawal transient
(4) TD2 : 10% control rod insertion and withdrawal transient
(5) TD3 : Moderator density change transient

The present verifications consist of 2 parts. Subsection 4.3.1 shows verification for the time dependence on the compressed coefficient matrices. Subsection 4.3.2 shows the verification of the computational efficiency of the ROM construction. In the present verification, all FOM calculations are carried out with the in-house 2D MOC code that has been verified in Appendix.

4.3.1. Verification for time dependence on coefficient matrices

In this subsection, the time dependence on the compressed coefficient matrices is verified. Table 4.1 and Figure 4.2 show the calculation condition of the reference FOM solution and the spatial mesh structure, respectively. The reference solutions are calculated with the same calculation conditions for each test problem in the present verification.

Table 4.1 Calculation conditions of reference FOM solution

Parameters	Calculation conditions
Azimuthal division	128 for 2π with cyclic quadrature set [8]
Polar division	3 for $\pi/2$ with TY-opt quadrature set [9]
Ray separation	0.01 cm using cyclic ray tracing
Convergence criterion	Fission : 10^{-8}, flux : 10^{-8}
Source approximation	Linear source approximation [10, 11]
Time discretization	MAF method
Time step size	Amplitude function : 10 msec Shape function : 500 msec[*]
Mesh structure for amplitude functions	1.26 cm × 1.26 cm for all meshes
Mesh structure for shape functions	Reflector cell : 0.42 cm × 0.42 cm square mesh Other cells : Material boundary + 8 azimuthal angle (31501 regions)

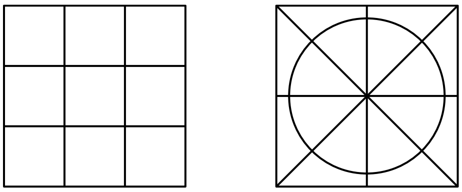
(a) Reflector cells (b) Other cells

Figure 4.2 Mesh structure for reference FOM calculation

---

[*] In the present verification, finer time step size for shape function than section 2.3.2 to see the non-linearity of the coefficient matrices.

As shown in Table 4.1, the MAF method and the linear source approximation, which is developed in Chapter 2, are employed to reduce the temporal and spatial discretization error in the FOM calculation, respectively. Figure 4.3 shows the core power transitions of the reference solutions.

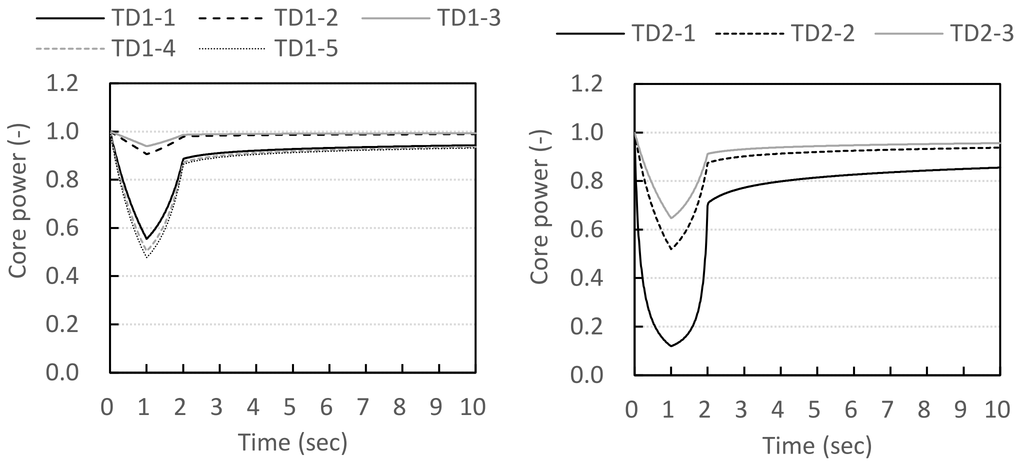

(a) TD1 (b) TD2

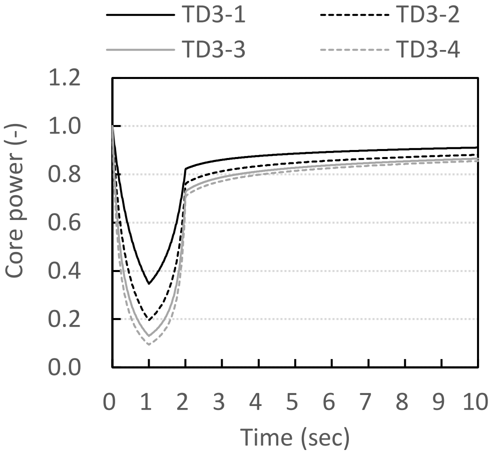

(c) TD3

Figure 4.3 Reference FOM solution for core power transition

Since the C5G7-TD 2D benchmark problem is the transient calculations for 10 sec and the time step size for the shape function is 500 msec in the present calculation condition, 21 flux distributions and the coefficient matrices are taken from the reference solutions for each test problem, *i.e.*, TD1-1, TD1-2, etc. Thus, the solution space for each test problem is described as a 31501×21 matrix, where 31501 is the number of flux regions in the reference solution. In the present verification, the thin SVD is applied for each solution space and the orthogonal bases are independently constructed, where the size of the orthogonal bases is also 31501×21 for each test problem. Thus, note that the present orthogonal bases focus to represent the transitions of the parameter distributions in each test problem with minimum DOFs, and all of the 21 flux distributions taken from the FOM can be accurately expanded by the orthogonal bases. Figure 4.4 shows the singular values of solution space for the flux, prompt and delayed fission rate distributions in the test problem, TD3-4.

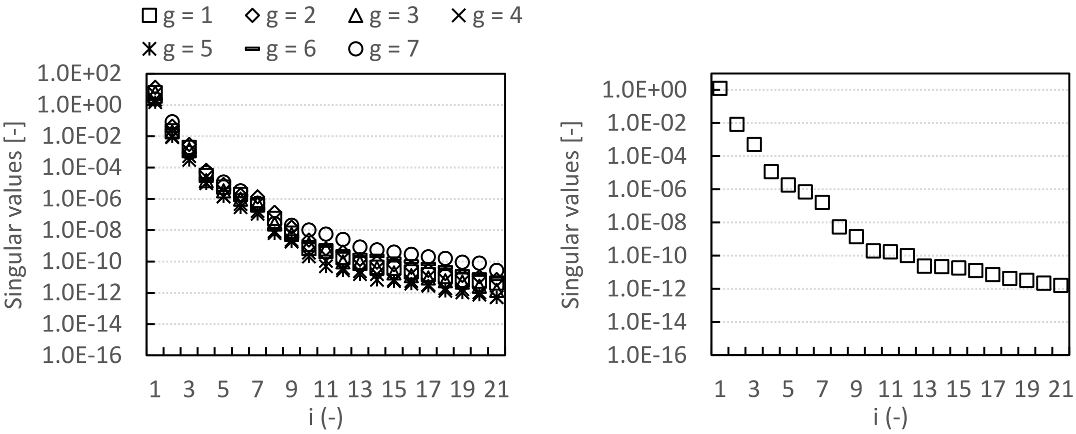

(a) Flux distribution

(b) Prompt fission rate distribution

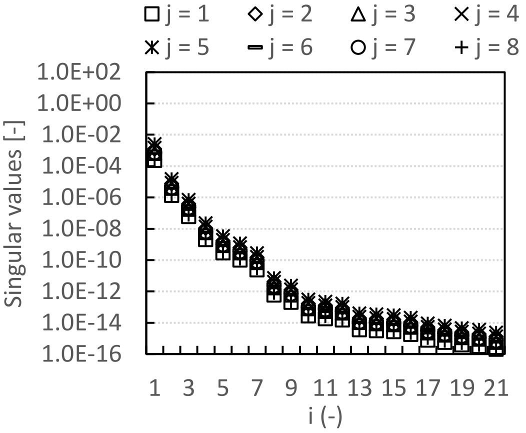

(c) Delayed fission rate distribution

Figure 4.4 Singular values for flux, prompt and delayed fission rate distributions (TD3-4)

As shown in Figure 4.4, the singular values, which indicate the contribution of each column vector in the orthogonal basis to the solution space, are rapidly decreasing. Since the column vectors corresponding to small singular values have less impact on the representation of the solution space, it can be seen that the solution space is accurately represented by a small number of dimensions. The major trend of the singular values is almost the same in the other test problems.

In the present verification, 3 ROMs are constructed based on different calculation conditions. Table 4.2 shows the case matrix for the ROM construction. Note that the low-rank approximation for the orthogonal bases is not employed in the present verification, *i.e.*, the size of the orthogonal bases used for the DR is also 31501×21 and that of compressed coefficient matrices $\widehat{\mathbf{A}}_{\boldsymbol{g}}^{\boldsymbol{n+1}}$ is 21×21, respectively. Since the size of the coefficient matrices before the DR with the POD, $\mathbf{A}_{\boldsymbol{g}}^{\boldsymbol{n+1}}$, is 31501×31501, the DOF the target problem is dramatically reduced with the POD.

Table 4.2 Case matrix for verification on time dependence of coefficient matrices

Case name	Sampling interval for coefficient matrices	Interpolation for matrices
Case 1	1.0 sec (11 steps)	Linear interpolation
Case 2	0.5 sec (21 steps)	Linear interpolation
Case 3	0.5 sec (21 steps)	Quadratic interpolation

As shown in Table 4.2, case 1 utilizes the coefficient matrices generated by 1.0 sec interval samplings and the matrices are linearly interpolated within the sampled time steps. Thus, it includes a larger interpolation error for the compressed coefficient matrices than the other cases. Case 2 is constructed with the finer sampling intervals for the coefficient matrices, 0.5 sec. However, if the coefficients in the compressed matrices vary non-linearly in time, the interpolation error for the coefficient matrices degrades the accuracy of the present ROM. Case 3 is constructed with the same sampling intervals as case 2 but the coefficient matrices are quadratically interpolated. Figure 4.5 shows the typical transition of a coefficient in the compressed matrix $\widehat{\mathbf{A}}_{\boldsymbol{g}}^{\boldsymbol{n+1}}$ for the test problem, TD3-4.

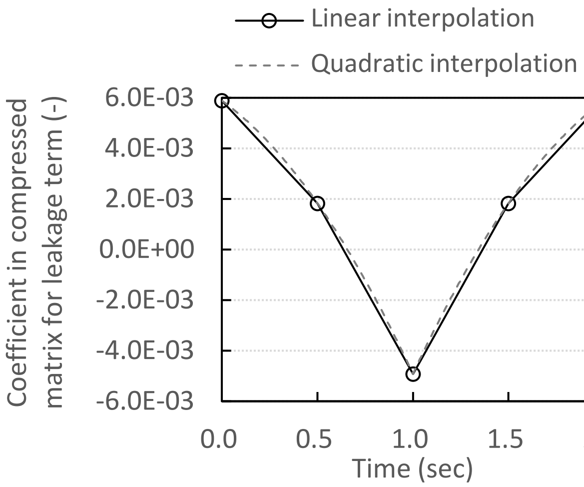

Figure 4.5 Typical transition of coefficient in the compressed coefficient matrix

As shown in Figure 4.5, the coefficient in the compressed matrix non-linearly varies during perturbation, where the discontinuity of the coefficient at t = 1.0 sec comes from the perturbation condition that the moderator density reaches a minimum at that point. Since the cross sections linearly vary in the C5G7-TD 2D benchmark problem, this non-linearity comes from the correction factor for neutron current, $D_{g,r\to r'}^{COR}$. In case 3, the interpolation intervals are selected as follows to avoid the overshoot of the interpolation:

(1) t = 0.0 sec – 1.0 sec : quadratic interpolation with t = 0.0, 0.5, 1.0 sec

(2) t = 1.0 sec – 2.0 sec : quadratic interpolation with t = 1.0, 1.5, 2.0 sec

(3) t = 2.0 sec – 10.0 sec : quadratic interpolation with the nearest 3 time steps after t = 2.0 sec

The time step size for the present ROMs is 10 msec for all test cases, which is the same as that of the amplitude function in the reference solution.

Figures 4.6 and 4.7 show the relative difference for the core power and the maximum relative difference for the flux distributions with respect to the reference FOM solution, where the relative differences are calculated as:

$$\frac{CP^{ROM} - CP^{FOM}}{CP^{FOM}} \times 100\ (\%)\ , \tag{4.75}$$

$$\max_{g\in G} \left| \frac{\vec{\phi}_g^{n,ROM} - \vec{\phi}_g^{n,FOM}}{\vec{\phi}_g^{n,FOM}} \right| \times 100\ (\%)\,, \tag{4.76}$$

where CP denotes the core power. The superscripts, FOM and ROM, denote the FOM and the ROM solutions, respectively. Note that the difference among the cases shows the impact of the interpolation error of the compressed coefficient matrices in Figures 4.6 and 4.7 since the same orthogonal bases are used for the DR in all cases, Cases 1–3.

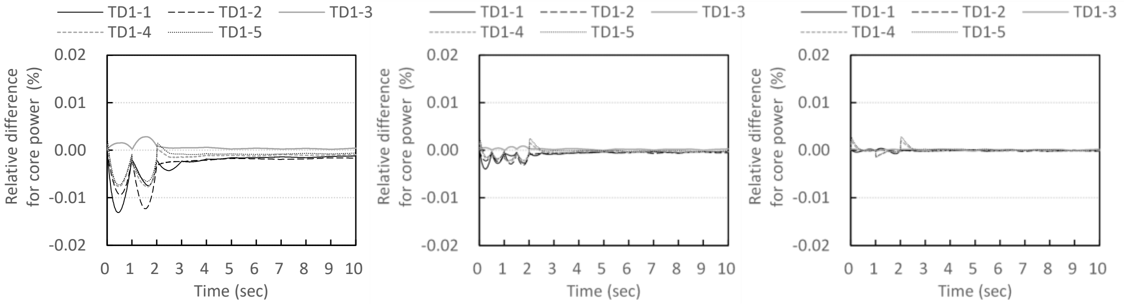

(a) TD1 – Case 1 (b) TD1 – Case 2 (c) TD1 – Case 3

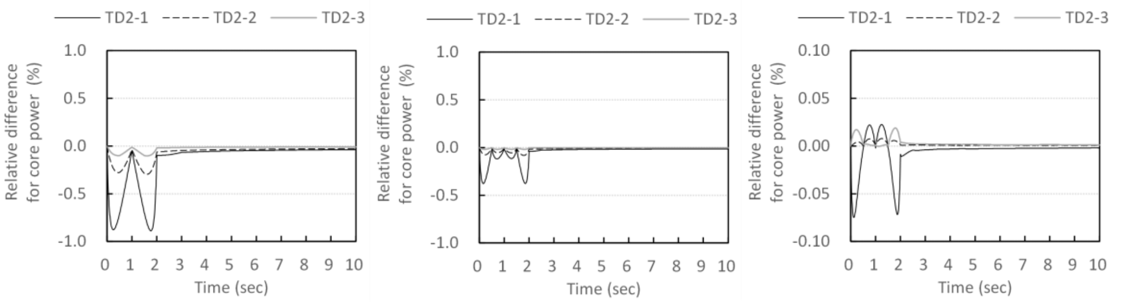

(d) TD2 – Case 1 (e) TD2 – Case 2 (f) TD2 – Case 3

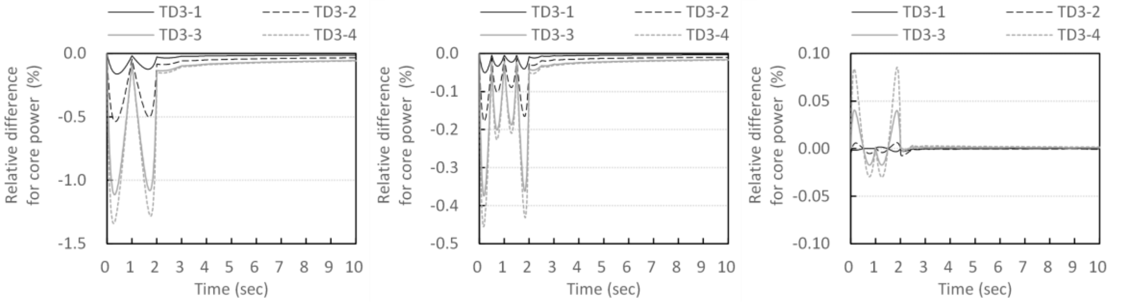

(g) TD3 – Case 1 (h) TD3 – Case 2 (i) TD3 – Case 3

Figure 4.6 Transition of relative difference for core power (case 1–3)

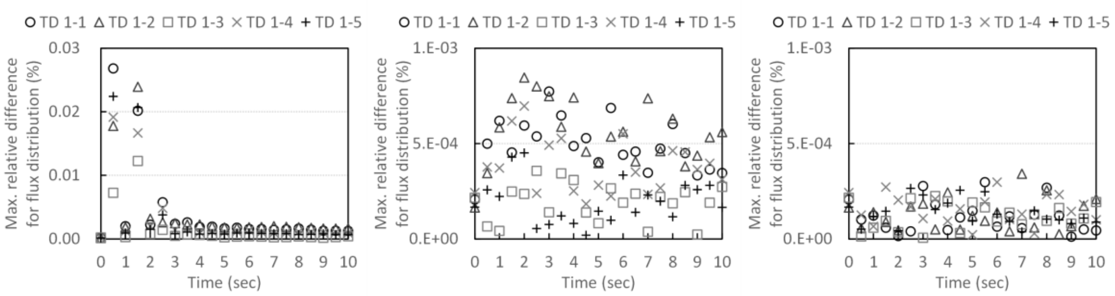

(a) TD1 – Case 1 (b) TD1 – Case 2 (c) TD1 – Case 3

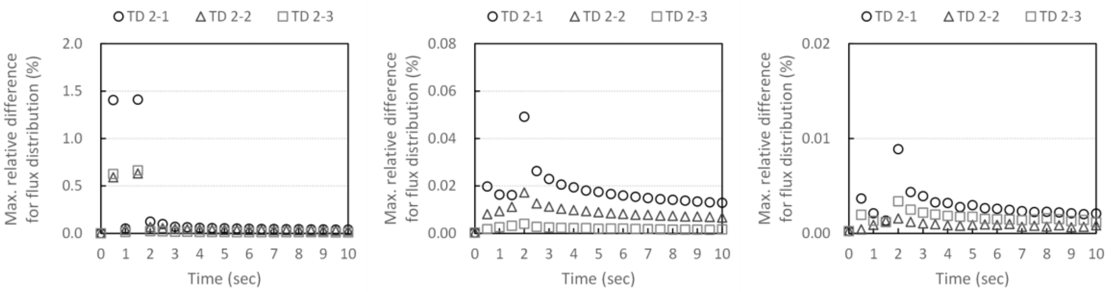

(d) TD2 – Case 1 (e) TD2 – Case 2 (f) TD2 – Case 3

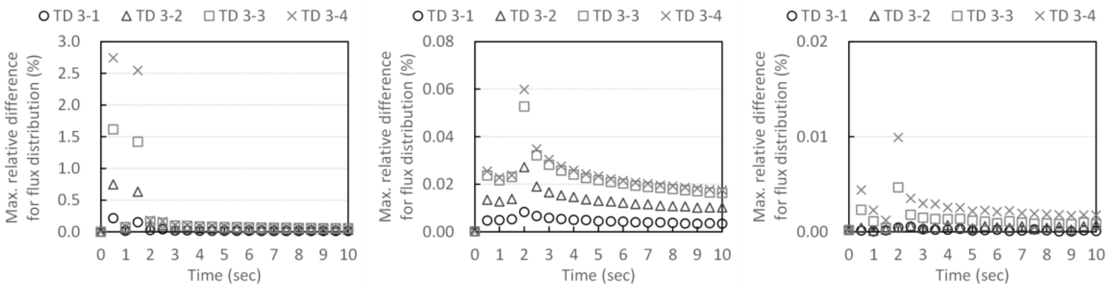

(g) TD3 – Case 1 (h) TD3 – Case 2 (i) TD3 – Case 3

Figure 4.7 Transition of maximum relative difference for flux distribution (case 1–3)

As shown in Figures 4.6 and 4.7, all cases in TD1 are in good agreement with the reference solution since the reactivity insertion and the variations of the coefficient matrices are small. However, there is a noticeable trend for TD2 and TD3 among the test cases especially from t = 0 sec to 2 sec. These results show the impact of the non-linearity of the coefficient matrices. Since all cross sections are linearly perturbed in the exercises TD1–TD3 and the spatial homogenization across the material boundary is not employed in the present study, the non-linearity appears only in the correction term for the neutron current in the present calculation condition. Thus, case 3 which employs non-linear interpolation for the coefficient matrices shows a better agreement with the reference FOM solution, and the oscillations of the relative difference of the core power in case 3 are caused by interpolation error of cubic or higher order in the compressed coefficient matrices. These results suggest the effectiveness of the non-linear interpolation for the compressed coefficient matrices.

4.3.2. Verification for computational efficiency of ROM construction

In the previous subsection, the present ROM is constructed from the reference solution to see the impact on the temporal discretization error for the coefficient matrices. However, the FOM calculation used for the ROM construction should be carried out more efficiently in practical applications. Thus, an efficient way to construct the present ROM is investigated in this subsection. Chapter 3 reveals that coarse step calculations are an effective way to construct an orthogonal basis when the relative shape of the solution space, *i.e.*, flux distributions, are comparable between the reference and coarse step calculations. However, the temporal discretization error will also affect the reconstructed coefficient matrices for the leakage term in the present ROM. Thus, the accuracy of the present ROM constructed from coarse time step calculation is compared with the reference FOM solution in the present verification. Table 4.3 shows the calculation conditions for the coarse step FOM calculation.

Table 4.3 Calculation conditions for coarse step calculation

Parameters	Calculation conditions
Azimuthal division	128 for 2π with cyclic quadrature set [8]
Polar division	3 for π/2 with TY-opt quadrature set [9]
Ray separation	0.01 cm using cyclic ray tracing
Convergence criterion	Fission : 10^{-8}, flux : 10^{-8}
Source approximation	Linear source approximation [10, 11]
Time discretization	Fully implicit method for flux[†], analytical solution assuming the linear transition of the fission sources for precursor [6]
Time steps	t = 0.0, 0.5, 1.0, 1.5, 2.0, 3.0, 6.5, 10.0 sec (8 steps)
Mesh structure	Reflector cell : 0.42 cm × 0.42 cm square mesh Other cells : Material boundary + 8 azimuthal angle (31501 regions)

As shown in Table 4.3, the fully implicit method[†] and the analytical solution assuming the linear transition of the fission sources between the successive time steps [6] are employed for the time integration for fluxes and precursors to reduce the computation time, respectively. The flux distributions are available only in 8 steps from the coarse time step FOM solution. The other calculation conditions are the same as the reference solution. Figure 4.8 shows the transition of the maximum relative differences of the flux distributions and the normalized flux distributions with respect to the reference solution, which is calculated as follows:

$$\max_{g\in G}\left|\frac{\vec{\phi}_g^{n',CTS}-\vec{\phi}_g^{n,ref}}{\vec{\phi}_g^{n,ref}}\right|\times 100\ (\%)\,, \tag{4.77}$$

[†] The calculation with the fully implicit method is carried out as the MAF method calculation with the fixed dynamic frequency and amplitude function, , *i.e.*, $\omega_{g,I}(t)=0$ and $P_{g,I}(t)=1$, using the equivalence of the MAF method and the fully implicit method [12]. TCMFD calculation is not performed in calculation with the fully implicit method.

$$\max_{g \in G} \left| \frac{\dfrac{\vec{\phi}_g^{n',CTS}}{CP^{n'}} - \dfrac{\vec{\phi}_g^{n,ref}}{CP^{n,ref}}}{\dfrac{\vec{\phi}_g^{n,ref}}{CP^{n,ref}}} \right| \times 100\ (\%)\,, \tag{4.78}$$

where the superscript CTS and ref denote the coarse time step calculation and the reference solution, respectively. n' and n denote the time step in the coarse time step calculation and the reference solution, where n is selected so that $t^{n',CTS} = t^{n,ref}$. Note that this comparison focuses on the applicability of the coarse time step calculation for the orthogonal basis construction and both calculations are performed with the FOM. In Figure 4.8, (a), (c), and (e) show the maximum relative differences of the flux distributions (Equation (4.77)), and (b), (d), and (f) show the normalized one (Equation (4.78)).

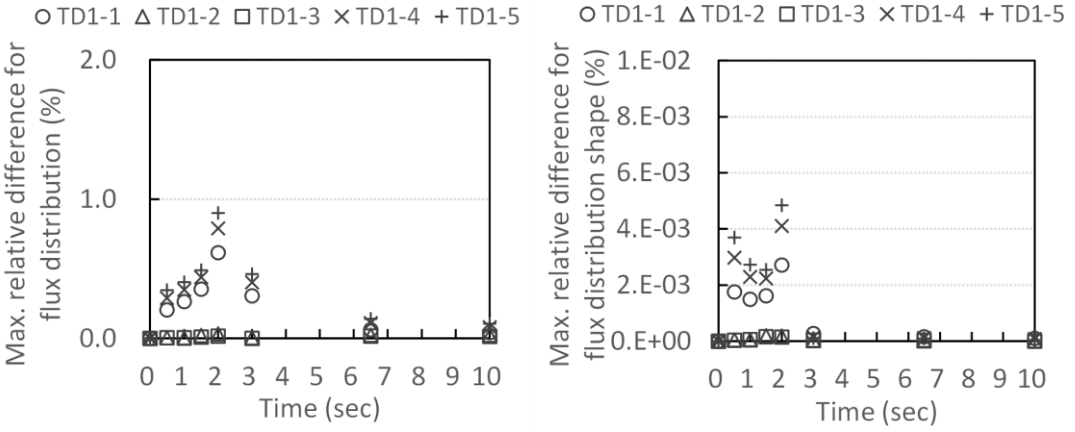

(a) TD1 – flux distribution (b) TD1 – normalized flux distribution

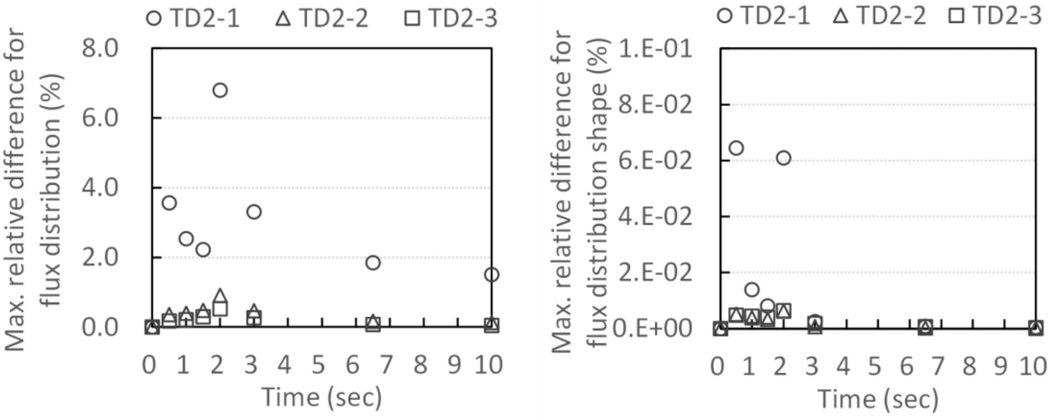

(c) TD2 – flux distribution (d) TD2 – normalized flux distribution

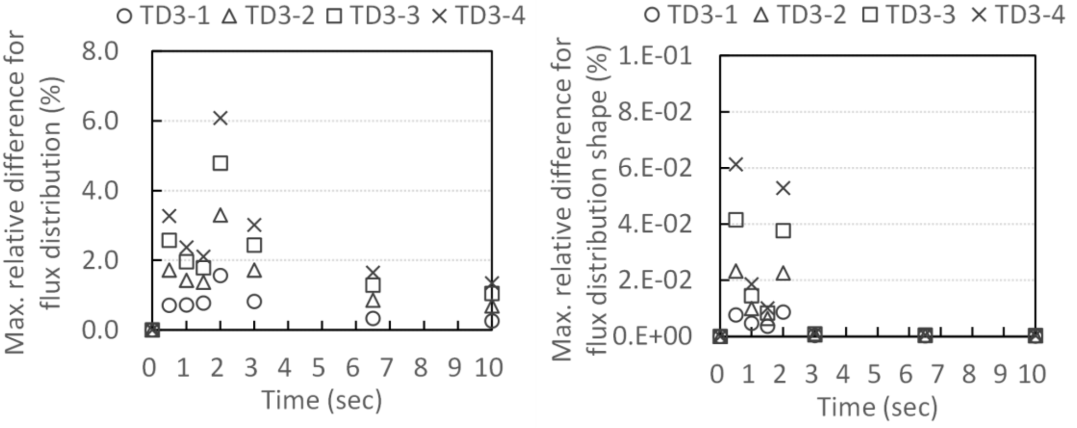

(e) TD3 – flux distribution (f) TD3 – normalized flux distribution

Figure 4.8 Accuracy of flux distributions in coarse step FOM calculations

As shown in Figure 4.8, the flux distributions in the coarse time step solution include large temporal discretization errors. However, the normalized flux distributions, which are employed for the orthogonal basis construction in the present study, are in good agreement with the reference solution. These results suggest that the coarse time step calculation can be an alternative to the reference solution for the orthogonal basis construction.

Table 4.4 shows the case matrix for the ROM construction.

Table 4.4 Case matrix for verification for efficiency of ROM construction

Case name	Sampling source	Sampled time steps for flux distributions	Sampled time steps for coefficient matrices
Case 4	Coase time step calculation	t = 0.0, 0.5, 1.0, 1.5, 2.0, 3.0, 6.5, 10.0 sec (8 steps)	
Case 5	Reference solution	t = 0.0, 0.5, 1.0, 1.5, 2.0, 3.0, 6.5, 10.0 sec (8 steps)	
Case 6	Reference solution	All time steps with 0.5 sec intervals for t = 0.0–10.0 sec (21 steps)	t = 0.0, 0.5, 1.0, 1.5, 2.0, 3.0, 6.5, 10.0 sec (8 steps)

As shown in Table 4.4, there are 3 test cases. Case 4 is the ROM constructed from the coarse time step solution. In case 5, the ROM is constructed from the reference solution, but with only 8 flux distributions at the same times used for the coarse step calculation (t = 0.0, 0.5, 1.0, 1.5, 2.0, 3.0, 6.5, 10.0 sec). The orthogonal basis for case 6 is constructed with all flux distributions in the reference solution. For all test cases, the coefficient matrices are evaluated at the same times used for the coarse step calculation. The compressed coefficient matrices are quadratically interpolated in all test cases as follows:

(1) t = 0.0 sec – 1.0 sec : quadratic interpolation with t = 0.0, 0.5, 1.0 sec
(2) t = 1.0 sec – 2.0 sec : quadratic interpolation with t = 1.0, 1.5, 2.0 sec
(3) t = 2.0 sec – 10.0 sec : quadratic interpolation with the nearest 3 time steps after t = 2.0 sec

Table 4.5 shows the size of the solution space, the orthogonal bases, and the coefficient matrices in the present calculation conditions. The low-rank approximation for the orthogonal bases is not applied in all cases.

Table 4.5 Size of orthogonal bases and coefficient matrices

Matrix	Case 4	Case 5	Case 6
Solution space ($\mathbb{R}_{\mathrm{F},g}$, $\mathbb{R}_{\mathrm{PF}}$, $\mathbb{R}_{\mathrm{DF},j}$)	31501×8	31501×8	31501×21
Orthogonal bases ($\mathbf{U}_{\mathbf{F},\boldsymbol{g}}$, $\mathbf{U}_{\mathbf{PF}}$, $\mathbf{U}_{\mathbf{DF},\boldsymbol{j}}$)	31501×8	31501×8	31501×21
Coefficient matrices ($\mathbf{A}_{\boldsymbol{g}}^{\boldsymbol{n+1}}$)	31501×31501	31501×31501	31501×31501
Compressed coefficient matrices ($\widehat{\mathbf{A}}_{\boldsymbol{g}}^{\boldsymbol{n+1}}$)	8×8	8×8	21×21

Figures 4.9 and 4.10 show the relative difference for the core power and the maximum relative difference for the flux distributions with respect to the reference FOM solution, where the relative differences are calculated as Equations (4.75) and (4.76).

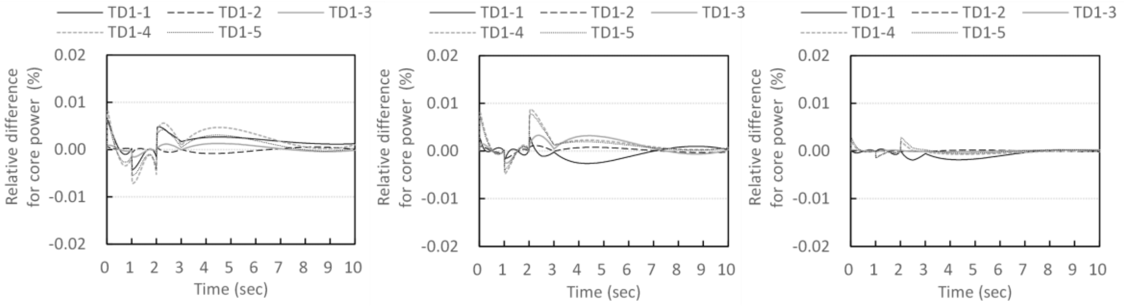

(a) TD1 – Case 4 (b) TD1 – Case 5 (c) TD1 – Case 6

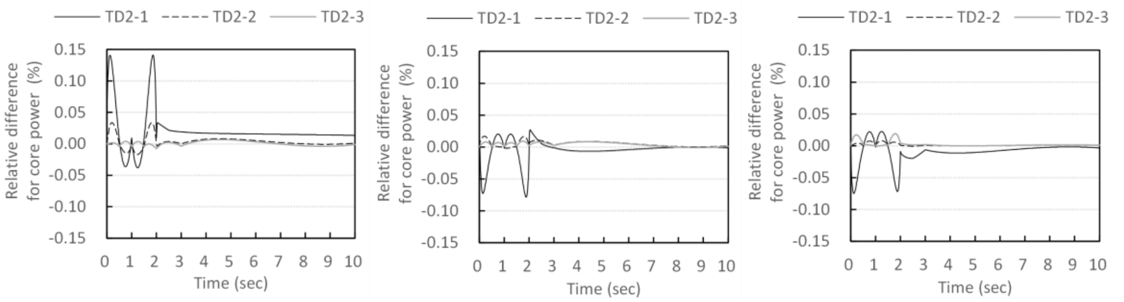

(d) TD2 – Case 4 (e) TD2 – Case 5 (f) TD2 – Case 6

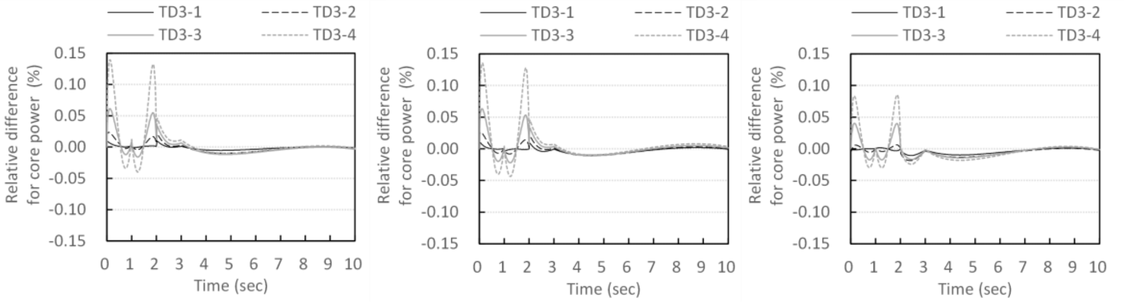

(g) TD3 – Case 4 (h) TD3 – Case 5 (i) TD3 – Case 6

Figure 4.9 Transition of relative difference for core power (case 4–6)

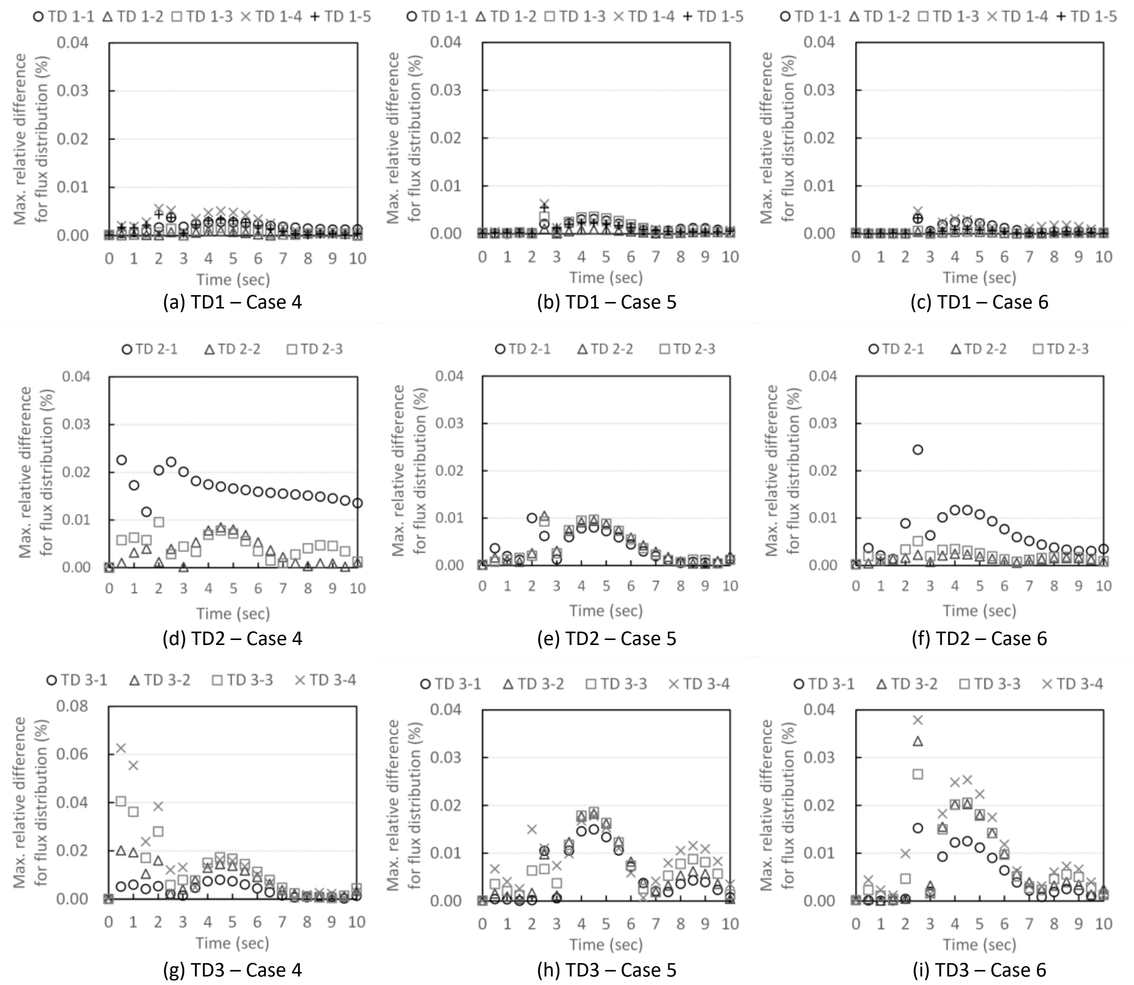

(a) TD1 – Case 4 (b) TD1 – Case 5 (c) TD1 – Case 6

(d) TD2 – Case 4 (e) TD2 – Case 5 (f) TD2 – Case 6

(g) TD3 – Case 4 (h) TD3 – Case 5 (i) TD3 – Case 6

Figure 4.10 Transition of maximum relative difference for flux distribution (case 4–6)

Since the calculation conditions of case 3 in Subsection 4.3.1 and case 6 are consistent except for the interpolation intervals for the coefficient matrices, the calculation results of cases 3 and 6 show that the interpolation error for the coefficient matrices has a negligible impact on the accuracy in the present calculation conditions. Comparing cases 5 and 6, the small degradation of the accuracy for the core power in TD3 indicates the degradation of the orthogonal basis due to fewer sampling of the flux distributions. A similar trend also appears in case 4 but the degradation of the flux distributions in Figures 4.10(d) and (g) shows the impact of the temporal discretization error for the orthogonal basis and the compressed coefficient matrices, which is reasonably small in the present calculation conditions. The maximum relative differences of the core power and flux transition between case 4 and the reference solution in the present verification are about 0.15% and 0.06%, respectively. These results suggest that the coarse step solution also can be an alternative to the reference solution in the present ROM by sampling a sufficient number of the typical flux distributions and coefficient matrices.

Table 4.6 shows the computation time of the reference solution and case 4. All calculations are carried out on Intel(R) Core$^{\mathrm{TM}}$ i9-9900K (3.6–5.0GHz) with 16 GB memory. Parallel calculation based on ray-trace-wise decomposition is carried out using 16 threads for the FOM calculation. The ROM calculation is not parallelized in the present verification.

Table 4.6 Computation time for reference FOM and ROM calculations

Test problem	Reference solution* (sec)	Case 4		
		Coarse step calculation* (sec)	SVD, DR† (sec)	ROM† (sec)
TD 1-1	14451	6657	5.3	2.4
TD 1-2	11619	5566	5.8	2.3
TD 1-3	10481	5392	5.6	2.9
TD 1-4	14108	6934	5.6	2.4
TD 1-5	15081	7337	5.8	2.4
TD 2-1	16070	7769	5.6	2.3
TD 2-2	15106	7163	6.7	2.4
TD 2-3	14556	6668	5.9	2.7
TD 3-1	16092	7384	3.6	2.4
TD 3-2	15344	7580	4.1	2.4
TD 3-3	16910	7540	4.3	2.8
TD 3-4	16319	6950	4.2	2.6

* Parallel calculation based on ray-trace-wise decomposition using 16 threads.

† Single thread calculation

As shown in Table 4.6, the present ROM enables us much faster computation than the FOM, *i.e.*, about 5000–6000 times faster computation is achieved for the ROM calculation itself. This speed-up is mainly achieved by the reduction of the DOF by the POD, *i.e.*, since the neutron balance is represented by the 8×8 compressed coefficient matrices in case 4 as shown in Table 4.5, the computational cost of the expansion coefficient is extremely small. Since 1001 steps of kinetic calculations are carried out in the present verification, the computation time of the present ROM for each time step is a few milliseconds, which is sufficiently fast to employ in real-time applications. The present ROM is still about 2 times faster than the FOM if we consider the computation time for the coarse step calculations, SVD, and DR to obtain the almost same accuracy. Since the 21 and 8 steps of MOC calculations are carried out in the reference and the coarse time step calculations respectively, the reduction of the computation time between them is almost linear for the number of the time steps.

These results suggest the effectiveness of the present approach to constructing a ROM for the time-dependent MOC calculations. In the future study, the present approach is planned to be applied to the 3-dimensional calculations because the present approach can be applied regardless of the dimensionality of the FOM, and can achieve real-time application if the size of the compressed coefficient matrices is small enough. The treatment of the feedback effect, that of the control rod movement, and the applicability of the orthogonal basis for various core situations would be important issues in the application of the present approach to 3-dimensional calculations. Resolving these technical issues, pin-resolved transport calculations could be applied to real-time applications such as online core monitoring.

4.4. Conclusion

In this chapter, an efficient ROM that reproduces the time-dependent MOC solution using the POD is proposed. In the present approach, the MOC-equivalent diffusion equation for each flux region is derived using the net neutron current calculated with MOC, and then the POD is applied to it. The flux and prompt/delayed fission rate distributions taken from a FOM solution are employed to make the orthogonal bases, which are separately defined for the scalar flux at each energy group and the precursor density at each precursor family in the present study. The accuracy of the present ROM is verified in the C5G7-TD 2D benchmark problem. The calculation results show that the non-linear time dependence of the reconstructed coefficient matrices degrades the accuracy in the present approach. However, it can be reasonably mitigated with the quadratic interpolation for them and the present ROM accurately reproduces the reference MOC solution with high accuracy in the present verification. The maximum relative differences for the core power and flux distributions in the present verification are about 0.15% and 0.06%, respectively. The computation speed of the present ROM is much faster than the MOC calculations. The maximum speed-up ratio in the present verification is about 5000–6000 for the ROM calculation itself and the computation time for the ROM construction is almost half of the reference solution. The present results also indicate that coarse step FOM calculations are effective to construct the present ROM and the temporal discretization error included in the reconstructed coefficient matrices has less impact on the accuracy. These results suggest the effectiveness of the present approach for time-dependent MOC calculations.

Since the present ROM can be applied regardless of the dimensionality of the FOM and can achieve real-time application if the size of the compressed coefficient matrices is small enough, in the future study, it is planned to be applied to the 3-dimensional MOC calculations and the treatment of the feedback effect, the control rod movement, and the applicability of the orthogonal basis for various core situations will be investigated. That could enable us to apply the pin-resolved high-fidelity transport calculations to real-time applications such as online core monitoring.

4.5. Reference

[1] Elzohery R, Roberts J, Exploring transient, neutronic, reduced-order models using DMD/POD-Galerkin and data-driven DMD, Proc PHYSOR 2020; 2020 Mar 29–Apr 2; Cambridge, United Kingdom.

[2] Elzohery R, Roberts J. Modeling neutronic transients with Galerkin projection onto a greedy-sampled, POD subspace. Ann Nucl Energy. 2021;162.

[3] Behne PA, Ragusa JC, Morel JE. Model order reduction for Sn radiation transport. Proc M&C 2019; 2019 Aug. 25–29; Oregon, Portland.

[4] Boyarinov VF, Fomichenko PA, Hou JJ, Ivanov KN, Aures A, Zwermann W, Velkov K. Deterministic time-dependent neutron transport benchmark without spatial homogenization (C5G7-TD). OECD Nuclear Energy Agency; 2017.

[5] Tatsumi M, Yamamoto A. Advanced PWR Core Calculation based on multi-group nodal-transport method in three-dimensional pin-by-pin geometry. J Nucl Sci Technol. 2003;40(6):376-387.

[6] Stacey WM, Space-time Nuclear Reactor Kinetics. New York: Academic Press; 1969.

[7] Bai Z, Demmel J, Dongrra J, Ruhe A, Vorst H. Templates for the solution of algebraic eigenvalue problems: a practical guide. Philadelphia: SIAM; 2000.

[8] Halsall MJ. CACTUS, A characteristics solution to the neutron transport equation in complicated geometries, Winfrith (United Kingdom): UKAEA; 1980, (AEEW-R 1291).

[9] Yamamoto A, Tabuchi M, Sugimura N, Ushio T, Mori M. Derivation of optimum polar angle quadrature set for the method of characteristics based on approximation error for the Bickley function. J Nucl Sci Technol. 2007;44(2):129–136.

[10] Ferrer R, Rhodes J. Linear source approximation in CASMO5. Proc PHYSOR 2012; 2012 Apr 15-20; Knoxville, Tennessee.

[11] Yamamoto A, Giho A, Yuki K, Endo T. GENESIS: a three-dimensional heterogeneous transport solver based on the Legendre polynomial expansion of angular flux method. Nucl Sci Eng. 2017;186(1):1-22.

[12] Ban Y, Endo T, Yamamoto A. A unified approach for numerical calculation of space-dependent kinetic equation. J Nucl Sci Technol. 2012;49:496–515.

5. Conclusion

5.1. Summary

In the present study, efficient numerical methods were developed to increase the computational efficiency of the time-dependent method of characteristics (MOC) calculations aiming to use high-fidelity modeling in transient calculations. However, there were several issues regarding their high computational costs. In time-dependent MOC calculations, neutron balance along a large number of the neutron flight paths is considered at each time step. It results in enormous degrees of freedom (DOF) in spatial and temporal domains, and it was the major cause of the high computational cost of time-dependent MOC calculations. While the construction of the alternative calculation model using the dimensionality reduction (DR) techniques also could be expected, it had been not established in past studies due to the enormous memory requirement for the reduced order model (ROM) construction in time-dependent MOC calculations. Thus, the following two approaches were investigated in the present study aiming to improve the computational efficiency of time-dependent MOC calculations and to enlarge their applicability to wider applications, e.g., design calculations or real-time applications:

(1) Improvement in the computational efficiency of the time-dependent MOC calculation using enhanced numerical methods

(2) Development of an effective way to construct a ROM for time-dependent MOC calculations

The first one was the utilization of enhanced numerical methods that reduce the spatial and temporal discretization error so that coarser spatial mesh structures and time steps could be used while keeping accuracy. The second one was ROM construction for time-dependent MOC calculations aiming to apply to real-time applications. In this dissertation, the enhanced numerical methods were investigated in Chapter 2, and the investigations for the ROM construction were described in Chapters 3 and 4. The technical achievements in the present study were summarized as follows:

In Chapter 2, the efficiency of time-dependent MOC calculations was improved using the multigrid amplitude function (MAF) method and the linear source approximation. In the previous study, the MAF method successfully improved the computational efficiency of time-dependent transport calculations using MOC. However, a large number of spatial meshes were required in strongly heterogeneous geometry to reduce the spatial discretization error, and it degraded the computational efficiency of the MAF method. To resolve this problem, the numerical scheme of the MAF method was derived based on the linear source approximation to reduce the spatial discretization error in MOC. The accuracy and computational efficiency of the present numerical scheme were verified in the TWIGL and the C5G7-TD 2D benchmark problems. Consequently, 6.2 times faster computation than the conventional MAF method was achieved with the present scheme while keeping the accuracy in the C5G7-TD 2D benchmark problem. It was also demonstrated that the temporal discretization error is dominated by the coarse mesh diffusion calculation in the MAF method. The present study revealed that the theta method can be effectively implemented into the time-dependent MOC calculation without any approximation for the residual term at the previous time step in the MAF method. The present numerical scheme is used as the FOM in Chapter 4 and also contributed to shortening the computation time of the FOM.

In Chapter 3, an efficient way to construct an orthogonal basis employed in time-dependent calculations using the proper orthogonal decomposition (POD) was investigated aiming to develop a ROM for time-dependent calculations. Higher-order flux distributions excited in transient calculations must be accurately represented by an orthogonal basis to construct a ROM for time-dependent calculations using the POD. In the present study, several sets of orthogonal bases, which were constructed using the different types of flux distributions, were tested to find a suitable dataset for the construction of the orthogonal basis that could accurately and efficiently represent the higher-order flux distributions. The accuracy of the ROMs constructed with the different orthogonal bases was verified in the TWIGL benchmark problem. As a result, the orthogonal basis constructed from the flux distributions obtained by coarse time step calculations accurately represented the transition of higher-order flux distributions. It also could be constructed within reasonable computation time, and the present ROM enabled approximately 100 times faster computation for the kinetic calculation itself than the full order model (FOM). These results suggest that the POD is effectively applied to real-time applications when the calculation conditions or the computational geometry are predetermined and the variation of the flux distributions are constrained by them.

In Chapter 4, an efficient ROM using the POD for time-dependent MOC calculations was developed. In the present study, coefficient matrices that reproduce a MOC solution were reconstructed using a diffusion calculation with correction terms for neutron current, and then the POD was applied to it. The accuracy and computational efficiency of the present ROM were verified in the

C5G7-TD 2D benchmark problem. As a result, the present ROM accurately reproduced the FOM solution, where the maximum relative differences between the present ROM and the FOM for the core power and flux distributions in the present verification were about 0.15% and 0.06%, respectively. As for the computation time, approximately 5000–6000 times faster computation than the FOM was achieved with the present ROM for the kinetic calculation. The average computation time per 1-time step with the present ROM was a few milliseconds in the present verification, which is sufficiently fast to achieve real-time applications. The computation time for the ROM construction was almost half of the FOM. These results suggest that the present ROM can be used as an alternative to the full-order MOC calculations when typical flux distributions of a target problem can be precalculated to construct an orthogonal basis.

As described above, the present study established efficient numerical methods that can resolve the primary issues on the computation time of time-dependent MOC calculations. The high-fidelity MOC calculations could be applied to safety analyses or real-time applications taking into the achievements of the present study.

5.2. Recommendation of future work

The present study established efficient numerical methods that can resolve the primary issues on the computation time of time-dependent MOC calculations, and confirmed their feasibility in 2-dimensional benchmark calculations. Especially, the present ROM developed in the present study can be applied regardless of the dimensionality of the FOM and can achieve real-time application if the size of the compressed coefficient matrices is small enough. To apply the present ROM to the 3-dimensional calculations and effectively achieve the real-time applications with the accuracy of the high-fidelity simulations, several technical issues would be addressed as follows:

(1) Treatment of the control rod movement (related to Chapter 4)

In the 3-dimensional calculation, the axial movement of the control rods must be taken into account. Since the axial position of the control rods is continuous, the orthogonal basis that can also represent the axial flux distributions with the partial insertion of the control rods would be necessary. While the effect of the partial insertion of the control rod can be mitigated when the axial length of the spatial meshes is small enough, the linear interpolation of the coefficient matrices also could cause the "cusp" of the flux distributions, *i.e.*, underestimation of the flux distribution by the overestimation of the neutron absorption at the partially rodded meshes. Since the "de-cusping" model for the POD is not been investigated in past studies, an effective approach for it would be desirable.

(2) Treatment of the thermal-hydraulic feedback effect (related to Chapter 4)

In the present study, the thermal-hydraulic feedback effect is not taken into account. To treat the feedback effect in the POD, variation of flux distribution due to the thermal-hydraulic parameters must be taken into account in orthogonal basis construction. Since the coefficient matrices for the neutron balance equation are also affected by the feedback effect, the difference of the cross sections due to the feedback effect also should be considered to prepare the compressed coefficient matrices. To effectively treat the compressed coefficient matrices in ROM calculations, an effective way to interpolate or estimate the compressed coefficient matrices depending on the thermal-hydraulic parameters would be desirable.

(3) Comprehensive verification for orthogonal basis in various core situations (related to Chapters 3 and 4)

In Chapter 3, the verification of the present ROM constructed from transient calculations, which is different from the target problem but the inserted reactivity is comparable, was carried out. While there was less impact on accuracy in the present verification, more comprehensive verifications including the different bank positions and/or bank worth in large geometries would be required to enlarge the applicability of the present ROM.

Appendix

A. C5G7-TD 2D benchmark results

A.1 Verification of in-house code

In the present study, a 2-dimensional in-house kinetic calculation code using the MOC is developed to verify the numerical scheme described in Chapter 2. In this subsection, the verification of the in-house code using the C5G7-TD 2D benchmark problem [1] is described.

The cross sections for seven energy groups, the delayed neutron parameters for 8 precursor groups for each material specified in the benchmark problem, and the perturbation condition for the test problems, TD1-1– TD3-4, are used as is. Table A.1 and Figure A.1 show the calculation conditions and mesh structure in the present verification, respectively.

Table A.1 Calculation conditions of the C5G7-TD 2D benchmark problem

Parameters	Calculation conditions
Azimuthal division	128 for 2π with cyclic quadrature set
Polar division	3 for π/2 with TY-opt quadrature set
Ray separation	0.01 cm using cyclic ray tracing
Convergence criterion	Fission : 10^{-6}, flux : 10^{-6}
Flux region division	Reflector cell : 0.42 cm × 0.42 cm square mesh Other cells : 24 flux regions shown in Figure A.2
Source approximation	Linear
Time discretization	MAF method Fully implicit method for the shape and amplitude functions,
Time step size	$\Delta t_{shape} = 1$ sec, $\Delta t_{amp} = 1$ msec
Coarse mesh structure for the amplitude function	1.26 cm × 1.26 cm square mesh

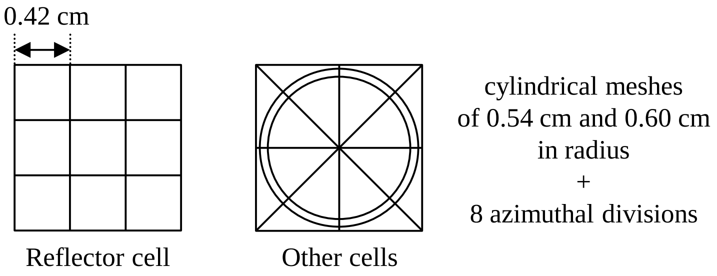

Figure A.1　Flux region division

In the C5G7-TD 2D benchmark problem, the reference solution of the initial k_{eff} is provided with the Monte Carlo code MCNP5 [1]. Table A.2 shows the comparison for the initial k_{eff}. In Table A.2, that of the planer MOC calculation code, MPACT, is also described for comparison.

Table A.2　Initial k_{eff} in the C5G7-TD 2D benchmark problem

	MCNP (reference)	MPACT	Present study
Initial k_{eff}	1.18646 ± 0.07%	1.186673	1.186507
Relative error	-	+18 pcm	+4 pcm

As shown in Table A.2, the initial k_{eff} calculated with the in-house code is in good agreement with the reference solution.

Table A.3 shows the core power transition of the in-house code. Figure A.2 shows the core power transition of the in-house code and the relative difference with the MPACT code, respectively. In Figure A.2, the relative difference of the core power is calculated as:

$$\text{Relative difference (\%)} = \frac{CP - CP^{MPACT}}{CP^{MPACT}} \times 100 \,, \tag{3.42}$$

where the superscript, $MPACT$, denotes the calculation result of the MPACT code.

Table A.3 Core power transition of the C5G7-TD 2D benchmark problem (1/3)

Time (sec)	TD 1-1	TD 1-2	TD 1-3	TD 1-4	TD 1-5	TD 2-1	TD 2-2	TD 2-3	TD 3-1	TD 3-2	TD 3-3	TD 3-4
0.0	1.00000	1.00000	1.00000	1.00000	1.00000	1.00000	1.00000	1.00000	1.00000	1.00000	1.00000	1.00000
0.1	0.93712	0.99112	0.99434	0.92450	0.91694	0.59950	0.91943	0.94784	0.87384	0.77433	0.69393	0.62767
0.2	0.87817	0.98194	0.98850	0.85545	0.84209	0.42273	0.84857	0.89993	0.76850	0.62005	0.51708	0.44159
0.3	0.82442	0.97264	0.98256	0.79388	0.77626	0.32496	0.78741	0.85690	0.68176	0.51089	0.40482	0.33275
0.4	0.77536	0.96326	0.97653	0.73879	0.71803	0.26293	0.73411	0.81805	0.60930	0.42986	0.32757	0.26174
0.5	0.73048	0.95381	0.97044	0.68931	0.66629	0.22014	0.68732	0.78281	0.54805	0.36757	0.27145	0.21206
0.6	0.68936	0.94434	0.96430	0.64472	0.62010	0.18890	0.64590	0.75071	0.49573	0.31838	0.22905	0.17560
0.7	0.65161	0.93484	0.95811	0.60440	0.57868	0.16513	0.60903	0.72135	0.45063	0.27870	0.19605	0.14786
0.8	0.61688	0.92535	0.95188	0.56781	0.54139	0.14647	0.57602	0.69439	0.41145	0.24613	0.16975	0.12617
0.9	0.58487	0.91586	0.94563	0.53451	0.50769	0.13145	0.54627	0.66955	0.37716	0.21900	0.14839	0.10883
1.0	0.55530	0.90639	0.93938	0.50412	0.47713	0.11911	0.51935	0.64658	0.34698	0.19612	0.13077	0.09471
1.1	0.57078	0.91121	0.94258	0.52030	0.49351	0.12576	0.53267	0.65750	0.36412	0.20993	0.14188	0.10392
1.2	0.58952	0.91688	0.94636	0.53990	0.51338	0.13425	0.54930	0.67121	0.38488	0.22683	0.15553	0.11525
1.3	0.61104	0.92305	0.95045	0.56257	0.53648	0.14511	0.56904	0.68735	0.40937	0.24736	0.17234	0.12934
1.4	0.63568	0.92967	0.95481	0.58877	0.56330	0.15926	0.59240	0.70623	0.43840	0.27265	0.19346	0.14723
1.5	0.66388	0.93674	0.95945	0.61909	0.59455	0.17821	0.62009	0.72823	0.47308	0.30438	0.22065	0.17064
1.6	0.69623	0.94425	0.96436	0.65431	0.63112	0.20462	0.65307	0.75391	0.51498	0.34515	0.25679	0.20244
1.7	0.73345	0.95220	0.96952	0.69544	0.67420	0.24353	0.69261	0.78394	0.56632	0.39919	0.30697	0.24796
1.8	0.77648	0.96060	0.97494	0.74384	0.72541	0.30594	0.74051	0.81923	0.63035	0.47383	0.38095	0.31822
1.9	0.82657	0.96944	0.98061	0.80131	0.78698	0.42086	0.79928	0.86098	0.71200	0.58293	0.50011	0.43997
2.0	0.88531	0.97872	0.98654	0.87035	0.86202	0.69615	0.87263	0.91082	0.81912	0.75603	0.72131	0.69842
2.1	0.89100	0.97971	0.98715	0.87688	0.86905	0.71974	0.87927	0.91535	0.82877	0.77069	0.73976	0.72008
2.2	0.89444	0.98034	0.98754	0.88077	0.87319	0.72892	0.88311	0.91804	0.83420	0.77806	0.74819	0.72919
2.3	0.89743	0.98089	0.98789	0.88415	0.87679	0.73685	0.88645	0.92037	0.83890	0.78444	0.75547	0.73707
2.4	0.90005	0.98137	0.98819	0.88712	0.87995	0.74379	0.88937	0.92242	0.84304	0.79003	0.76185	0.74395
2.5	0.90237	0.98180	0.98846	0.88975	0.88275	0.74990	0.89197	0.92424	0.84670	0.79498	0.76748	0.75003
2.6	0.90446	0.98218	0.98870	0.89211	0.88526	0.75535	0.89429	0.92587	0.84997	0.79940	0.77251	0.75545
2.7	0.90634	0.98253	0.98892	0.89423	0.88752	0.76025	0.89638	0.92733	0.85294	0.80338	0.77704	0.76033
2.8	0.90805	0.98284	0.98911	0.89616	0.88958	0.76469	0.89828	0.92866	0.85566	0.80699	0.78114	0.76476
2.9	0.90961	0.98313	0.98929	0.89793	0.89146	0.76874	0.90001	0.92988	0.85811	0.81028	0.78489	0.76879
3.0	0.91104	0.98339	0.98946	0.89955	0.89318	0.77246	0.90161	0.93099	0.86036	0.81332	0.78833	0.77250
3.1	0.91238	0.98364	0.98961	0.90106	0.89478	0.77588	0.90309	0.93204	0.86248	0.81610	0.79151	0.77593
3.2	0.91361	0.98386	0.98975	0.90245	0.89626	0.77906	0.90446	0.93300	0.86442	0.81870	0.79446	0.77910
3.3	0.91476	0.98407	0.98989	0.90375	0.89765	0.78202	0.90574	0.93389	0.86622	0.82112	0.79721	0.78206

Table A.3 Core power transition of the C5G7-TD 2D benchmark problem (2/3)

Time (sec)	TD 1-1	TD 1-2	TD 1-3	TD 1-4	TD 1-5	TD 2-1	TD 2-2	TD 2-3	TD 3-1	TD 3-2	TD 3-3	TD 3-4
3.4	0.91584	0.98427	0.99001	0.90497	0.89894	0.78479	0.90693	0.93473	0.86792	0.82338	0.79977	0.78483
3.5	0.91685	0.98446	0.99013	0.90612	0.90016	0.78739	0.90806	0.93552	0.86951	0.82551	0.80219	0.78743
3.6	0.91781	0.98463	0.99024	0.90719	0.90131	0.78985	0.90912	0.93626	0.87101	0.82752	0.80446	0.78988
3.7	0.91871	0.98480	0.99034	0.90822	0.90239	0.79217	0.91012	0.93697	0.87243	0.82942	0.80662	0.79220
3.8	0.91957	0.98496	0.99044	0.90918	0.90342	0.79437	0.91107	0.93763	0.87377	0.83122	0.80866	0.79440
3.9	0.92038	0.98510	0.99053	0.91011	0.90440	0.79646	0.91197	0.93827	0.87506	0.83293	0.81060	0.79649
4.0	0.92115	0.98525	0.99062	0.91098	0.90534	0.79846	0.91284	0.93887	0.87628	0.83457	0.81246	0.79849
4.1	0.92191	0.98539	0.99071	0.91183	0.90624	0.80037	0.91367	0.93945	0.87746	0.83615	0.81425	0.80038
4.2	0.92262	0.98552	0.99079	0.91264	0.90709	0.80219	0.91446	0.94000	0.87858	0.83765	0.81595	0.80220
4.3	0.92331	0.98564	0.99087	0.91341	0.90792	0.80394	0.91522	0.94053	0.87965	0.83908	0.81758	0.80395
4.4	0.92396	0.98576	0.99094	0.91415	0.90871	0.80563	0.91595	0.94104	0.88068	0.84046	0.81914	0.80563
4.5	0.92460	0.98588	0.99101	0.91487	0.90947	0.80725	0.91665	0.94154	0.88168	0.84179	0.82065	0.80725
4.6	0.92521	0.98599	0.99108	0.91555	0.91020	0.80881	0.91732	0.94201	0.88264	0.84307	0.82210	0.80881
4.7	0.92580	0.98610	0.99115	0.91622	0.91091	0.81031	0.91798	0.94247	0.88356	0.84431	0.82351	0.81031
4.8	0.92637	0.98620	0.99122	0.91686	0.91159	0.81177	0.91861	0.94291	0.88446	0.84550	0.82486	0.81177
4.9	0.92692	0.98630	0.99128	0.91749	0.91225	0.81318	0.91922	0.94334	0.88532	0.84666	0.82618	0.81318
5.0	0.92745	0.98640	0.99134	0.91809	0.91289	0.81455	0.91981	0.94375	0.88616	0.84778	0.82744	0.81455
5.1	0.92797	0.98649	0.99140	0.91868	0.91353	0.81589	0.92039	0.94416	0.88698	0.84889	0.82869	0.81589
5.2	0.92848	0.98659	0.99146	0.91925	0.91413	0.81718	0.92095	0.94455	0.88778	0.84994	0.82989	0.81718
5.3	0.92897	0.98667	0.99151	0.91980	0.91472	0.81844	0.92149	0.94493	0.88854	0.85097	0.83106	0.81844
5.4	0.92944	0.98676	0.99157	0.92034	0.91529	0.81965	0.92201	0.94530	0.88929	0.85197	0.83219	0.81966
5.5	0.92991	0.98685	0.99162	0.92086	0.91585	0.82084	0.92253	0.94566	0.89002	0.85295	0.83330	0.82084
5.6	0.93036	0.98693	0.99167	0.92137	0.91639	0.82200	0.92303	0.94601	0.89073	0.85390	0.83437	0.82200
5.7	0.93080	0.98701	0.99172	0.92187	0.91692	0.82312	0.92352	0.94635	0.89142	0.85482	0.83542	0.82312
5.8	0.93123	0.98709	0.99177	0.92236	0.91744	0.82422	0.92399	0.94668	0.89210	0.85572	0.83644	0.82422
5.9	0.93165	0.98716	0.99182	0.92283	0.91794	0.82529	0.92445	0.94701	0.89275	0.85660	0.83744	0.82530
6.0	0.93205	0.98723	0.99186	0.92329	0.91843	0.82634	0.92491	0.94732	0.89340	0.85746	0.83842	0.82634
6.1	0.93246	0.98731	0.99191	0.92375	0.91892	0.82737	0.92535	0.94763	0.89403	0.85831	0.83937	0.82738
6.2	0.93285	0.98738	0.99195	0.92419	0.91939	0.82837	0.92579	0.94794	0.89465	0.85914	0.84031	0.82838
6.3	0.93323	0.98745	0.99199	0.92462	0.91985	0.82935	0.92621	0.94823	0.89525	0.85994	0.84122	0.82936
6.4	0.93360	0.98752	0.99204	0.92504	0.92029	0.83030	0.92662	0.94852	0.89583	0.86072	0.84210	0.83030
6.5	0.93397	0.98758	0.99208	0.92546	0.92073	0.83125	0.92703	0.94881	0.89641	0.86150	0.84298	0.83125
6.6	0.93433	0.98765	0.99212	0.92586	0.92116	0.83216	0.92742	0.94908	0.89697	0.86224	0.84383	0.83216
6.7	0.93468	0.98771	0.99216	0.92626	0.92159	0.83306	0.92781	0.94936	0.89753	0.86299	0.84467	0.83307

Table A.3 Core power transition of the C5G7-TD 2D benchmark problem (3/3)

Time (sec)	TD 1-1	TD 1-2	TD 1-3	TD 1-4	TD 1-5	TD 2-1	TD 2-2	TD 2-3	TD 3-1	TD 3-2	TD 3-3	TD 3-4
6.8	0.93502	0.98777	0.99220	0.92664	0.92200	0.83394	0.92819	0.94962	0.89806	0.86370	0.84548	0.83394
6.9	0.93536	0.98784	0.99223	0.92702	0.92240	0.83480	0.92856	0.94988	0.89859	0.86441	0.84629	0.83480
7.0	0.93569	0.98789	0.99227	0.92740	0.92280	0.83564	0.92893	0.95014	0.89911	0.86511	0.84708	0.83565
7.1	0.93602	0.98796	0.99231	0.92777	0.92319	0.83648	0.92929	0.95039	0.89963	0.86579	0.84785	0.83649
7.2	0.93633	0.98801	0.99234	0.92813	0.92357	0.83730	0.92964	0.95064	0.90013	0.86646	0.84861	0.83730
7.3	0.93665	0.98807	0.99238	0.92848	0.92395	0.83810	0.92999	0.95088	0.90062	0.86712	0.84936	0.83811
7.4	0.93695	0.98812	0.99241	0.92883	0.92432	0.83889	0.93033	0.95112	0.90110	0.86776	0.85009	0.83889
7.5	0.93725	0.98818	0.99245	0.92917	0.92468	0.83966	0.93066	0.95135	0.90157	0.86840	0.85081	0.83966
7.6	0.93755	0.98823	0.99248	0.92950	0.92504	0.84042	0.93099	0.95158	0.90204	0.86902	0.85151	0.84042
7.7	0.93784	0.98828	0.99251	0.92983	0.92538	0.84116	0.93131	0.95180	0.90250	0.86963	0.85220	0.84117
7.8	0.93812	0.98834	0.99254	0.93015	0.92573	0.84189	0.93162	0.95202	0.90294	0.87023	0.85288	0.84190
7.9	0.93840	0.98839	0.99258	0.93047	0.92606	0.84261	0.93193	0.95224	0.90338	0.87082	0.85355	0.84262
8.0	0.93868	0.98844	0.99261	0.93078	0.92639	0.84332	0.93224	0.95245	0.90382	0.87140	0.85421	0.84332
8.1	0.93895	0.98849	0.99264	0.93109	0.92672	0.84401	0.93254	0.95266	0.90425	0.87197	0.85486	0.84402
8.2	0.93922	0.98853	0.99267	0.93139	0.92704	0.84470	0.93284	0.95287	0.90467	0.87254	0.85550	0.84470
8.3	0.93948	0.98858	0.99270	0.93169	0.92736	0.84537	0.93313	0.95307	0.90508	0.87309	0.85612	0.84537
8.4	0.93974	0.98863	0.99272	0.93198	0.92767	0.84603	0.93341	0.95327	0.90548	0.87363	0.85674	0.84603
8.5	0.93999	0.98867	0.99275	0.93226	0.92797	0.84668	0.93369	0.95347	0.90588	0.87416	0.85734	0.84668
8.6	0.94024	0.98872	0.99278	0.93254	0.92827	0.84732	0.93397	0.95366	0.90627	0.87469	0.85793	0.84732
8.7	0.94049	0.98876	0.99281	0.93282	0.92857	0.84795	0.93424	0.95385	0.90666	0.87520	0.85852	0.84795
8.8	0.94073	0.98880	0.99283	0.93309	0.92886	0.84857	0.93451	0.95404	0.90704	0.87571	0.85910	0.84857
8.9	0.94097	0.98885	0.99286	0.93336	0.92914	0.84918	0.93477	0.95422	0.90741	0.87621	0.85966	0.84918
9.0	0.94120	0.98889	0.99289	0.93363	0.92942	0.84978	0.93503	0.95441	0.90778	0.87671	0.86022	0.84978
9.1	0.94143	0.98893	0.99291	0.93389	0.92970	0.85037	0.93529	0.95458	0.90815	0.87719	0.86078	0.85038
9.2	0.94166	0.98897	0.99294	0.93415	0.92998	0.85095	0.93554	0.95476	0.90851	0.87767	0.86132	0.85096
9.3	0.94188	0.98901	0.99296	0.93440	0.93025	0.85153	0.93578	0.95493	0.90886	0.87814	0.86185	0.85153
9.4	0.94210	0.98905	0.99299	0.93465	0.93051	0.85209	0.93603	0.95510	0.90920	0.87861	0.86238	0.85210
9.5	0.94232	0.98909	0.99301	0.93489	0.93077	0.85265	0.93627	0.95527	0.90955	0.87906	0.86290	0.85265
9.6	0.94253	0.98913	0.99303	0.93514	0.93103	0.85320	0.93650	0.95544	0.90988	0.87951	0.86341	0.85320
9.7	0.94274	0.98917	0.99306	0.93537	0.93128	0.85374	0.93674	0.95560	0.91021	0.87996	0.86391	0.85374
9.8	0.94295	0.98920	0.99308	0.93561	0.93153	0.85427	0.93697	0.95576	0.91054	0.88040	0.86441	0.85428
9.9	0.94316	0.98924	0.99310	0.93584	0.93178	0.85480	0.93719	0.95592	0.91086	0.88083	0.86490	0.85480
10.0	0.94336	0.98928	0.99312	0.93607	0.93202	0.85532	0.93742	0.95607	0.91118	0.88125	0.86539	0.85533

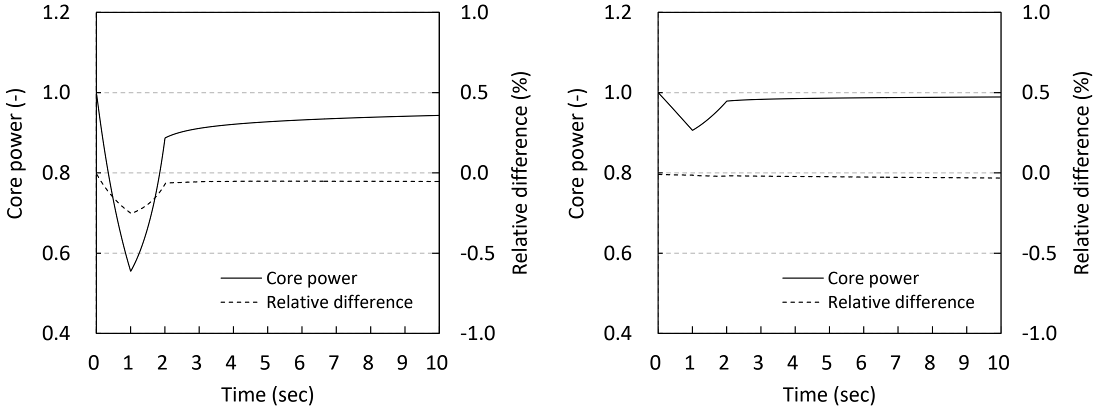

(a) TD 1-1

(b) TD 1-2

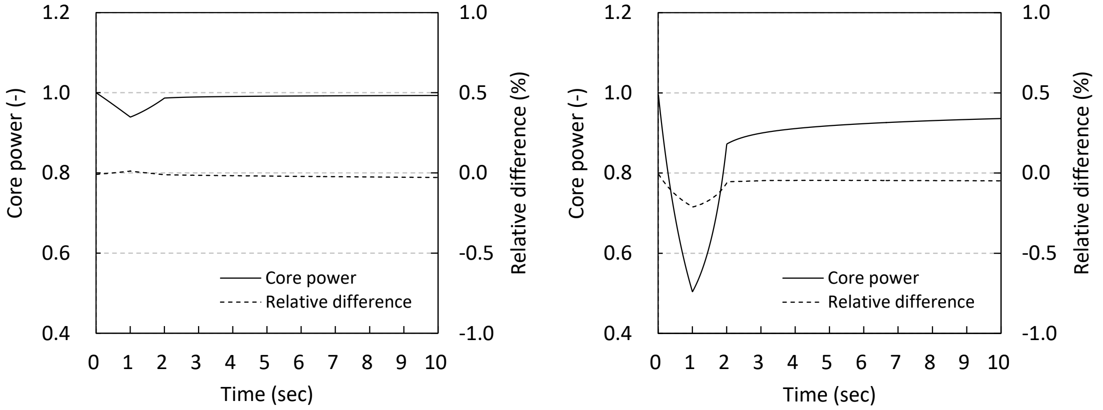

(c) TD 1-3

(d) TD 1-4

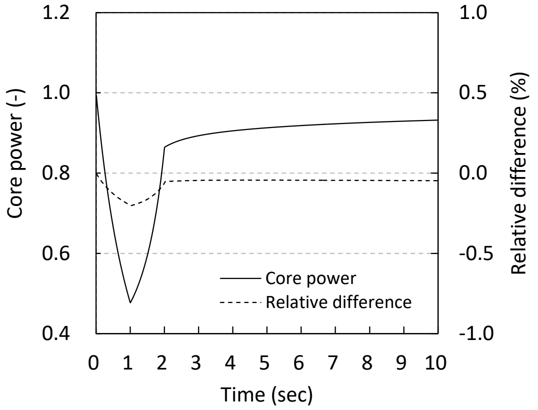

(e) TD 1-5

Figure A.2 Comparison of the core power transition with MPACT (1/3)

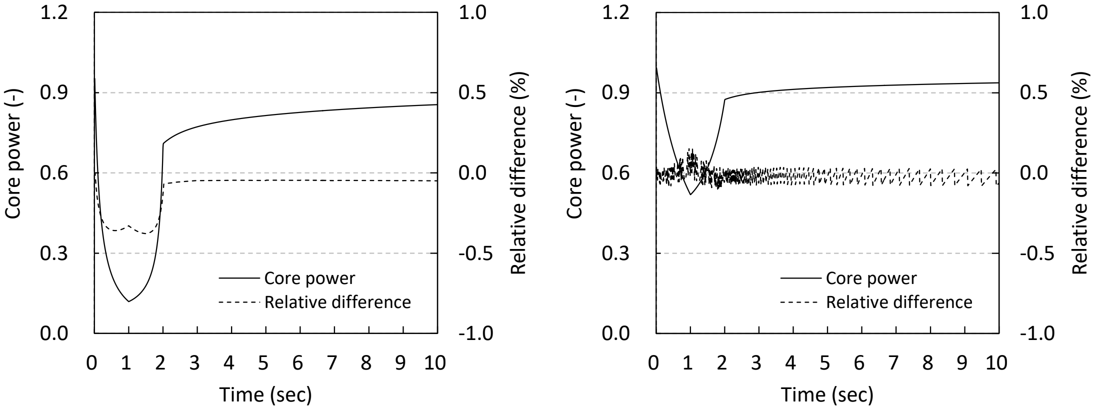

(f) TD 2-1 (g) TD 2-2

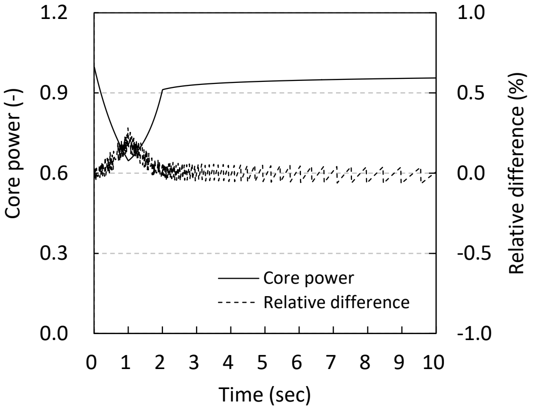

(h) TD 2-3

Figure A.2 Comparison of the core power transition with MPACT (2/3)

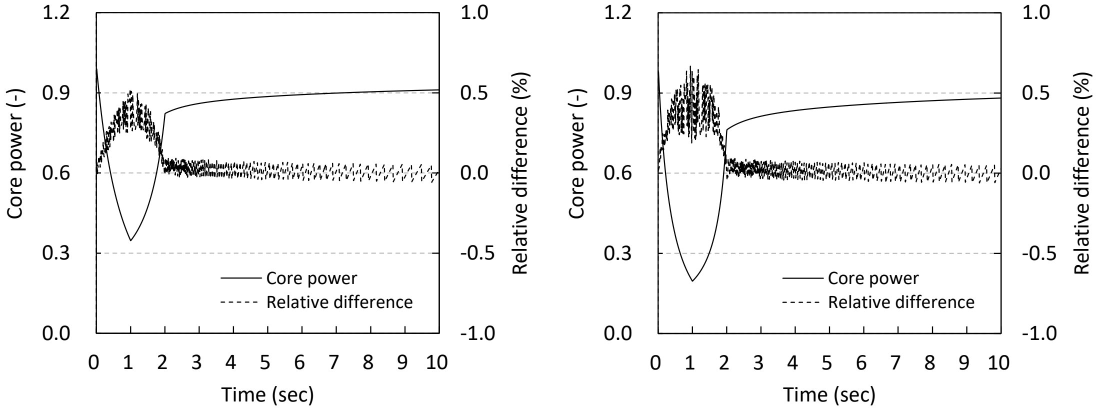

(i) TD 3-1 (j) TD 3-2

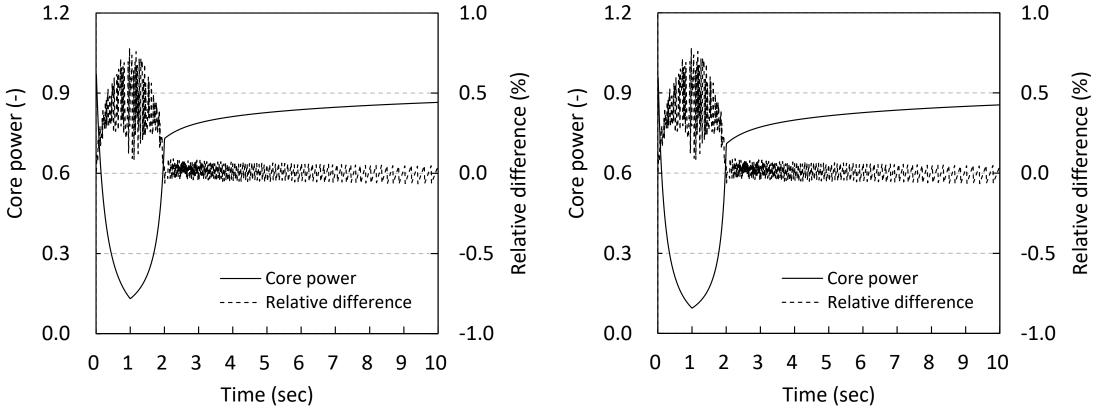

(k) TD 3-3 (l) TD 3-4

Figure A.2 Comparison of the core power transition with MPACT (3/3)

As shown in Figure A.2, the relative differences for the core power calculated with the in-house code and that of MPACT are less than about 1.0% and are in good agreement, where they come from the spatial/temporal discretization error due to calculation conditions and computational methodologies. Note that the oscillations of the relative difference for the core power in TD2-2–TD3-4 come from the rounding error, where only 3 effective digits for the MPACT solution are available in the reference [2]. These results support the accuracy of the results of the in-house code.

A.2 Reference

[1] Boyarinov VF, Fomichenko PA, Hou JJ, Ivanov KN, Aures A, Zwermann W, Velkov K. Deterministic time-dependent neutron transport benchmark without spatial homogenization (C5G7-TD). OECD Nuclear Energy Agency; 2017.

[2] Shen Q, Wang Y, Jabaay D, Kochunas B, Downar TJ. Transient analysis of C5G7-TD benchmark

with MPACT. Ann Nucl Energy. 2019;125:107–120.

This page is intentionally left blank.

Acknowledgments

The author would like to express his heartfelt gratitude to his advisor, Professor Akio Yamamoto of Nagoya University for his thoughtful advice and invaluable suggestions throughout this study.

The author is deeply indebted to Associate Professor Tomohiro Endo of Nagoya University for his insightful advice and warm encouragement.

The author owes a debt of gratitude to Professor Yoshiyuki Tsuji, Associate Professor Atsushi Okamoto, Associate professor Takahiko Sugiyama of Nagoya University, and Associate professor Hiroki Takezawa of Nagaoka University of Technology for their helpful comments to complete this dissertation.

The author would like to thank Nuclear Engineering, Ltd. (NEL) and the staffs in the design and analysis group of NEL for their support to study in the doctoral course at Nagoya University.

Finally, the author would like to express thanks to his family for their continuous support and encouragement.

This page is intentionally left blank.

List of papers published by the author

Publication in journals

(1) Tsujita K, Endo T, Yamamoto A. Application of the multigrid amplitude function method for time-dependent MOC based on the linear source approximation. J Nucl Sci Technol. 2020;57:646–662.

(2) Tsujita K, Endo T, Yamamoto A. Fast reproduction of time-dependent diffusion calculations using the reduced order model based on the proper orthogonal and singular value decompositions. J Nucl Sci Technol. 2021;58:173–183.

(3) Tsujita K, Endo T, Yamamoto A. Efficient reduced order model based on the proper orthogonal decomposition for time-dependent MOC calculations. J Nucl Sci Technol. 2022. DOI: 10.1080/00223131.2022.2097963

Publication in conference proceedings

(1) Tsujita K, Endo T, Yamamoto A. C5G7-TD benchmark analysis using multigrid amplitude function method. Proc RPHA19; 2019 Dec 2–3; Osaka, Japan.

(2) Tsujita K, Endo T, Yamamoto A. Fast reproduction of time-dependent MOC calculations using the reduced order model based on the proper orthogonal and singular value decompositions. Trans Am Nucl Soc; 2020;123:1349–1353.